

**Naval Research Laboratory**

Washington, DC 20375-5320

**AD-A266 132**

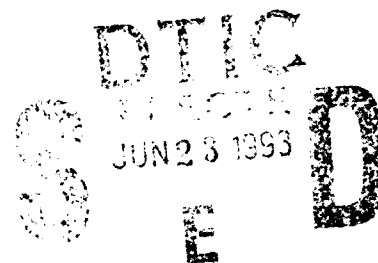


**NRL/MR/6722--93-7301**

# **Advanced Concepts Theory Annual Report 1992, Final Report**

*Radiation Hydrodynamics Branch  
Plasma Physics Division*

**May 26, 1993**



This research was sponsored by the Defense Nuclear Agency under Subtask RLRA/Advanced Technology Development, and Work Unit Title, 000789, "Advanced Technology Development," MIPR No. 92-580.

**93 6 22 04 8**  
Approved for public release; distribution unlimited.

**93-14018**



120px

REPORT DOCUMENTATION PAGE			Form Approved OMB No. 0704-0188	
Public reporting burden for this collection of information is estimated to average 1 hour per response, including the time for reviewing instructions, searching existing data sources, gathering and maintaining the data needed, and completing and reviewing the collection of information. Send comments regarding this burden estimate or any other aspect of this collection of information, including suggestions for reducing this burden, to Washington Headquarters Services, Directorate for Information Operations and Reports, 1215 Jefferson Davis Highway, Suite 1204, Arlington, VA 22202-4302, and to the Office of Management and Budget, Paperwork Reduction Project (0704-0188), Washington, DC 20503.				
1. AGENCY USE ONLY (Leave Blank)	2. REPORT DATE  May 26, 1993	3. REPORT TYPE AND DATES COVERED  Final Report		
4. TITLE AND SUBTITLE  Advanced Concepts Theory Annual Report 1992, Final Report		5. FUNDING NUMBERS PE - 62715H WU - DNA 880-191		
6. AUTHOR(S)  Radiation Hydrodynamics Branch				
7. PERFORMING ORGANIZATION NAME(S) AND ADDRESS(ES)  Naval Research Laboratory Washington, DC 20375-5320		8. PERFORMING ORGANIZATION REPORT NUMBER  NRL/MR/6722-93-7301		
9. SPONSORING/MONITORING AGENCY NAME(S) AND ADDRESS(ES)  Defense Nuclear Agency RAEV Alexandria, VA 22310		10. SPONSORING/MONITORING AGENCY REPORT NUMBER		
11. SUPPLEMENTARY NOTES  This research was sponsored by the Defense Nuclear Agency under Subtask RLRA/Advanced Technology Development, and Work Unit Code and Title, 000789, "Advanced Technology Development," MIPR No. 92-588				
12a. DISTRIBUTION/AVAILABILITY STATEMENT  Approved for public release; distribution unlimited.		12b. DISTRIBUTION CODE		
13. ABSTRACT (Maximum 200 words)  This report details the work of the Radiation Hydrodynamics Branch conducted in FY92 with respect to several critical problems concerning the design and analysis of z-pinch experiments, the electron dynamics of z-pinch implosions, and the optimization of their radiative output. Separate sections describe progress in: (1) the design of z-pinch wire and gas puff experiments, (2) the analysis and scaling of z-pinch experiments using phenomenological turbulence transport parameters, (3) the development of a non-Maxwellian electron distribution function analysis from which to calculate turbulence enhanced transport coefficients, (4) the development of L-shell atomic models, (5) the analysis of PRS argon experiments, and (6) the development of a POS transmission line model with which to study power flow in IES machines, POS/PRS interactions, and energy coupling to PRS loads.				
14. SUBJECT TERMS  Z-pinch physics Radiation MHD		Plasma radiation sources		15. NUMBER OF PAGES  120
				16. PRICE CODE
17. SECURITY CLASSIFICATION OF REPORT  UNCLASSIFIED	18. SECURITY CLASSIFICATION OF THIS PAGE  UNCLASSIFIED	19. SECURITY CLASSIFICATION OF ABSTRACT  UNCLASSIFIED	20. LIMITATION OF ABSTRACT  UL	

## CONTENTS

EXECUTIVE PROGRAM SUMMARY .....	E-1
I. DESIGNING WIRE ARRAY PRS EXPERIMENTS FOR PRESENT-DAY PULSED POWER GENERATORS .....	1
II. COMPARISON OF PI ARGON EXPERIMENTS WITH 1-D ENHANCED TRANSPORT CALCULATIONS .....	18
III. NON-MAXWELLIAN DISTRIBUTION FUNCTIONS IN DECADE-CLASS Z-PINCHES .....	30
IV. PRS NOZZLE DESIGN AND GAS PUFF SIMULATION .....	69
V. COUPLING PRS LOADS TO DECADE CLASS, LONG CONDUCTION TIME POS INDUCTIVE GENERATORS .....	86
VI. L-SHELL MODEL DEVELOPMENT AND SCALING .....	104

Accession For	
NTIS CRA&I	<input checked="" type="checkbox"/>
DTIC TAB	<input type="checkbox"/>
Unannounced	<input type="checkbox"/>
Justification	
By	
Distribution /	
Availability Codes	
Dist	Avail and/or Special
<b>A-1</b>	

## EXECUTIVE SUMMARY

Six DECADE related problem areas were the focus of Code 6720 efforts in FY 1992 in the Plasma Radiation Source (PRS) Theory Program:

- (1) An important need exists to better understand and to improve the performance of large aspect ratio wire array implosions, i.e., those implosions for which the initial array diameter is greater than 2 cm. The ability to extend the kilovolt emission spectrum in DECADE toward warm x-rays depends on the effectiveness of these implosions. While kinetic energy arguments can provide sufficient guidance for scaling pulsed power machine design, DNA is ultimately concerned with achieving the best performance from the x-ray simulators that utilize these machines. In order to begin an evaluation of the effectiveness of large aspect ratio implosions to convert kinetic energy into kilovolt x-rays, a series of PRS experiments was planned for the SATURN machine at Sandia National Laboratory. These experiments were carried out in August, 1992. They were also carefully designed to increase the maximum yield of kilovolt x-rays from aluminum array implosions on SATURN from its previous high value, and to allow meaningful comparisons with similar experiments conducted on the Double EAGLE machine at Physics International, Inc. to be made. While the experiments did achieve a significant increase in kilovolt yield, they did not perform entirely up to expectations, especially for the large aspect ratio implosions. The design of these and of follow-up experiments is discussed in Section I of this report. Serious analysis of the SATURN experiments will take place in FY93.
- (2) Because experimental implosions are much softer (i.e., much lower in density and much fatter in extent) than classically calculated 1-D MHD implosions, it is important to phenomenologically determine enhancements to classically calculated plasma viscosities, heat conductivities, and electrical resistivities in order to explain the present-day experiments. This soft implosion modeling is also needed to provide a more realistic scaling of load designs from present-day machines to DECADE. It was found this year, for example, that soft implosion modeling of argon implosions significantly modifies the scaling of K-shell yield with load mass and implosion velocity. In particular, the breakpoint masses for achieving efficient K-shell emission are shifted upwards from their predicted hard implosion values. It was also found that soft implosion modeling can achieve reasonably good agreement with experimental density, temperature, and K-shell yield measurements, and that it can also predict the experimental trends of this data. This work is described in Section II.
- (3) As machine currents increase, load current densities will increase, and the need to determine the current flow dynamics in the presence of possible plasma microturbulence, runaway electron, and non-Maxwellian electron distribution effects could become increasingly important. Current profiles determine the force dynamics on the PRS plasma, the coupling of the PRS load to the generator, and the transfer of energy from the electrons to the ions in the load and subsequently into x-rays. Progress on the analysis of this electron dynamics in DECADE-class machines is discussed in Section III.
- (4) Because of the finite number of return current posts used in PRS diodes and because of the three dimensional flow patterns of gas jets, exploding wire arrays, and metal vapor jets, 2-D

MHD modeling of PRS load implosions is essential in order to optimize load symmetry and kinetic energy generation and conversion on axis. This problem may be especially critical for large aspect ratio implosions. For wire arrays,  $r$ - $\theta$  calculations are needed to determine the optimal positioning of the wires. For gas puff implosions,  $r$ - $z$  calculations are needed to help determine optimal nozzle designs and tilt angles. This latter work on Double EAGLE and SATURN is discussed in Section IV. The Double EAGLE work has provided an important benchmark for extending these calculations to DECADE.

- (5) Because DECADE is designed to be an Inductive Energy Store (IES) generator, the effect of Plasma Opening Switch (POS) operation on PRS performance must be investigated. There are many uncertainties as to how POSs operate, and a number of POS models have been developed to describe this operation. One model, recently developed and suitable for use in a transmission line model description of power flow in DECADE, is discussed in Section V. During FY92, work was carried out to benchmark this model against experimental data obtained from Code 6770's Hawk POS. Work was also carried out to demonstrate a procedure for optimizing PRS performance within a power flow calculation using any POS model. This work will be published in the DoD's Journal of Radiation Effects.
- (6) Finally, a small effort continued in FY92 to develop scalable L-shell models for use in modeling the performance of PRS loads on DECADE. It is discussed in Section VI. This effort now makes use of atomic code capabilities that were developed at the Los Alamos National Laboratory. There are two problems of critical importance to DECADE that this work addresses. One is the problem of scaling L-shell emission behavior with atomic number. The other is the problem of studying L-shell burn-through in order to ignite the K-shell.

ADVANCED CONCEPTS THEORY ANNUAL REPORT 1992  
FINAL REPORT

I. DESIGNING WIRE ARRAY PRS EXPERIMENTS FOR PRESENT-DAY PULSED POWER GENERATORS

In March of 1992, a series of aluminum PRS experiments were designed for the SATURN machine at Sandia National Laboratory. The purpose of these experiments was to test the K-shell yield scaling that had been predicted for aluminum PRS loads,<sup>1</sup> that had been partially confirmed in experiments at Physics International Inc.,<sup>2</sup> and that were being used to predict PRS performance on DECADE. The basic concept being tested by the PI experiments was that, for efficient production of K-shell emission, a z-pinch array load had to be imploded to a final kinetic energy per ion,  $K_i$ , in excess of (and usually a small multiple of) a minimum energy,  $E_{min}$ , which scales with the atomic number,  $Z$ , of the load:

$$E_{min} = 1.012Z^{3.662} \text{ eV/ion.}$$

For aluminum, this minimum energy is approximately 12 keV/ion. The dimensionless parameter,  $\eta$ , defined by  $\eta \equiv K_i/E_{min}$ , thus should satisfy the criterion,  $\eta > 1$ , i.e.,  $K_i > 12 \text{ keV/ion}$  for aluminum.

In Ref. 1, MHD calculations had been carried out that showed how the K-shell yield from aluminum would scale with  $m$ , the imploded array mass per unit length, when  $\eta$  was held constant or with  $\eta$  when  $m$  was held constant. These calculations, which were carried out using classical plasma conductivities, produced hard implosions, i.e., implosions in which the plasma assembled on axis into a tight pinch of radius on the order of 0.1 mm. The experiments that were conducted at PI to test the validity of the calculated yields were not designed to hold either  $m$  or  $\eta$  constant. In them,  $m r_0^2$  was held roughly constant, where  $r_0$  is the initial radius of the imploded array. This condition corresponds to holding either  $K_T$ , the total kinetic energy of the implosion, or the product  $m\eta$  roughly constant. Scaling relations had been derived from the MHD calculations which predicted that the yields in the PI experiments would be roughly constant as well, corresponding to a fixed fractional ( $\sim 30\%$ ) conversion of kinetic energy into K-shell x-rays for all implosions of different radii,  $r_0$ , for which  $m r_0^2 = \text{constant}$ .

The PI experiments confirmed that, when the condition,  $\eta > 1$ , was satisfied, the pinch behaved as an efficient bulk K-shell emitter with, at minimum, the kinetic energy conversion efficiencies predicted by the calculations. However, two important differences between theory and experiment were observed. First, the K-shell yields were not flat, but had a peak for small  $\eta$  values ( $\eta \sim 2$  or  $3$ ), corresponding to a kinetic energy conversion efficiency of  $\geq 100\%$ , which is a theoretical impossibility. Second, the experimental implosions were much softer than the calculated implosions, i.e., they assembled on axis with radii on the order of 1 mm. The first difference suggests the conjecture that an anomalously high amount of Ohmic heating occurs under certain plasma conditions on axis as the current continues to cook the pinch. The second points to the conjecture that the implosions have anomalously high (MHD turbulence induced) viscosities and heat conductivities as well. Calculations utilizing enhanced electrical resistivities, viscosities, and heat conductivities appear to confirm these conjectures; however, more experimental guidance is needed to confirm the use of these effects in larger current pulsed power machines.

Thus, the first rationale for carrying out experiments on SATURN was to determine how the experimental results of Double EAGLE would scale to higher currents and larger imploded

aluminum masses. Because SATURN is a much softer machine than Double EAGLE, (since the PRS load implosion dynamics reacts back on the current flowing through the load much more strongly in SATURN than in Double EAGLE), it was important to design the SATURN experiments using the lumped circuit model for SATURN. The same procedure would be needed for Double EAGLE if greater control of the experimental parameters is required than was achieved in the Ref. 2 experiments.

The circuit model that was used to design the SATURN experiments is shown in Figure 1 of Ref. 3. The pulsed power generator is described as a time dependent voltage source,  $V(t)$ , driving a line resistance,  $Z_0$ , a line inductance,  $L_p$ , and a dynamic imploding z-pinch load with a time dependent inductance,  $L(r(t))$ . By using a slug model description of the dynamic load to determine  $r(t)$ , the location of the shell of imploding plasma, the PRS load dynamics can be initially simplified to the problem of solving the following two equations of motion:<sup>3</sup>

$$L_T \frac{dI}{dt} + \left( Z_0 - L_0 \frac{1}{r} \frac{dr}{dt} \right) I = V(t), \quad (1)$$

$$m \frac{d^2 r}{dt^2} = - \frac{L_0}{2\ell} I^2 \frac{1}{r}, \quad (2)$$

where  $I(t)$  is the current flowing through the load,  $L_T \equiv L_p - L_0 \ln(r/r_0)$ ,  $L_0 \equiv (1 - 1/N)(\mu_0 \ell)/(2\pi)$ ,  $N$  is the number of wires in the array,  $\ell$  is the length of the array, and  $\mu_0 = 4\pi 10^{-7}$  henry/m. The inductance of the load is given by  $L = -L_0 \ln(r/r_0)$ . A set of four benchmark calculations were carried out to test the use of this circuit model to explain previous PRS implosion data that had been taken at the SATURN facility.<sup>4</sup> The benchmark worked well. The predicted implosion times, total implosion kinetic energies, and kinetic-energies-per-ion were in accord with experimental observations.

Three sets of experiments were planned. They were designed using commercially available aluminum wire sizes, and, in an attempt to achieve maximum implosion symmetry, the arrays were taken to contain 24 wires. The first set of experiments were designed to closely parallel the Double EAGLE experiments so that direct inferences as to how the K-shell yields were scaling to higher mass loads could be made. Therefore, as in the Double EAGLE experiments, the initial array diameters were taken to be  $< 2$  cm. In the first set of experiments, the total kinetic energy generated in each implosion was 170 kJ and  $\eta$ 's ranged in value from less than 1 to 6. If 30% of the kinetic energy could be converted to K-shell emission, the minimum expected output of K-shell x-rays in these experiments would be 51 kJ. Eqs. (1) and (2) describe the dynamics of hard MHD implosions only to the point where the plasma is close enough to the axis to generate a back pressure comparable to the  $j \times B$  forces, which are described by the  $I^2$  term on the right side of Eq. (2). Thus, the solutions to Eqs. (1) and (2) must be terminated before this condition ensues. The parameters of the first set of SATURN experiments that are given in the following table were calculated from Eqs. (1) and (2) by terminating the solution in each case at  $r(t_{imp}) = 1.5$  mm, where  $t_{imp}$  is by definition the implosion time.

The calculations in Ref. 1 also suggested that K-shell yields would continue to rise as a function of  $\eta$  for a fixed  $m$  until fairly large  $\eta$  values were reached. For example, peaks in the calculated yields occurred at  $\eta = 7.5$  and  $\eta = 27.5$  for  $m = 60$  and  $200 \mu\text{g/cm}$  respectively.

### SATURN PRS Experiments

K.E. = 170 kJ,

Return current radius = 1.4 cm, array length = 2.0 cm

Wire Diam (mil)	Wire Mass ( $\mu\text{g/cm}$ )	Array Rad (cm)	$\eta$	# Wires
2.5	2050	0.638	0.95	24
2.0	1310	0.67	1.6	24
1.7	950	0.7	2.2	24
1.5	740	0.73	2.7	24
1.2	470	0.79	4.2	24
1.0	330	0.86	6.0	24

Such large  $\eta$  values could be reached on the SATURN generator by going to large aspect ratio implosions, i.e., those implosions for which the initial array diameter was larger than 2 cm. In argon and krypton gas puff experiments, large aspect implosions had been observed to produce the highest yields. This observation provided a second rationale for proposing a second set of large aspect ratio SATURN experiments in which the total kinetic energy generated in the implosions was held fixed at 230 kJ. A 30% conversion of this energy to kilovolt x-rays would produce a K-shell yield of 69 kJ. The following table lists the calculated parameters for these large aspect ratio aluminum array implosions:

### SATURN PRS Experiments

K.E. = 230 kJ,

Return current radius = 2.4 cm, array length = 2.0 cm

Wire Diam (mil)	Wire Mass ( $\mu\text{g/cm}$ )	Array Rad (cm)	$\eta$	# Wires
1.5	740	1.1	3.5	24
1.2	470	1.145	5.6	24
1.0	330	1.21	8.3	24
0.75	185	1.365	15	24
0.7	160	1.405	17	24
0.6	120	1.52	22	24

A third set of special case experiments was also proposed. For example, by going out to a radius of  $r_0 = 1.7$  cm, a large implosion velocity and a total kinetic energy of 280 kJ could be generated using either aluminum or titanium wires. The final velocity achievable in such an implosion would be sufficient to generate an  $\eta$  larger than 1 for titanium (for which  $E_{min} = 83.4$  keV/ion) provided the finest 0.8 mil titanium wire is used. The masses of these two implosions, listed in the following table, were large enough to anticipate that good conversion of kinetic energy into kilovolt x-rays was possible following assembly on axis of the pinch:



### SATURN PRS Experiments

K.E. = 280 kJ,      Return current radius = 3.0 cm, array length = 2.0 cm

Element	Wire Diam (mil)	Wire Mass ( $\mu\text{g/cm}$ )	Array Rad (cm)	$\eta$	# Wires
Al	1.2	473	1.7	7	24
Ti	0.8	350	1.7	2.7	24

Two other special array experiments were designed to simulate an exploding wire by positioning the wires so close to the axis that they would, immediately upon exploding, form a plasma on axis with sufficient back pressure to negate the generation of kinetic energy. The wire's mass loading was chosen so that the wires would quickly assemble on axis into an anticipated Bennett equilibrium. Under these conditions, the ability of Ohmic heating to ionize the bulk plasma into the K-shell could be observed as a test of the conjecture that a strong anomalous heating could be generated in a z-pinch on axis. The parameters that were chosen for these two experiments are :

### SATURN PRS Experiments

K.E.  $\cong$  0 kJ,      Return current radius = 1.4 cm, array length = 2.0 cm

Element	Wire Diam (mil)	Wire Mass ( $\mu\text{g/cm}$ )	Array Rad (cm)	$\eta$	# Wires
Al	1.7	950	0.2	0	24

K.E.  $\cong$  0 kJ,      Return current radius = 0.5 cm, array length = 2.0 cm

Element	Wire Diam (mil)	Wire Mass ( $\mu\text{g/cm}$ )	Array Rad (cm)	$\eta$	# Wires
Al	2.0	1310	0.2	0	24

Finally, the array parameters for one last (large aspect ratio) special case were calculated. The goal in this experiment was to implode a 3 cm long aluminum array of sufficient mass and  $\eta$  in order to achieve the largest possible yield in these experiments. The total kinetic energy generated in this case is 330 kJ; a 30% conversion efficiency would yield 99 kJ of kilovolt x-rays. The parameters for this case are:

## SATURN PRS Experiments

K.E. = 330 kJ,      Return current radius = 2.4 cm, array length = 3.0 cm

Element	Wire Diam (mil)	Wire Mass ( $\mu\text{g/cm}$ )	Array Rad (cm)	$\eta$	# Wires
Al	1.2	473	1.5	5.8	24

Shortly after the above experiments had been completed, R. Spielman at Sandia indicated that a significant improvement in aluminum K-shell yield had been attained on Saturn in the 0.86 cm radius, 330  $\mu\text{g/cm}$  shot (an increase of 30 to 40% over previous yields). An improvement of this order was indicated by 1-D MHD calculations that focused on the thermalization of kinetic energy as the primary mechanism for producing K-shell emission. These same calculations predict that the yield should continue to increase for the larger aspect ratio implosions (array diameters  $> 2$  cm); however, R. Spielman also indicated that these large aspect ratio Al experiments, just completed in August, 1992, did not work as well as hoped. When these experiments were planned in March the goal was to tradeoff load mass for implosion velocity, using the early hard implosion calculations as a guide. They had showed K-shell yield increasing as a function of  $\eta$  up to fairly high values. Implosion symmetry is very important in implosions that start from large radii, however, and it was hoped that, by using 24 wires, the SATURN experiments had a better chance of success than earlier large radius experiments on Double EAGLE or BJ5. However, the pinhole pictures of these high aspect ratio implosions apparently showed poor implosion quality.

Based on these very preliminary and undocumented findings, a new set of aluminum PRS experiments was planned for the Phoenix facility at the Naval Surface Weapons Center. A circuit model for Phoenix was obtained from P. Corcoran of PSI. When run in short circuit mode, it produced about 5.3 MA peak current with a risetime of approximately 100 ns. Efforts to design some experiments for Phoenix were then begun. They were influenced by two other important recent findings:

(1) Recent large aspect ratio experiments with krypton at PI were very successful (in contrast to Al on SATURN), i.e., the peak in the kilovolt yield curve (L-shell radiation) occurred at a 4 cm nozzle diameter. This is a larger diameter than was used on any of the Sandia wire experiments. Therefore, all loads being equal, the Sandia experiments should have mimicked the success of the PI krypton experiments. Apparently, even 24 wires with 6 or 8 return current posts do not perform as well as one cylindrical flow of gas with the same return current posts. The important question is why not?

(2) Calculations on argon that were carried out for the BEAMS 92 conference in May showed that, for soft implosions, load mass was more important than  $\eta$ , i.e., the K-shell yield curves saturated rapidly with  $\eta$  ( $\eta \leq 6$ ) for the kinds of masses used in the SATURN and PI experiments. (For the PI krypton experiments, we found that the L-shell yield peaked for  $\eta \sim 1$ .) These soft implosion (also called turbulent) results are shown in Figure 1 in comparison to the 200  $\mu\text{g/cm}$  hard implosion (non-turbulent) result. In a soft implosion calculation  $\eta^*$  represents the (normalized)

total energy coupled to the load: kinetic +  $pdV$  work + Ohmic heating. As Figure 2 shows, in a soft implosion, only 55 to 60% of the coupled energy is kinetic, which accounts for the softness of the implosion.

We conclude from these findings that large aspect ratio wire experiments should be carried out in the future at SATURN, Phoenix, and Double EAGLE to test a different machine/load tradeoff: that between mass and implosion radius. Experiments in which  $\eta$  is fixed at small values from 2 to 6 should be done with an increasing array mass (or increasing number of wires) in order to generate increasing kinetic energies. A series of such Phoenix experiments were designed in September. Like the SATURN experiments, they utilize standard, commercially available, wire sizes, and they are tailored to the fact that Phoenix has eight return current posts. The proposed aluminum wire array parameters are listed in the following three tables:

### Phoenix Aluminum Experiments

$\eta = 2$ , Return current radius = 3.0 cm, array length = 2.0 cm

Wire Diam (mil)	Wire Mass ( $\mu\text{g}/\text{cm}$ )	Array Rad (cm)	K.E. (kJ)	# Wires
1.0	219	0.75	38	16
1.5	246	0.79	42	8
1.2	315	0.79	54	16
1.7	316	0.9	54	8
2.0	438	1.15	74	8
1.2	473	1.325	82	24

$\eta = 3$ , Return current radius = 3.0 cm, array length = 2.0 cm

Wire Diam (mil)	Wire Mass ( $\mu\text{g}/\text{cm}$ )	Array Rad (cm)	K.E. (kJ)	# Wires
1.2	158	0.87	40	8
0.75	185	0.93	47	24
1.0	219	1.02	57	16
1.5	246	1.1	63	8
1.2	315	1.32	81	16

These experiments differ from the SATURN experiments because, as the array diameter is increased to generate more total kinetic energy, the  $\eta$  values (i.e. the final implosion velocities) are kept moderately low while the array mass is increased. The large array diameter SATURN experiments were designed for roughly the same mass values that are shown in the above tables,

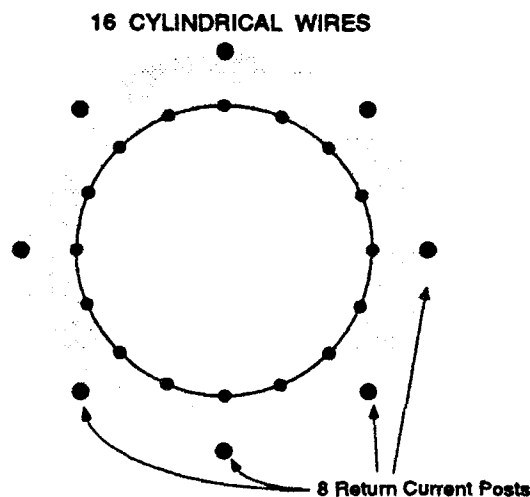
## Phoenix Aluminum Experiments

$\eta = 4$ , Return current radius = 3.0 cm, array length = 2.0 cm

Wire Diam (mil)	Wire Mass ( $\mu\text{g}/\text{cm}$ )	Array Rad (cm)	K.E. (kJ)	# Wires
1.2	158	1.08	54	8
0.7	161	1.08	55	24
0.75	185	1.17	63	24
1.0	219	1.32	75	16
1.5	246	1.55	85	8

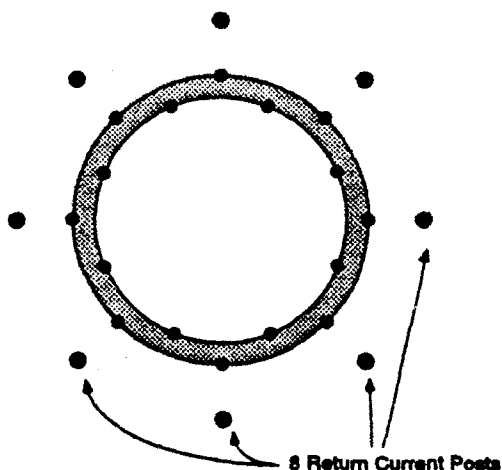
but for much larger  $\eta$ s. Again, earlier aluminum experiments at Double EAGLE had shown peak K-shell yields for  $\eta$  values of 2 to 3, and they converted close to 100% of the implosion kinetic energy to K-shell x-rays. If similar results could be obtained in these Phoenix experiments, they might produce maximum K-shell yields of between 70 to 80 kilojoules.

Because it is important to discover why K-shell yields tend to fall off as the array diameter is increased, it was also proposed that one or more of the large aspect ratio implosion cases in the above list of experiments be carried out in two geometries. These geometries are displayed in the following three pictures.

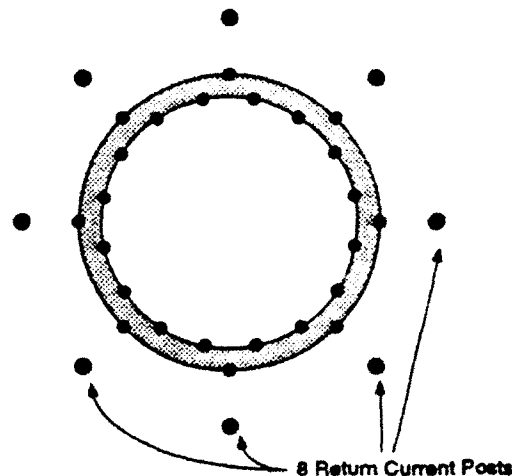


It is standard practice to mount the array wires on the same circle as shown in the first picture. However, in this case, the wires nearest the return current posts will experience the strongest  $\mathbf{j} \times \mathbf{B}$  forces and will be accelerated to the axis sooner than the other wires. Thus, a symmetric beginning for the wires will not lead to a symmetric ending on axis, a condition that is essential for

16 CONCENTRIC WIRES, 8 WIRE OFFSET



24 CONCENTRIC WIRES, 16 WIRE OFFSET



the efficient production of K-shell radiation. For this reason, we propose that a second geometry be employed, illustrated above in the lower two pictures depending on the number of wires. In this case, the wires are mounted on two concentric circles. The wires nearest the return current posts are mounted on the outer circle, and the other wires are mounted nearer to the axis on the inner circle. The goal of these experiments, like the goal of the tilted nozzle puff gas experiments recently conducted at PI, is to determine whether the K-shell yield will increase as the inner circle radius is reduced. One might begin with a 1/2 mm radial separation between the inner and outer circles, and then double it to 1 mm, and then double it again to 2 mm, for example.

A circuit model for Double EAGLE was also used to design a set of experiments for Double EAGLE that are the equivalent of the above Phoenix experiments. They take into account the fact that Double EAGLE has only 6 return current posts, while Phoenix has 8, and they again make use of commercially available wire sizes. Since the idea for these experiments is to get large aspect ratio aluminum experiments to work more efficiently, the comparison of well diagnosed Double EAGLE with comparable Phoenix experiments should help us to understand what the problems are in achieving this performance. As in the Phoenix experiments, it will be important to understand the role of mass / kinetic energy tradeoffs in achieving these efficiency improvements. If these experiments can be made to work as well as earlier PI experiments, then 100% of the kinetic energies listed below would be converted to K-shell x-rays, and Double EAGLE would nearly double its previous maximum Al K-shell yield. The proposed experiments are listed in the following three tables:

Because Phoenix is a newly designed and operated machine, its lumped circuit model has yet to be tested. Another reason, therefore, for comparing Double EAGLE and Phoenix experiments is to obtain an important benchmark for the Phoenix circuit by way of Double EAGLE. The earlier experiments that were carried out at Double EAGLE were both well diagnosed and, consequently, well benchmarked. Hence, they have provided a valuable validation of the Double EAGLE lumped circuit model. We demonstrate this fact with the following example. Additionally, it illustrates

## Double EAGLE Aluminum Experiments

$\eta = 2$ , Return current radius = 2.0 cm, array length = 2.0 cm

Wire Diam (mil)	Wire Mass ( $\mu\text{g}/\text{cm}$ )	Array Rad (cm)	K.E. (kJ)	# Wires
1.0	164	0.8	28	12
1.2	236	0.91	41	12
2.0	328	1.07	56	6
1.2	355	1.14	61	18

$\eta = 3$ , Return current radius = 2.0 cm, array length = 2.0 cm

Wire Diam (mil)	Wire Mass ( $\mu\text{g}/\text{cm}$ )	Array Rad (cm)	K.E. (kJ)	# Wires
1.2	118	0.92	30	6
1.0	164	1.04	43	12
1.5	185	1.09	47	6
1.2	236	1.26	61	12
1.0	246	1.3	63	18

$\eta = 4$ , Return current radius = 2.0 cm, array length = 2.0 cm

Wire Diam (mil)	Wire Mass ( $\mu\text{g}/\text{cm}$ )	Array Rad (cm)	K.E. (kJ)	# Wires
0.7	121	1.115	41	18
0.75	139	1.18	47	18
1.0	164	1.3	52	12
1.5	185	1.4	64	6

that the full capacity of Double EAGLE to produce K-shell emission from aluminum loads has yet to be realized. The aluminum experiments proposed above should, hopefully, demonstrate this fact. If not, then, they ought to provide us with some reasons why not.

In the following example, the circuit equations, (1) and (2) above, are used with the circuit elements appropriate to Double EAGLE. A systematic examination of the implosion dynamics up to, but just prior to, assembly on axis, is then carried out by varying the mass of the aluminum array. The experimental case in Ref. (2) being modeled is the one where 164  $\mu\text{g}/\text{cm}$  was imploded from a radius of 0.75 cm. From Ref. (2), the implosion time was observed to be 95 ns and the implosion produced 28 kJ of K-shell yield with an  $\eta$  value of 1.7. The results of the calculations that were

performed with the Double EAGLE slug model circuit equations are shown in Figs. (3)-(6).

As more mass is imploded from the same initial array radius (of 0.75 cm), one sees from Fig. (3) that the implosion time is stretched from 110 to 260 ns. Small mass implosions reach the axis early during the rise of the current pulse; whereas, the large mass implosions reach the axis late in the current pulse after it has peaked (see Fig. (4)). The labels, R, L, and G, in Figs. (3)-(6) place into correspondence the mass loadings with the three current traces and kinetic energies that are generated when the masses implode. Fig. (5) shows that the implosion, L, that produces the most kinetic energy ( $\sim 50$  kJ) corresponds to an implosion that occurs just after peak current at roughly 167 ns. However, in Fig. (6), one sees that this implosion has an  $\eta$  value of only 0.4 and, therefore, it should be a poor radiator of kilovolt x-rays. Thus, even though this particular choice of array parameters produces good coupling to the Double EAGLE generator and a near optimal amount of kinetic energy generation, it also produces a poor kilovolt x-ray radiator. The Double EAGLE load designs presented in the above tables were clearly designed to overcome this limitation. They were determined to optimize kinetic energy as well as kilovolt x-ray production. Unfortunately, the present impediment to their successful realization appears to be the requirement that they are initiated from array diameters larger than 2 cm. An important near term objective of the DECADE PRS program should be to remove this limitation.

Fig. (3) also shows an extrapolation of the mass versus implosion time curve to approximately the mass value of  $164 \mu\text{g}/\text{cm}$ . These slug model calculations then predict that this mass should implode to the axis in roughly 105 ns. As seen in Fig. (4), this time can easily be adjusted down to 95 ns. given the experimental uncertainty of identifying the beginning of the current pulse. When the kinetic energy curve is extrapolated to 105 ns in Fig. (5), it shows that 25 kJ of kinetic energy is generated in the experiment corresponding to a greater than 100% efficiency of converting kinetic energy to kilovolt x-rays. Fig. (6) confirms that a  $164 \mu\text{g}/\text{cm}$  aluminum implosion from a radius of 0.75 cm has enough implosion velocity to be a good K-shell radiator, i.e., in this case,  $\eta \geq 1.7$ .

Enhanced transport MHD calculations were performed to test the quality of the energy conversion to be expected in both the proposed Phoenix and Double Eagle aluminum experiments. These calculations were done for soft implosions in accord with the HEART Conference work to be published in the DoD Journal of Radiation Effects, i.e., the thermal conductivity was enhanced by a factor of 30, electrical resistivity was enhanced by 20, and the viscosity was enhanced by 25. The K-shell emission comes predominantly from thermalization of kinetic energy because the current is terminated when the voltage across the plasma diode reaches 3 MV. The Double Eagle calculations show that K-shell yields of 20 kJ/cm can be achieved. This is specifically true for the proposed experiment in which the mass loading is  $246 \mu\text{g}/\text{cm}$  and the array radius is 1.3 cm. Similar calculations made for previous Double Eagle experiments underpredicted the measured K-shell yield (by as much as 7 kJ/cm), especially for loads in excess of  $200 \mu\text{g}/\text{cm}$ . It is thought that current-on effects such as Ohmic heating are responsible for this under-prediction. If these same effects are present in the above proposed experiments, then one would predict that K-shell yields of 25 to 30 kJ/cm ought to be achieved. Similar calculations for Phoenix show that, without taking into consideration any current-on effects, K-shell yields of 30 kJ/cm are possible. This predicted yield is larger than the Double Eagle yield because of the larger current that Phoenix produces at current turn-off time. If these predictions are not observed, then they may provide an indicator for determining the propensities for the two machines to short-circuit in the diode region.

The above yield results represent what is believed to be achievable on Double EAGLE and Phoenix given that the load design promotes a symmetric implosion. Although detailed data analysis still needs to be performed on the SATURN aluminum experiments, it is believed that asymmetric behavior may be responsible for the fact that the larger aspect ratio wire loads did not perform as well as expected. Although large aspect ratio argon and krypton gas puff experiments at PI did exhibit symmetric implosion behavior and produce K-shell and L-shell yields as large or larger than predicted, these encouraging results are not yet reproducible with wire arrays. Thus, much experimental and theoretical load design work needs to be done if DECADE is to reach its full potential as an x-ray simulator, especially using wire arrays.

#### REFERENCES

1. K. G. Whitney, J. W. Thornhill, J. P. Apruzese, and J. Davis, *J. Appl. Phys.* **67**, 1725 (1990); J. W. Thornhill, K. G. Whitney, and J. Davis, *J. Quant. Spectrosc. Radiat. Transfer* **44**, 251 (1990).
2. C. Deeney, T. Nash, R. R. Prasad, L. Warren, K. G. Whitney, J. W. Thornhill, and M. C. Coulter, *Phys. Rev. A* **44**, 6762 (1991).
3. J. Katzenstein, *J. Appl. Phys.* **52**, 676 (1981).
4. R. B. Spielman, R. J. Dukart, D. L. Hanson, B. A. Hammel, W. W. Hsing, M. K. Matzen, and J. L. Porter, "Dense Z-Pinches, Second International Conference" ed. by N. R. Pereira, J. Davis, and N. Rostoker, *AIP Conference Proc.* **195**, 3 (1989).



# Turbulent and Non-Turbulent K-shell Yields Versus Mass and Coupled Energy ( $\eta^*$ )

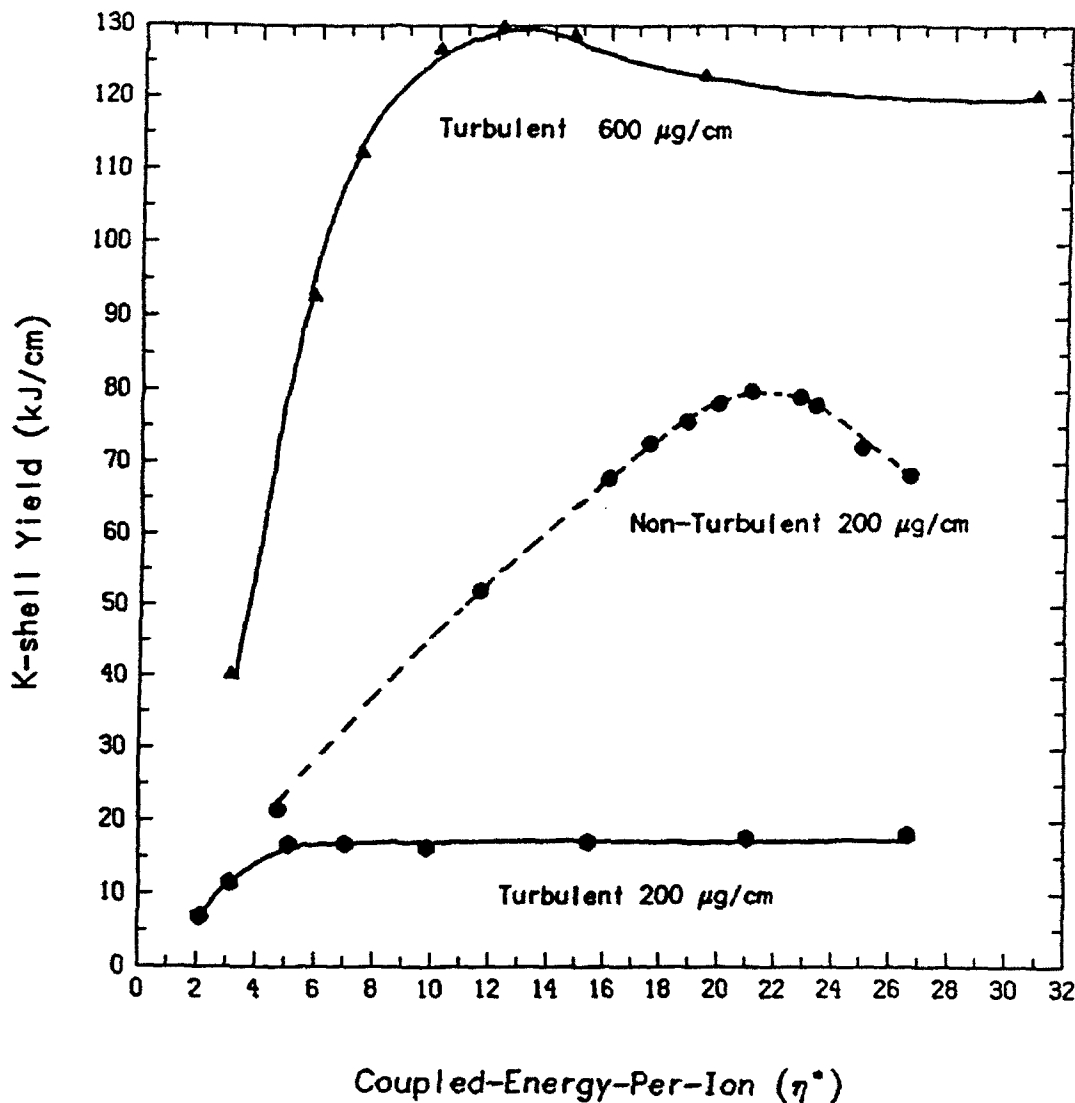


Figure 1.

- Loads are driven by linearly ramped current profiles from an initial radius of 1.0 cm. The current is terminated at the time a 0-D slug calculation predicts the outer radius of the load is within 0.14 cm of the axis.
- $\eta^*$  is the coupled energy-per-ion normalized by the minimum energy needed to ionize to the K-shell (38 keV for argon).

$$\eta^* = (\text{JxB work} + \text{ohmic heating}) / (\text{number of ions} \times 38 \text{ keV})$$

- These K-shell yields also include  $> 1\text{keV}$  radiation, however, the  $> 3 \text{ keV}$  radiation represents at least 85% of the K-shell yield.

# Ratio of Peak Kinetic Energy to Coupled Energy Versus Mass and Coupled Energy ( $\eta^*$ )

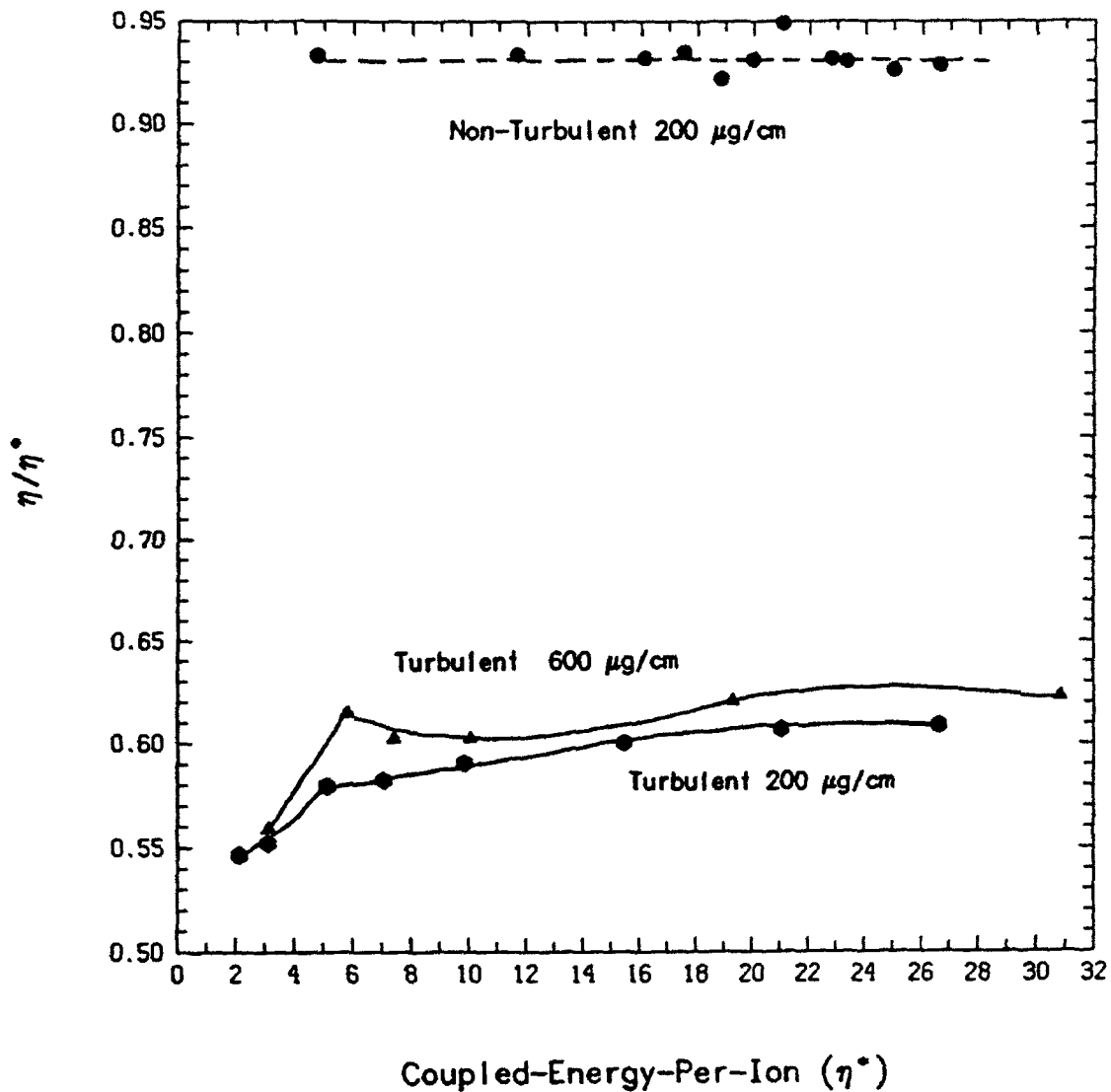


**Figure 2.**

- $\eta^*$  is the coupled energy-per-ion normalized by the minimum energy needed to ionize to the K-shell (38 keV for argon).

$$\eta^* = (\text{JxB work} + \text{ohmic heating}) / (\text{number of ions} \times 38 \text{ keV})$$

- $\eta$  is the peak kinetic-energy-per-ion normalized by the minimum energy needed to ionize to the K-shell (38 keV for argon).

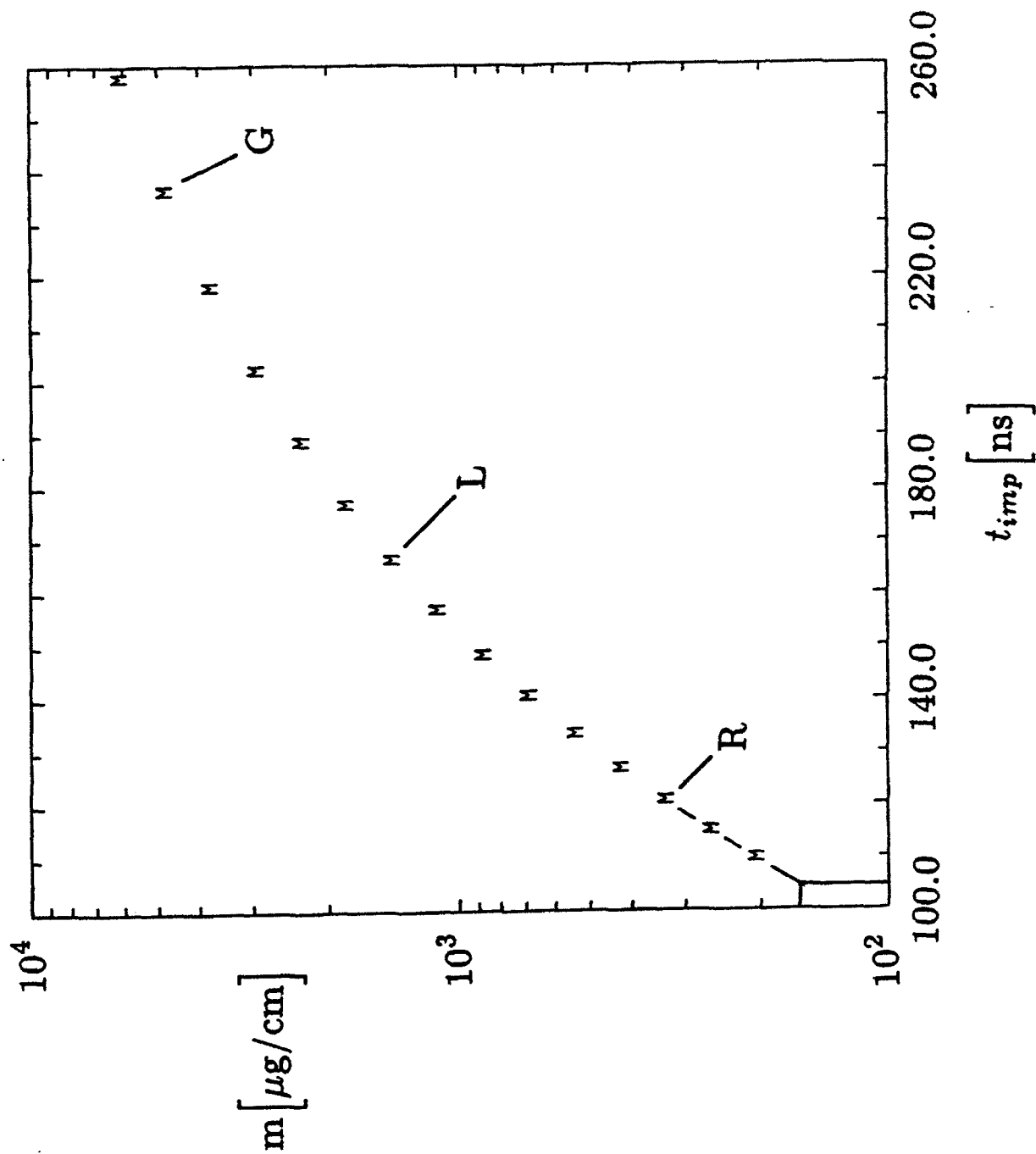


Figure 3. The mass of a number of aluminum Double EAGLE implosions is plotted against the time of implosion. The initial array radius is 0.75 cm, the array length is 2 cm, and the return current radius is 2 cm.

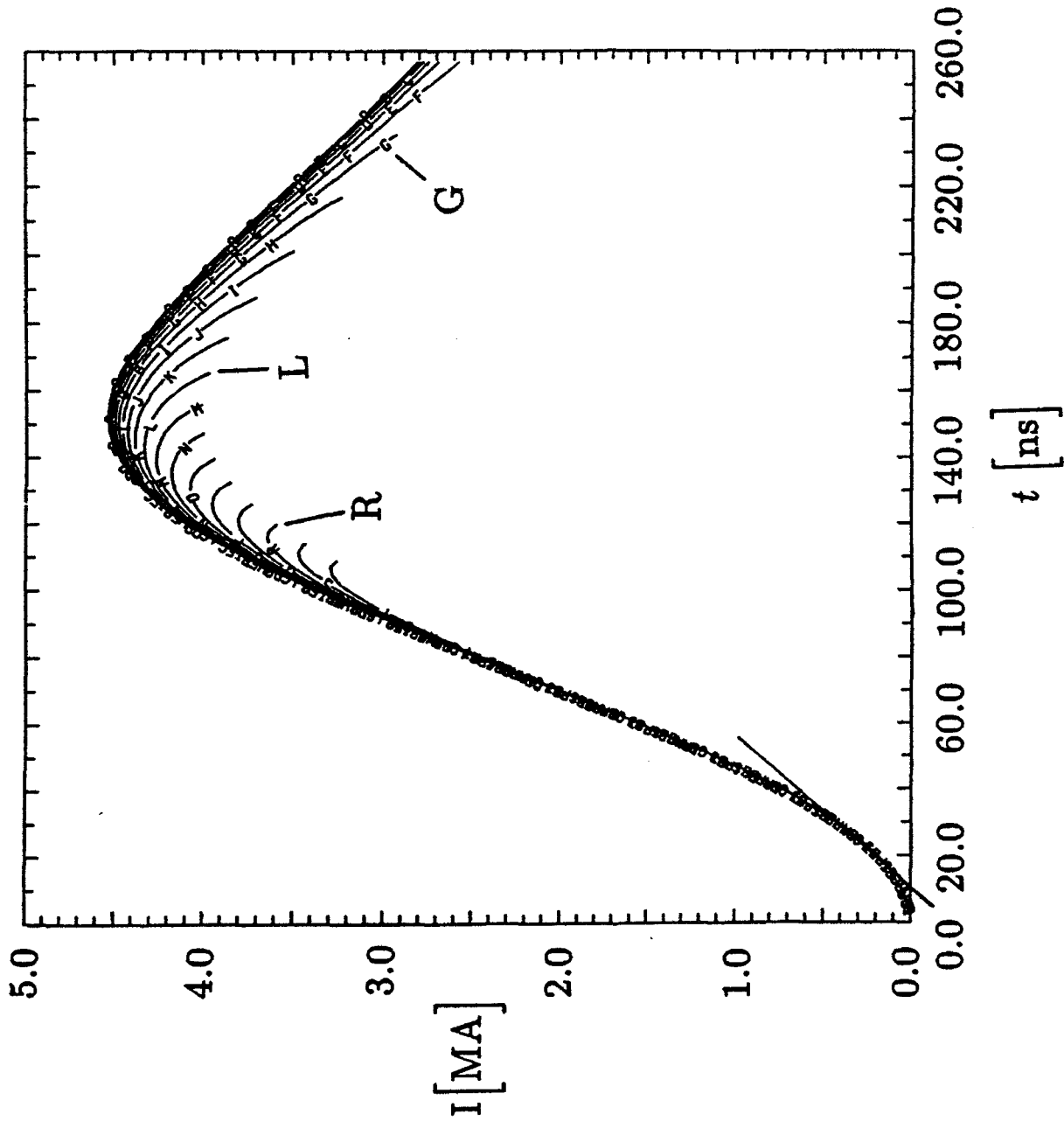


Figure 4. The current traces of the different mass implosions of Fig. (3) are shown with three labels, R, L, and G, enlarged to allow easy correspondence to be made with the masses in Fig. (3). The initial array radius is 0.75 cm, the array length is 2 cm, and the return current radius is 2 cm.

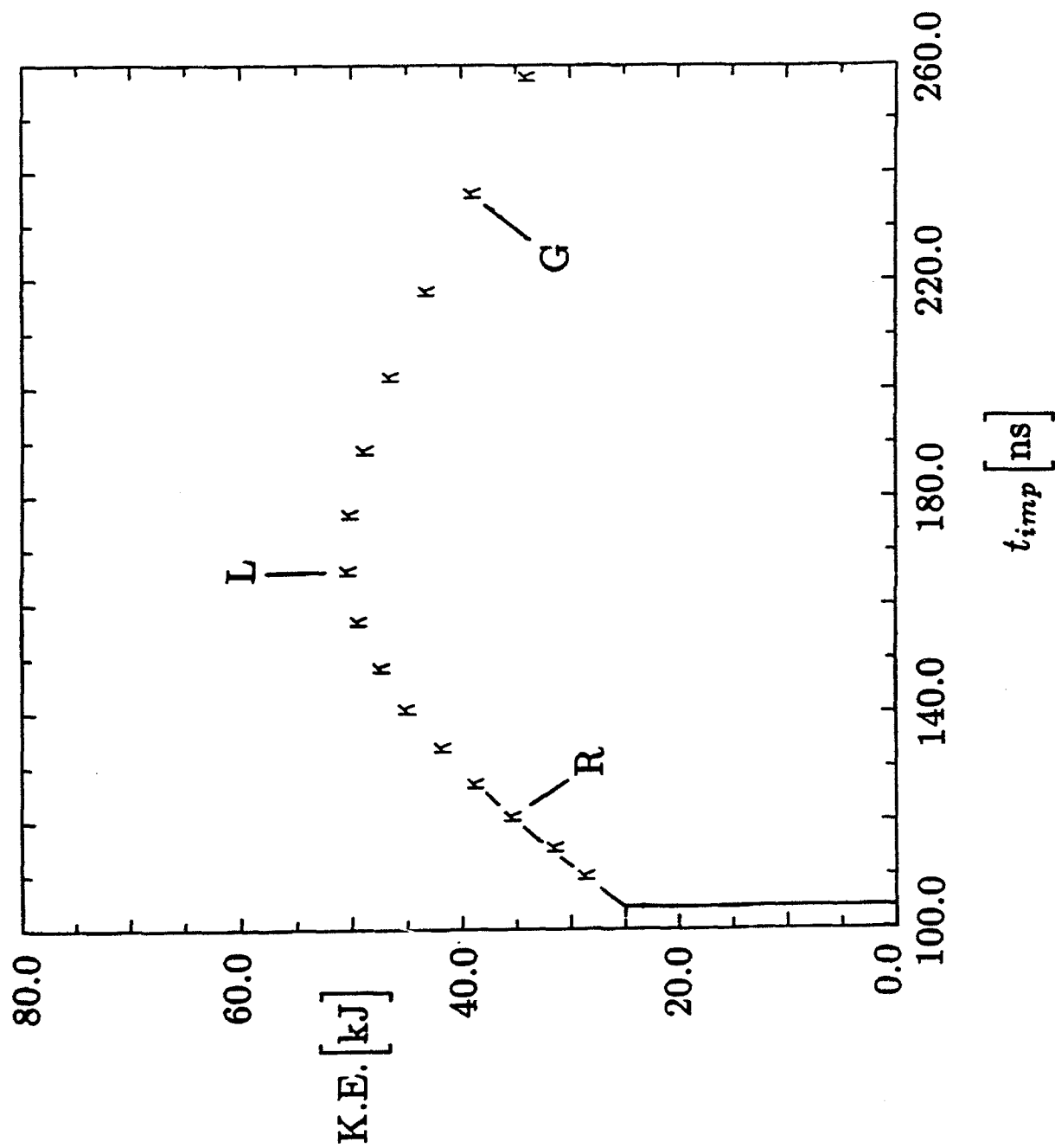


Figure 5. The total kinetic energies generated in each of the Figs. (3) and (4) implosions are shown as a function of implosion time. The initial array radius is 0.75 cm, the array length is 2 cm, and the return current radius is 2 cm.

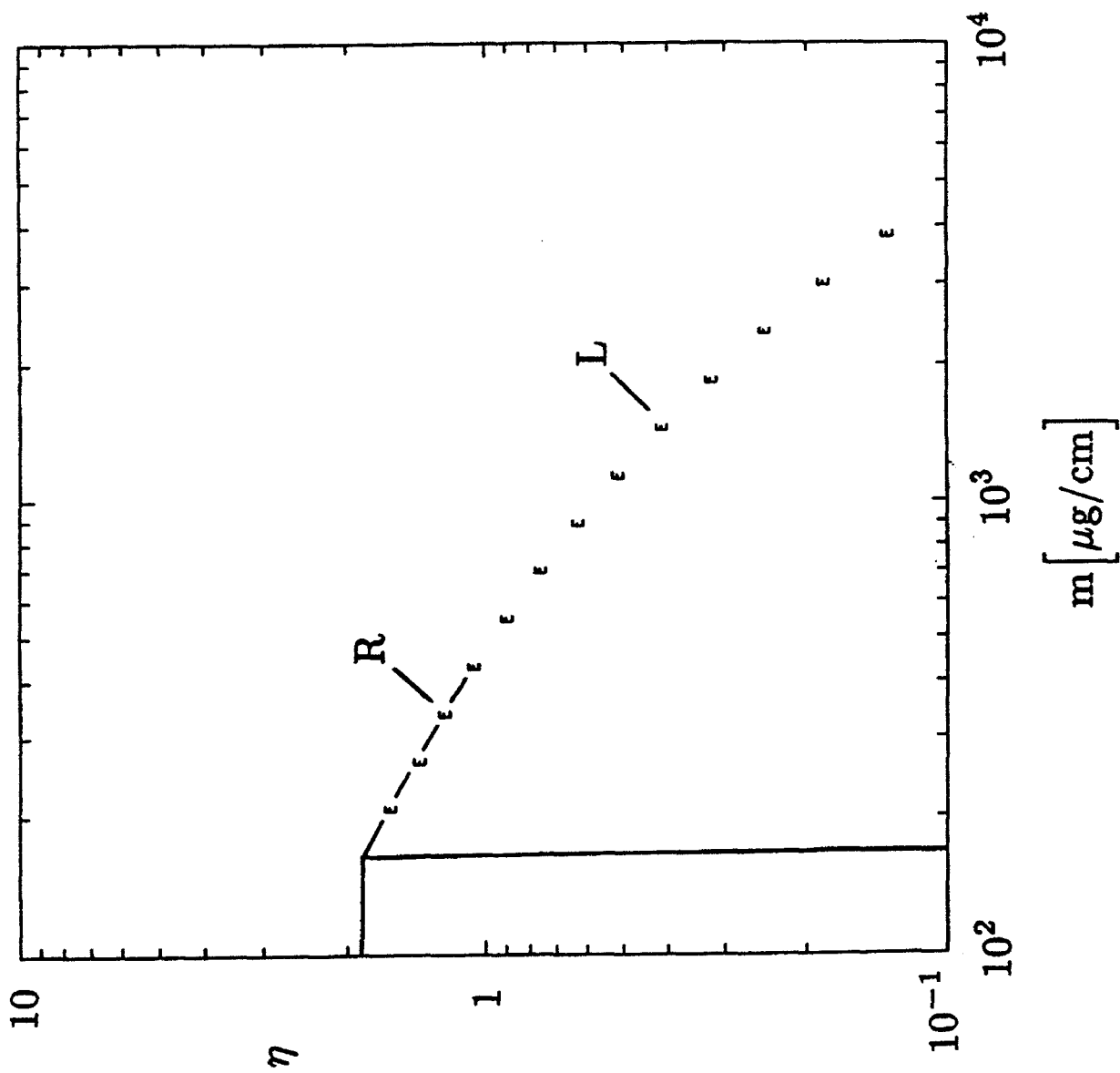


Figure 6. The  $\eta$ 's generated in each of the Figs. (3) and (4) implosions are plotted as a function of the imploded mass. The initial array radius is 0.75 cm, the array length is 2 cm, and the return current radius is 2 cm.

## II. COMPARISON of PI ARGON EXPERIMENTS WITH 1-D ENHANCED TRANSPORT CALCULATIONS

### INTRODUCTION

In work that was presented at the 1992 HEART and BEAM conferences,<sup>1,2</sup> a phenomenological treatment of hydromagnetic turbulence and microturbulence was included in the standard non-turbulent 1-D MHD model in order to obtain better agreement with experimental measurements than had been provided by the standard 1-D model. Historically the non-turbulent model over-predicts the experimental stagnation densities and radiative powers by orders of magnitude. The phenomenological treatment consisted of enhancing transport by using multipliers for the classical transport coefficients of resistivity, viscosity, and thermal conduction. A choice of coefficients was made so that the calculated stagnation ion densities and electron temperatures approximated those measured in a series of Double Eagle argon experiments.

The results of the HEART and BEAM's work showed: (1) Because of the softer implosions (lower stagnation ion density) generated by enhancing the transport coefficients, the turbulent calculations require more mass than non-turbulent ones to reach an efficient K-shell emission scaling regime ( $> 20\%$  conversion of kinetic energy into K-shell photons). (2) The range of values for  $\eta$  (kinetic-energy-per-ion normalized to the amount of energy required to ionize to the K-shell) over which efficient scaling can be obtained for a given mass is limited to low  $\eta$  values in the enhanced transport scaling calculations. (3) When turbulence is included, the onset of K-shell burn-through and lower plasma density severely limit the maximum K-shell yield that is attainable from a given mass (as opposed to the non-turbulent case). However, other than these quantitative differences between turbulent and non-turbulent transport models, the results of earlier non-turbulent transport scaling work are still largely valid. In particular, the existence of an efficient scaling regime for producing K-shell radiation, which is a function of mass loading, machine energy, and atomic number of the material, is still supported by the enhanced transport calculations. This is important because it provides strong theoretical support for the belief that high  $Z$  experiments performed on powerful PRS machines such as DECADE will exhibit efficient K-shell x-ray production. Thus, enhanced transport calculations can provide valuable guidance for designing future experiments to be performed on these high power machines.

The turbulence coefficients used in the HEART and BEAM's studies were obtained from stagnation density and temperature comparisons with PI experiments all having the same 52  $\mu\text{g}/\text{cm}$  argon load. We have since extended the HEART and BEAM's work by examining how this determination of turbulence coefficients is altered as the mass of the argon load used in the experiments is increased substantially above 52  $\mu\text{g}/\text{cm}$ . In this case 1-D simulations are performed of Double Eagle argon experiments having mass loads of 42, 85, 125 and 165  $\mu\text{g}/\text{cm}$ . In each simulation the transport coefficients are varied until a reasonable match with experiment is found. The technique (HEART paper) of multiplying the classical coefficients by constant multipliers is utilized; however, in the interest of limiting the parameter space of possible coefficients it was assumed, somewhat arbitrarily, that the mechanism responsible for enhanced viscosity is also responsible for an equal enhancement of ion thermal conduction. The calculated quantities that are matched to the experimental data are the mass averaged temperature and density of the K-shell emitting region. The latter quantities were inferred from the measured K-shell spectrum, pulsewidth, and pinhole picture. The MHD model is the same as that described in the HEART paper. All of the simulations employ a circuit model of Double Eagle so that the driving current and the plasma load dynamics in the calculation is the same as the machine dynamics. The calculations are begun at the same radius as the experiments with 93 percent of the mass concentrated within an annular shell having the identical thickness as the 0.4 cm nozzle exit. The remaining mass is distributed with a mass density that exponentially decays towards the axis. This initialization procedure provides for numerical stability and it also simulates the backpressure effects of plasma that is blown toward the axis by the gas jets.

A major premise of past work<sup>1-4</sup> and also of this present analysis is that thermalization of kinetic energy determines the state of the stagnation plasma. This is insured in the calculations by terminating the current (current-off calculation) when the voltage across the diode reaches 3 MV. Because there is no current beyond a certain early time in the on-axis dynamics, no attempt is yet made to model ohmic heating, anomalous heating, and plasma confinement by magnetic fields during these latter stages of the implosion. All of these phenomena will tend to increase the K-shell yield.

The HEART study showed that when late time current effects are neglected, enhanced resistivity does not play as strong a role as enhanced viscosity and enhanced ion and electron thermal conduction in lowering stagnation ion densities. In this regard, we are going to take the point of



view that prior to stagnation, most of the major differences between experiment and non-enhanced transport calculations are attributable to macroscopic turbulence. Thus, only the artificial viscosity  $\nu$ , which heats directly the ions, and ion thermal conductivity  $\kappa_i$  are enhanced in these calculations. Our reason for not enhancing the electron thermal conduction is discussed in more detail at the end of the results section.

Note, since late time current effects are neglected and also because it is the nature of a 1-D model to neglect zippering and other large scale multi-dimensional macroscopic motion (all of which can significantly lengthen the time scale over which kinetic energy is thermalized and consequently can broaden the radiation pulse) it is unreasonable to expect exact agreement between calculations and experiment. As mentioned at the beginning of the introduction we are primarily seeking a reduction in the 2 - 3 order of magnitude differences in density and radiative powers that exists between 1-D non-turbulent calculations and experiments.

## RESULTS

The results of this theoretical and experimental comparison are summarized in Tables 1 through 4 for the 42, 85, 125, and 165  $\mu\text{g}/\text{cm}$  argon loads, respectively. The mass of each plasma load was determined from a 0-D slug model analysis of the experimental implosion time. The K-shell yields were measured using kapton filtered tantalum calorimeters and also by numerical integration of filtered x-ray diode (XRD) emission power signals. The spatial and temporal behavior of K-shell emission was determined using the arrangement of Deeney et. al.<sup>5</sup> Applying the analysis technique of Coulter et. al.<sup>6</sup> to the time integrated and resolved K-shell data provided the density, mass fraction, and electron temperature of the K-shell emission region. This required knowledge of the outer radius of the K-shell, the K-shell power, and the  $\text{He}_\alpha$  to  $\text{Ly}_\alpha$  line ratio.

As in the HEART and BEAM's work, it was possible to find a broad range of values in  $(\kappa_i, \nu)$  parameter space that produced stagnation temperatures and ion densities in acceptable agreement with experiment. Over an appreciable time span during peak K-shell emission, electron temperatures could be matched within 25% and ion densities could be matched within a factor of 3. In particular, multiples of >10 to 25 times the classical conduction and viscosity coefficients for the 42  $\mu\text{g}/\text{cm}$  load, multiples of 25 to 40 for the 85  $\mu\text{g}/\text{cm}$  and 125  $\mu\text{g}/\text{cm}$  load and multiples of >25 to 50 for the 165  $\mu\text{g}/\text{cm}$  load all produced acceptable agreement with experimental

stagnation densities and electron temperatures in the K-shell emission region. Based on this limited data set it appears that the amount of enhanced transport required to give experimental agreement could be increasing by a factor of 2 over the range of masses from 42 to 165  $\mu\text{g}/\text{cm}$ . However, this upward variation is expected to saturate with increasing mass because enhancements of 40 or greater over classical ion conduction are close to the limit of physically allowable conduction. To insure that calculations do not go beyond the bounds of physical possibility, flux correctors will be utilized in future models.

The most representative calculation for each mass load produced a full-width-half-maximum radiation pulse width within a factor of two or three of the experiments. This is good agreement considering that late time current behavior and axial motion such as zippering are not modeled. The mass calculated to be emitting in the K-shell as well as the outer radius of the K-shell emission at the time of stagnation are in excellent agreement with experiment. These results indicate, both experimentally and theoretically, that the K-shell emission of the lower mass loads are dominated by bulk plasma behavior, whereas, the inner core plasma does the K-shell radiating for the larger mass loads. Since  $\eta$  is less than unity for the more massive loads, they could not be bulk K-shell emitters.

The calculated peak K-shell powers agree within a factor of 1.5 with the experiments for the lower mass loads and within a factor of 5 for the higher mass loads. Again, this is good agreement considering that the calculated and experimental ion densities only agree to within factors of 2 - 3 and that optically thin radiative powers are very sensitive to the ion density, i.e. radiative power  $\propto N_i^2$ .

Since K-shell yields are dependent upon the amount of magnetic work done on the plasma, the comparison between calculated and experimental K-shell yields has large uncertainties at this stage because we do not have sufficient knowledge of the magnetic work that was done on the experimental plasmas. As soon as more information on the time resolved and integrated minimum outer radius of L-shell emission is made available to us, better determinations of this magnetic work can be made. Thus, for the moment, we find that the calculated K-shell yields for the more massive loads are in excellent agreement with experiment, whereas, the calculated yields for the lower mass loads are substantially smaller than the corresponding experimental yields. It is likely that late time current effects are responsible for this behavior. One reason for this likelihood is provided by the observation that the calculated kinetic energy after stagnation is  $\sim 70$

percent of the original magnetic work energy coupled to the plasma for the 42  $\mu\text{g/cm}$  plasma while it is only  $\sim 10$  percent for the 165  $\mu\text{g/cm}$  load. Thus, the lower mass loads undergo essentially an elastic stagnation in which very little of their kinetic energy is radiated away as it is thermalized in the current-off calculations. Conversely, most of this energy is radiated upon thermalization for the more massive loads even though only a small fraction of the total mass is needed to do the K-shell radiating. If the current continues to confine the plasma after stagnation in the experiments, then all of the pre-stagnation kinetic energy will be eventually radiated from the low mass loads. Since the value of  $\eta$  is  $> 1.0$  for these loads, the bulk of the plasma is hot enough that a significant portion of this radiation will come from the K-shell.

Another possible late time current effect that could be responsible for the experimental K-shell yields being larger than the calculated values for the low mass plasmas is ohmic or anomalous heating. If the plasma is confined on axis then it most likely will be in Bennett equilibrium and then

$$B^2/8\pi = N_i(1+Z)T_e/(\pi r^2) \quad (1)$$

where  $B$  is the magnetic field strength,  $r$  is the stagnation radius, and  $Z$  is the effective charge. Substituting  $B = 2I/rc$ , and  $N_i \approx m/(2Z \cdot 1.67 \times 10^{-24})$  in the above expression, we find

$$I^2 \approx 96 \times m \times T_e \quad (2)$$

where  $I$  is the current in MA,  $T_e$  is in eV, and  $m$  is the mass-per-unit-length (g/cm). In order to produce K-shell emission it is best to operate near the optimal electron temperature required to effectively radiate in the K-shell, i.e.  $T_{\text{opt}} \sim 0.3 Z^{2.9}$ .<sup>4</sup> Substituting  $T_{\text{opt}}$  into expression (2) gives

$$I^2 \sim 28 \times m \times Z^{2.9} \quad (3)$$

For Double Eagle, with a stagnation current of 3 MA, and  $Z = 18$  for argon, the optimal mass loading to achieve a K-shell Bennett equilibrium confinement is  $\sim 73 \mu\text{g/cm}$ , which lies between the 42 and 85  $\mu\text{g/cm}$  loads. The heating mechanism responsible for maintaining the equilibrium has not yet been determined and is under investigation.

The mass of each load was determined using a 0-D slug model and knowledge of the experimental implosion times  $\tau$ , which is the time to the onset of the K-shell emission. The fact that a 0-D model does not include plasma back pressure effects, which are especially important for those loads which start close to the axis, could explain the differences between the calculated  $\tau$  and experimental  $\tau$  for the most massive loads. If this is true, then 125  $\mu\text{g}/\text{cm}$  and 165  $\mu\text{g}/\text{cm}$  are larger than the actual respective load masses.

In the HEART work, viscosity, electron thermal conduction, and ion thermal conduction were enhanced until agreement with a 52  $\mu\text{g}/\text{cm}$  argon load was obtained; this occurred for multipliers of 20 - 40. Preliminary calculations that included electron thermal conduction also produced experimental agreement for the 42  $\mu\text{g}/\text{cm}$  and 85  $\mu\text{g}/\text{cm}$  loads. However, for the more massive loads, with enhanced electron thermal conduction even as large as a factor of 40, the stagnation ion densities of the K-shell emission region were still nearly two orders of magnitude larger than the experimental densities. This is the primary reason enhanced electron thermal conduction was not considered in this work.

#### SUMMARY AND CONCLUSIONS

In two earlier papers,<sup>3,4</sup> a series of 1-D MHD calculations were described that showed how the imploded mass and the kinetic energy generated per-ion influence the K-shell emission characteristics of a z-pinch. However, these calculations predicted an ideal implosion dynamics, which was not seen in the experiments. Based on the experimental evidence and on 2-D MHD z-pinch calculations,<sup>7</sup> it seems likely that some or all of the missing physics in the 1-D calculations is caused by plasma turbulence. In the HEART and BEAM's work this hypothesis was tested by employing a phenomenological approach of incorporating turbulence effects into the 1-D model. Multipliers were introduced for the plasma (artificial) viscosity, the ion and electron heat conductivity, and the electrical resistivity. It was then possible to make an appropriate choice for these multipliers so that the 1-D MHD calculations produced approximately the same plasma conditions as a 52  $\mu\text{g}/\text{cm}$  PI argon gas puff experiment. Again this provided supporting evidence for the presence of plasma turbulence in z-pinch experiments.

In this paper, a similar approach as outlined above was used in order to examine phenomenologically the scaling of turbulence effects with load mass. This was accomplished by comparing enhanced transport calculations with a

series of PI argon experiments in which the load mass was varied. The masses in these experiments ranged from 42 to 165  $\mu\text{g}/\text{cm}$ . Preliminary calculations had showed that agreement could not be attained with the experimental plasma conditions of the K-shell emission region when enhanced electron thermal conduction was included in the calculations for the larger mass loads. For this reason, enhanced electron thermal conduction was not included in this work, i.e. macroscopic turbulence effects were modeled only by enhanced viscosity (artificial), and ion thermal conduction.

We have found that it is possible to obtain reasonable agreement with experimental conditions during stagnation of the z-pinch over a range of mass loads by enhancing the viscosity and ion thermal conduction coefficients. A factor of  $> 10$  to 25 enhancement of the transport coefficients was required in order to get the 42  $\mu\text{g}/\text{cm}$  load to approximate the experimental conditions while it took twice this factor for the largest (165  $\mu\text{g}/\text{cm}$ ) load. It is expected that the amount of enhancement required to approximate the experimental conditions will saturate with increased mass, because eventually, a flux limit for physically allowable transport will be reached. This hypothesis will be tested by including ion thermal flux correctors in the calculations and comparing the results with larger mass experiments, e.g. Saturn argon experiments.

Both calculations and experiments support the idea that the bulk of the plasma emits in the K-shell when  $\eta > 1$  and that it is only the plasma core which radiates in the K-shell when  $\eta < 1$ . Previous current-off calculations which included enhanced electron thermal conduction did not show proportionately as much K-shell emission from the core of  $\eta < 1$  plasmas, most likely because the energy of the core is transferred too rapidly to the bulk of the plasma.

The stagnation of the 42  $\mu\text{g}/\text{cm}$  load was very elastic, i.e. only 30 percent of the pre-stagnation kinetic energy was radiated away in these current-off calculations. Given that the current is still present during stagnation in the experiment, most of the remaining energy (70 percent) would be confined and radiated. This is a possible explanation for why the K-shell yield from the lower mass plasmas was higher in the experiments than predicted by the current-off calculations. We showed that ohmic heating or anomalous heating during Bennett confinement can "cook" the lower mass plasmas while they exist in the K-shell ionization stages.

In the future we hope to investigate the scaling of turbulence coefficients to even larger masses than examined here and also to different Z elements. If a phenomenological determination of the scaling of turbulence

coefficients with Z and mass can be made, then this knowledge will be used to reexamine the BEAM's work in order to obtain a more accurate determination of the mass boundaries for scaling of K-shell emission efficiently with Z, mass loading, and kinetic energy (machine energy). As illustrated in this study, effects such as plasma confinement and heating during stagnation may play a significant role in influencing the K-shell yield. By continuing our strong collaboration with the experimentalists the plasma conditions under which these effects are important can be determined by comparing the experimental results with calculations in which the full current or a short-circuit current are present during stagnation. All of this work has substantial implications for the performance, design, and optimization of DECADE PRS loads.

#### REFERENCES

1. J. W. Thornhill, K. G. Whitney, C. Deeney, M. C. Coulter, and D. LePell, "PRS Simulator Design Requirements for Hundreds of Kilojoule X-Ray Output for NWET in DECADE," presented at 1992 HEART Conference and accepted for publication in JRE.
2. K. G. Whitney, J. W. Thornhill, C. Deeney, P. D. Lepell, and M. C. Coulter, "Phenomenological Modeling of Argon Z-Pinch Implosions," to be published in BEAM's 1992 conference proceedings.
3. J. W. Thornhill, K. G. Whitney, and J. Davis, J. Quant. Spectrosc. Radiat. Transfer 44, 251 (1990).
4. K. G. Whitney, J. W. Thornhill, J. P. Apruzese, and J. Davis, J. Appl. Phys. 67, 1725 (1990).
5. C. Deeney, T. Nash, R. R. Prasad, L. Warren, K. G. Whitney, J. W. Thornhill, and M. C. Coulter, Phys. Rev. A 44, (1991).
6. M. C. Coulter, K. G. Whitney, and J. W. Thornhill, J. Quant. Spectrosc. Radiat. Transfer 44, 443 (1990).
7. C. Deeney, P. D. Lepell, F. L. Cochran, and M. C. Coulter, "Argon Gas Puff Implosion Experiments and Two Dimensional Modeling," submitted to Phys. of Fluids for publication.

Argon mass is 42 $\mu\text{g/cm}$ Initial Radius is 2.0 cm	Experimental Results	$K_i$ and $v \times 1$ Results	$K_i$ and $v \times 10$ Results	$K_i$ and $v \times 18$ Results	$K_i$ and $v \times 25$ Results
K-shell radiation pulse width $\tau_{FWHM}$ (ns)	9.0	$\sim 1$	$\sim 1$	$\sim 3$	$\sim 4$
$\langle Ni \rangle$ of K-shell emission region ( $10^{19} \text{ cm}^{-3}$ )	1.5	$\tau^+ 1.7$ $\tau 4.5$ $\tau^- 4.1$	1.7 3.0 3.0	0.5 1.0 0.7	0.4 0.7 0.4
$\langle Te \rangle$ of K-shell emission region (keV)	1.7	$\tau^+ 1.7$ $\tau 3.0$ $\tau^- 2.5$	2.1 3.0 2.9	1.8 3.0 2.0	1.8 2.7 1.8
Mass emitting in the K-shell ( $\mu\text{g/cm}$ )	30.	32	32.	29.	29.
Outer Radius of K-shell emission region (cm) at $\tau$	0.1	0.06	0.07	0.12	0.13
Minimum outer radius of L-shell emission region (cm)	time - 0.4 integrated time - 0.2 resolved	0.18	0.20	0.17	0.19
K-shell emission peak power (GW/cm)	271	1200	900	280	200
K-shell yield (kJ/cm)	3.46	1.9	1.7	.88	.73
Magnetic work done on plasma (kJ/cm)	15.8 - 22.	13.	13.	13.5	13.8
Ohmically Coupled Energy (kJ/cm)	Not Available	0.5	0.5	0.5	0.5
$\eta^*$	3.9 - 5.4	3.2	3.2	3.3	3.4
Implosion time $\tau$ in (ns)	115	117	117	118	118
Current at $\tau$ (MA)	3.3	3.2	3.2	3.2	3.2
Kinetic energy after stagnation $t = \infty$ (kJ/cm)	Not Available	9.0	9.1	10.0	10.0

Table 1. Experimental and calculated parameters for the 42  $\mu\text{g/cm}$  argon gas puff load.  $\tau_{FWHM}$  is the time duration of the full-width-half-maximum of the K-shell radiation pulse.  $\tau^+$  and  $\tau^-$  are the respective times of the right and left hand edges of  $\tau_{FWHM}$ .  $\eta^*$  is the magnetic work done on the plasma divided by the product of the ion density and the minimum energy required to reach the K-shell ( $E_{min} \sim 40 \text{ keV/ion}$ ).

Argon mass is 85 $\mu\text{g}/\text{cm}$ Initial radius is 1.25 cm	Experimental Results	$K_i$ and $v \times 1$ Results	$K_i$ and $v \times 25$ Results	$K_i$ and $v \times 40$ Results
K-shell radiation pulse width $\tau_{FWHM}$ (ns)	13.	$\sim 1$	$\sim 4$	$\sim 4$
$\langle Ni \rangle$ of K-shell emission region ( $10^{19} \text{ cm}^{-3}$ )	2.0	$\tau^+$ 30. $\tau$ 70. $\tau^-$ 60.	2.9 3.5 2.3	1.4 1.9 1.4
$\langle Te \rangle$ of K-shell emission region (keV)	1.7	$\tau^+$ 1.0 $\tau$ 1.0 $\tau^-$ 0.8	1.4 2.0 1.4	1.7 2.1 1.6
Mass emitting in the K-shell ( $\mu\text{g}/\text{cm}$ )	40.	55.	39.	39.
Outer Radius of K-shell emission region (cm) at $\tau$	0.1	0.02	0.07	.1
Minimum outer radius of L-shell emission region (cm)	time - 0.34 integrated time - NA resolved	0.14	0.18	.18
K-shell emission peak power (GW/cm)	354	4000	700	460
K-shell yield (kJ/cm)	4.16	4.0	2.3	2.2
Magnetic work done on plasma (kJ/cm)	- 10.7	11.1	11.5	11.8
Ohmically Coupled Energy (kJ/cm) (kJ/cm)	Not Available	0.8	0.8	0.8
$\eta^*$	1.31 -	1.36	1.41	1.45
Implosion time $\tau$ in (ns)	110	110	111	111
Current at $\tau$ (MA)	3.0	2.9	2.9	3.0
Kinetic energy after stagnation $t = \infty$ (kJ/cm)	Not Available	1.1	4.3	5.0

Table 2. Experimental and calculated parameters for the 85  $\mu\text{g}/\text{cm}$  argon gas puff load.  $\tau_{FWHM}$  is the time duration of the full-width-half-maximum of the K-shell radiation pulse.  $\tau^+$  and  $\tau^-$  are the respective times of the right and left hand edges of  $\tau_{FWHM}$ .  $\eta^*$  is the magnetic work done on the plasma divided by the product of the ion density and the minimum energy required to reach the K-shell ( $E_{min} \sim 40 \text{ keV/ion}$ ).



Argon mass is 125 $\mu\text{g}/\text{cm}$ Initial radius is 1.0 cm	Experimental Results	$K_\alpha$ and $\nu \times 1$ Results	$K_\alpha$ and $\nu \times 25$ Results	$K_\alpha$ and $\nu \times 40$ Results
K-shell radiation pulse width $\tau_{\text{FWHM}}$ (ns)	Not Available	< 1	$\sim 3$	$\sim 4$
<Ni> of K-shell emission region ( $10^{19} \text{ cm}^{-3}$ )	Not Available	$\tau^+$ 14. $\tau$ 30. $\tau^-$ 100.	2.0 6.0 5.0	1.2 4.0 3.6
<Te> of K-shell emission region (keV)	1.6	$\tau^+$ 2.0 $\tau$ 2.0 $\tau^-$ 1.3	2.0 2.3 1.4	2.0 2.0 1.4
Mass emitting in the K-shell ( $\mu\text{g}/\text{cm}$ )	Not Available	9.	24.	29.
Outer Radius of K-shell emission region (cm) at $\tau$	not available	0.02	0.04	0.07
Minimum outer radius of L-shell emission region (cm)	time - NA integrated time - NA resolved	0.13	0.14	0.14
K-shell emission peak power (GW/cm)	194	2000	800	600
K-shell yield (kJ/cm)	2.6	1.4	2.8	2.33
Magnetic work done on plasma (kJ/cm)	Not Available	10.5	10.8	11.2
Ohmically Coupled Energy (kJ/cm)	Not Available	1.1	1.1	1.0
$\eta^*$	Not Available	0.88	0.91	0.93
Implosion time $\tau$ in (ns)	100	107	108	108
Current at $\tau$ (MA)	3.2	2.8	2.8	2.8
Kinetic energy after stagnation $t = \infty$ (kJ/cm)	Not Available	0.6	1.7	2.3

Table 3. Experimental and calculated parameters for the 125  $\mu\text{g}/\text{cm}$  argon gas puff load.  $\tau_{\text{FWHM}}$  is the time duration of the full-width-half-maximum of the K-shell radiation pulse.  $\tau^+$  and  $\tau^-$  are the respective times of the right and left hand edges of  $\tau_{\text{FWHM}}$ .  $\eta^*$  is the magnetic work done on the plasma divided by the product of the ion density and the minimum energy required to reach the K-shell ( $E_{\text{min}} \sim 40 \text{ keV/ion}$ ).

Argon mass is 165 $\mu\text{g/cm}$ Initial radius is 0.75 cm	Experimental Results	$K_i$ and $v_i \times 1$ Results	$K_i$ and $v_i \times 25$ Results	$K_i$ and $v_i \times 40$ Results	$K_i$ and $v_i \times 50$ Results
K-shell radiation pulse width $\tau_{FWHM}$ (ns)	Not Available	< 1	$\sim 2$	$\sim 3$	$\sim 4$
<Ni> of K-shell emission region ( $10^{19} \text{ cm}^{-3}$ )	2.	$\tau^+$ 10. $\tau$ 50. $\tau^-$ 200.	6. 12. 20.	3. 6. 7.	2. 5. 5.
<Te> of K-shell emission region (keV)	1.6	$\tau^+$ 1.0 $\tau$ 1.2 $\tau^-$ 0.9	1.8 2.0 1.2	1.8 1.8 1.3	1.9 2.0 1.3
Mass emitting in the K-shell ( $\mu\text{g/cm}$ )	10.	5.	18.	18.	18.
Outer Radius of K-shell emission region (cm) at $\tau$	0.05	.007	0.02	0.03	0.04
Minimum outer radius of L-shell emission region (cm)	time - NA integrated time - NA resolved	0.12	0.13	0.12	0.13
K-shell emission peak power (GW/cm)	140	500	850	700	630
K-shell yield (kJ/cm)	1.7	0.33	2.2	2.3	2.3
Magnetic work done on plasma (kJ/cm)	Not Available	8.7	8.8	9.1	9.2
Ohmically Coupled Energy (kJ/cm)	Not Available	1.2	1.3	1.2	1.2
$\eta^*$	Not Available	0.55	0.55	0.57	0.58
Implosion time $\tau$ in (ns)	95	100	100	100	100
Current at $\tau$ (MA)	2.9	2.7	2.7	2.7	2.6
Kinetic energy after stagnation $t = \infty$ (kJ/cm)	Not Available	0.7	0.6	0.8	1.0

Table 4. Experimental and calculated parameters for the 165  $\mu\text{g/cm}$  argon gas puff load.  $\tau_{FWHM}$  is the time duration of the full-width-half-maximum of the K-shell radiation pulse.  $\tau^+$  and  $\tau^-$  are the respective times of the right and left hand edges of  $\tau_{FWHM}$ .  $\eta^*$  is the magnetic work done on the plasma divided by the product of the ion density and the minimum energy required to reach the K-shell ( $E_{\min} \sim 40 \text{ keV/ion}$ ).

### III. NON-MAXWELLIAN DISTRIBUTION FUNCTIONS IN DECADE-CLASS Z-PINCHES

#### Introduction

Non-Maxwellian electron distribution functions could become a critical factor determining how an optimal PRS implosion will perform at DECADE current levels and beyond. As the mobile component of the plasma, electrons provide most of the thermal pressure and carry most of the current. Varying the largely electronic thermal and electrical conductivity will change a "hard" implosion into a "soft" implosion, or vice-versa. Ohmic plasma heating is mediated by the electrons, which absorb electrical energy from the generator and transfer it to ions by both elastic and inelastic collisions. The atomic line radiation consequent from inelastic electron-ion collisions is an important plasma diagnostic, and could play a crucial role in the energy balance that determines whether there is radiative collapse. Also of concern, observations of beams of runaway electrons under certain pinch conditions show that there is sometimes energy transfer that does not result in plasma heating; these runaway electrons may also be associated with hot spots, poorly understood regions of enhanced radiation and probable hydrodynamic instability. For all these reasons, a good understanding of the factors influencing the electron distribution function is an important part of understanding present PRS experiments and of designing future more powerful PRS devices.

In DECADE, the peak current will be many times that of earlier machines. This increased current means increased electron flow velocities and greater electric-field heating of the electrons, which means more favorable conditions for ion-acoustic microturbulence. The higher plasma temperatures in DECADE could mean increased importance for electron-ion excitation collisions, a factor that in lower power machines made a difference of only a few percent. (The importance of these inelastic collisions is proportional to temperature for fixed ion populations, although the population levels also depend on temperature). Higher inductive current flows in DECADE also mean larger electric fields, both parallel to and transverse to the current, which could change the way ohmic heating affects the distribution function from lower-power machines.

Generally, it is assumed that the electron distribution has a Maxwellian shape, because electron-electron collisions, which are always present, cause the distribution to relax towards a Maxwellian equilibrium. PRS timescales are nanoseconds to hundreds of nanoseconds. Electron-electron collisions equilibrate the system on the collisional timescale:

$$\tau_{ee} = 0.2588 \frac{(\kappa T)^{3/2}}{n_{18} \log \Lambda} \text{ ps}, \quad (1)$$

where  $\kappa T$  is the temperature in eV,  $n_{18}$  is the density in units of  $10^{18} \text{ cm}^{-3}$ , and  $\log \Lambda = \log [5.1596(\kappa T)^{3/2}/n_{18}^{1/2}]$  is the Coulomb logarithm. At low energies, below the thermal

energy, electron-electron collisions are increasingly dominant, but equilibration is slower for the high-energy electrons in the tail of the distribution. In the distribution tail, the effects of ohmic heating and collisional cooling to produce non-Maxwellian distributions are quite pronounced, especially at high temperatures, and are strongly influenced by the strength of the magnetic field. In addition, the effects of these processes can be magnified by plasma microturbulence, which if present can also greatly increase the resistivity and viscosity.

In this report, we lay out a general analysis of how the electron distribution function develops in a PRS implosion. These results form a comprehensive basis for finding plasma conditions (and implosion parameters) that create non-Maxwellian distributions. In the first section, we describe the plasma conditions and the methods of study. The second section sketches the relevant kinetic theory, which includes electron-electron collisions, a model of ohmic heating, and inelastic collisions with ions.<sup>1</sup> We then discuss ion-acoustic turbulence, whose properties and likely presence in implosions have been presented earlier.<sup>2</sup> We show how ion-acoustic turbulence can be simply included in our model, and introduce a parameter to estimate its strength.

The consequences of this kinetic theory are explored in section 4. The actual shape of the distribution function depends on the interplay between the Maxwellian-producing electron-electron collisions and the various other processes, whose effects depend primarily on temperature, current density and magnetic field strength. Ohmic heating in a strong magnetic field produces depleted-tail distributions of a well-established form,<sup>3</sup> but for moderate magnetic field strengths or in the presence of ion-acoustic turbulence more complicated distribution function shapes are produced. Inelastic electron-ion collisions, surprisingly, tend to produce relatively enhanced distribution function tails. We estimate the relative importance of these processes, depending on plasma conditions and on the strength of turbulence.

To obtain practical results from the model, we need a way to determine the local electric field in the plasma. In fact, all that is generally available is an estimate of the total current through the pinch, from which we can estimate the local current density, based on assumptions about the radial current profile. The current density is directly related to the current-aligned component of the electric field by the transverse Spitzer resistivity.<sup>4</sup> In addition to this, a large radial component of the electric field is needed to drive the current across the pinching magnetic field. It is the total electric field, not just the current-aligned component, that is used in our model. Therefore, we show in section 5 how to calculate the resistivity in terms of the actual distribution functions; this allows us to find the electric field in terms of the current density. Simplified analytic expressions for the conductivity are introduced in this section, which are useful for showing the basic scaling properties of the resistivity. Numerical calculations of the resistivity of self-similar distributions<sup>3</sup> are also presented, showing non-Maxwellian effects for various magnetic fields. The increase of resistivity with turbulence is shown.

Runaway phenomena are briefly discussed in section 6. In contrast to tokamacs, where current is mostly along magnetic field lines and runaways are commonly observed, PRS devices have transverse current and magnetic field, and freely-accelerated runaways tend to be suppressed. Runaways are possible where the electric field exceeds the magnetic field strength; where and how this situation exists depends sensitively on how current penetrates into the conducting plasma, a subject that will be studied in detail in the near future. Here, we discuss conditions for runaway generation and show how runaways would be manifested in our model. In particular, the increasing anisotropy of the electron distribution with increasing current is pointed out.

Finally, we illustrate the model developed here by calculating in section 7 the time-evolution of the electron distribution function in a selenium z-pinch at different temperatures and magnetic field strengths. An energy equilibrium is assumed, where ohmic heating is balanced by inelastic collisions and radiative dissipation. The K- and L-shell inelastic collision strengths for selenium were derived from radiative rates determined by the Radiation Hydrodynamics Branch,<sup>5</sup> which are also used in Branch MHD calculations. Ion populations were determined by collisional-radiative equilibrium (CRE) calculations for the temperature and density.

These results represent only the initial step in applying the kinetic model developed here to study PRS electron distributions. The model includes the important influences on the distribution, even nonlinear turbulence phenomena. When this is coupled with the comprehensive atomic database of the Radiation Hydrodynamics Branch, as we have done, model predictions can be used to study the effect of non-Maxwellian distributions on energy balance within the device. The transport coefficients (e.g., resistivity) from the model can be used to improve MHD modeling. The next step will be to determine for what parameters non-Maxwellian corrections are significant; for this, a self-consistent scheme for determining the current and field distribution must be developed. Plans for this step are discussed in the conclusion.

## 1. Theory

We are looking at the evolution of the electron distribution function in a high atomic number plasma in an imploding z-pinch. The ions are much heavier than the electrons, and reach equilibrium much faster, and so we assume the ion distribution to be a Maxwellian. Electron-electron collisions are very important in energy exchange and in determining the isotropic part of the distribution, but are not so important in exchange of momentum; therefore we ignore the direct contribution of electron-electron collisions to the current (that is, we assume a Lorentzian plasma). Electron-ion collisions are the dominant factor determining the current; these are much more frequent than electron-electron collisions, so that the directional part of the electron distribution is in quasi-equilibrium. Inelastic collisions affect only the isotropic part of the distribution; they are

not frequent enough to contribute on the electron-ion timescale.

The system is composed of electrons and various ion species  $\alpha$ , each with charge  $Z_\alpha e$ , mass  $m_\alpha$  and density  $n_\alpha$ . The mean ion charge number is  $Z = n_e/n_i$ , where  $n_e = \sum_\alpha n_\alpha Z_\alpha$  and  $n_i = \sum_\alpha n_\alpha$ ; we assume  $Z \gg 1$ . The plasma frequency for species  $\alpha$  is  $\omega_\alpha = \sqrt{4\pi Z_\alpha^2 e^2 n_\alpha / m_\alpha}$ . The electric field  $\vec{E}$  and magnetic field  $\vec{B}$  are constant and uniform; the electrostatic force on electrons is  $m\vec{a} = e\vec{E}$ , and the vector cyclotron frequency is  $\vec{\omega}_c = (e/mc)\vec{B}$ . Spatial variation of all quantities is neglected in the model.

The ions, with mass  $m_\alpha$  much greater than the electron mass  $m$ , are assumed to maintain a Maxwell-Boltzmann distribution  $f_\alpha(v)$ . The electrons are described by a distribution function  $f(\vec{v}, t)$ , normalized to  $n_e$ . Here, a Cartesian tensor expansion is used<sup>6</sup> with only the first-order term retained, so that

$$f(\vec{v}, t) \approx f_0(v) + \vec{v} \cdot \vec{f}_1(v). \quad (2)$$

Thus, for example, the average energy  $\langle E \rangle$  is determined by  $f_0(v)$ :

$$\langle E \rangle = \frac{4\pi}{n_e} \int_0^\infty \frac{1}{2} m v^2 f_0(v) v^2 dv \quad (3)$$

and the current density  $\vec{j}$  is determined by  $\vec{f}_1(v)$ :

$$\vec{j} = \frac{4\pi}{3n_e} \int_0^\infty (e n_e v) \vec{f}_1(v) v^2 dv. \quad (4)$$

In general, the Cartesian-tensor expansion has an infinite number of terms, with term  $f_n(v)$  being an  $n^{\text{th}}$  order tensor. The magnitude of  $\vec{f}_1(v)$  determines the directionality of the distribution: The distribution is isotropic (though not necessarily Maxwellian) if  $f_1(v) \sim 0$ , and the greatest possible anisotropy is if  $f_1(v) = f_0(v)$ . Except in special circumstances, neglect of the higher-order terms implies that  $f_1(v) \ll f_0(v)$ .

The "temperature" of the nonequilibrium system is defined to be proportional to the average energy (in units of eV, when in numerical formulas):

$$\kappa T \equiv \frac{2}{3} \langle E \rangle, \quad (5)$$

and the thermal velocity is defined as:

$$v_{th} = \sqrt{\frac{2\kappa T}{m}}. \quad (6)$$

The (Rutherford) collision frequency of a particle of species  $\alpha$  as it moves with velocity  $v_\alpha$  through a number density  $n_\beta$  of species  $\beta$  particles is:

$$\nu_{\alpha\beta} = Y_{\alpha\beta} \frac{n_\beta}{v_\alpha^3} \quad (7)$$

where

$$Y_{\alpha\beta} = \frac{4\pi Z_\alpha^2 Z_\beta^2 e^4}{m_\alpha^2} \log \Lambda_{\alpha\beta}. \quad (8)$$

and  $\log \Lambda$  is the Coulomb logarithm.<sup>7</sup> The characteristic frequency in this system is  $\nu_R \equiv \nu_{ee}(v_{th})$ .

The inelastic collisions considered here transfer energy from the electrons to the ions, exciting the ion to a higher energy level. De-excitation collisions, which transfer energy from ions to electrons, are neglected. The transition energy from level  $a$  to level  $b$  is  $\epsilon_{ab}$ ; below this electron energy there is no energy transfer. The actual inelastic collision frequencies are complicated functions of atomic parameters, but they can be conveniently expressed in terms of slowly-varying semi-empirical collision strengths, of order one. The collision frequency for an electron of velocity  $v$  to excite an ion from level  $a$  to level  $b$  is

$$\nu_{ab}^* = n_a \left[ \pi a_0^2 \frac{\Omega_{ab}(\epsilon)/g_a}{\epsilon/Ry} \theta(\epsilon - \epsilon_{ab}) \right] v, \quad (9)$$

where  $\epsilon = \frac{1}{2}mv^2$ ,  $Ry \approx 13.6$  eV is the Rydberg energy,  $a_0$  is the Bohr radius,  $g_a$  is the multiplicity of level  $a$ , and  $\Omega_{ab}(\epsilon)$  is the collision strength mentioned above.

## 2. Basic description: without turbulence

The electron distribution function evolves according to the Boltzmann equation:

$$\frac{\partial f}{\partial t} + (\vec{a} + \vec{v} \times \vec{\omega}_c) \cdot \vec{\nabla}_v f = C_{el} + C_{inel} \quad (10)$$

with small-angle collisions  $C_{el}$  described by a Landau collision term,<sup>8</sup> and inelastic collisions  $C_{inel}$  included as discussed below. Using the first-order Cartesian-tensor expansion, assuming the ions to be in a spherically-symmetric Maxwellian distribution and neglecting the effect of electron-electron collisions on  $\vec{f}_1(v)$  (i.e., assuming a Lorentzian plasma), we obtain two coupled kinetic equations:

$$\frac{df_0}{dt} = C_{EB} + C_{FP} + C^* \quad (11)$$

$$\frac{d\vec{f}_1}{dt} + \vec{a} \frac{\partial f_0}{\partial v} + \vec{\omega}_c \times \vec{f}_1 = -\nu_{ei}(v) \vec{f}_1. \quad (12)$$

The isotropic distribution  $f_0(v)$  is determined by the electric-field heating term  $C_{EB}$ , a Fokker-Planck elastic collision term  $C_{FP}$  and an inelastic collision term  $C^*$ . The electric-field heating term is:

$$C_{EB} = -\frac{1}{3v^2} \frac{\partial}{\partial v} \left[ v^2 \vec{a} \cdot \vec{f}_1 \right]. \quad (13)$$

This is evidently proportional to  $\vec{j} \cdot \vec{E}$  (cf. eq. (4)). The elastic collision term describes the effects of multiple small-angle electron-electron collisions:

$$C_{FP} = \frac{4\pi Y_{ee}}{v^2} \frac{\partial}{\partial v} \left[ f_0 \int_0^v f_0(v') v'^2 dv' + \frac{v}{3} \frac{\partial f_0}{\partial v} \left( \frac{1}{v^2} \int_0^v f_0(v') v'^4 dv' + v \int_v^\infty f_0(v') v' dv' \right) \right]. \quad (14)$$

The inelastic term is of the form

$$C^* = \sum_j [-\nu_j^*(\epsilon) f_0(\epsilon) + \sqrt{\frac{\epsilon + \epsilon_j}{\epsilon}} \nu_j^*(\epsilon + \epsilon_j) f_0(\epsilon + \epsilon_j)] \quad (15)$$

where  $\nu_j^*(\epsilon)$  is the energy-dependent collision frequency (given in eq. (9)) and  $\epsilon_j$  is the threshold energy, for the  $j^{\text{th}}$  inelastic collision process. This term conserves the number of ions and free electrons, as it should, without ionization or recombination: An inelastic collision simply transfers electrons within the distribution from energy  $\epsilon$  to energy  $\epsilon - \epsilon_j$ . The factor  $\sqrt{(\epsilon + \epsilon_j)/\epsilon}$  makes allowance for the greater phase-space volume available at energy  $\epsilon + \epsilon_j$ : the number of particles scattered between energy  $\epsilon$  and  $\epsilon + \epsilon_j$  is always  $\nu^*(\epsilon) f(\epsilon) 4\pi\sqrt{\epsilon} d\epsilon$ . The contribution of inelastic collisions to the  $\vec{f}_1$  equation is neglected because  $\nu^* \ll \nu_{ei}$  ( $\nu_j^*/\nu_{ei} \propto Z^{-2}$ ), and so inelastic-collision changes to  $\vec{f}_1$  are relatively slow.

The inelastic collision term  $C^*$  is related to the excitation rates commonly used in MHD codes. The excitation rate  $W_{ab}$  from state  $a$  to state  $b$  is defined such that  $\partial n_b / \partial t = \sum_a n_a W_{ab}$ ; it is the inelastic collision frequency  $\nu_{ab}^*$  times the number of electrons available in state  $a$  to excite the transition. Thus, the rate depends on the electron distribution function assumed for its computation (usually a Maxwellian):

$$W_{ab} = \frac{4\pi}{n_a} \int_0^\infty \nu_{ab}^*(v) f_0(v) v^2 dv. \quad (16)$$

All information about the collision is found in the collision strength  $\Omega_{ab}(\epsilon)$ . Although the rates are computed as shown from the collision strengths, it is not feasible to deduce collision strengths from rates.\* We have, however, successfully reconstructed collision strengths from rates by fitting to the assumed functional form  $\Omega_{ab} = \Omega_0 e^{a\epsilon}$ . This self-consistent procedure entails only a small error in computing radiative output (determined by recalculating rates from the deduced collision strengths), and will give good estimates of  $C^*$  for most collision strengths.

As a step towards solving the coupled eqs. (11–12), we now find an approximate solution to eq. (12), thus determining  $C_{EB}$  and leaving only one equation to solve. We note that  $\vec{f}_1$  equilibrates at the high frequency of  $\nu_{ei} = Z\nu_{ee}$ , and so assume it to be in quasi-static equilibrium with  $f_0$ . The equilibrium solution to eq. (12) is in general

$$\vec{f}_1 = \frac{1}{\omega_c^2 + \nu_{ei}^2} \left[ \vec{\omega}_c \times \vec{a} - \frac{\vec{\omega}_c \cdot \vec{a}}{\nu_{ei}} \vec{\omega}_c - \nu_{ei} \vec{a} \right] \frac{\partial f_0}{\partial v}. \quad (17)$$

Note that when  $\vec{a} \parallel \vec{\omega}_c$ , this is independent of  $\omega_c$ , as it should be. Here, we consider the

---

\* It is in principle possible to invert the numerical integration sums, which form a product of a Vandermonde matrix with a vector of collision strength values on a grid. In practice, however, the matrix is much too ill-conditioned.



complementary situation,  $\vec{a} \perp \vec{\omega}_e$ , where

$$C_{EB} = \frac{1}{3v^2} \frac{\partial}{\partial v} \left[ v^2 \frac{a^2}{\nu_{ei} (1 + \omega_e^2 / \nu_{ei}^2)} \frac{\partial f_0}{\partial v} \right]. \quad (18)$$

In summary, the kinetic equation without turbulence is just eq. (11), with eq. (18) for  $C_{EB}$ , eq. (14) for  $C_{FP}$  and eq. (15) for  $C^*$ .

### 3. Inclusion of turbulence

The non-turbulent plasma is well defined in terms of slowly-varying average quantities like the density. Although there are always microscopic fluctuations from the average values, these are small in magnitude. But in turbulent plasmas, the fluctuations are not small, and can greatly affect plasma dynamics. Turbulent fluctuations generally involve collective modes of the plasma and are generated by a plasma instability; at a minimum, the turbulent mode cannot be strongly damped. We have conducted a survey<sup>2</sup> of important instabilities for typical z-pinch parameters and found that the most likely important sources of turbulence are the ion-acoustic and lower-hybrid drift instabilities. Here we look exclusively at the ion-acoustic instability, which we found to be favored at certain times in a variety of high-Z z-pinch. Although the lower-hybrid drift instability might be important, it may not have sufficient time to become established in these short implosions.

The ion-acoustic dispersion relation (real part) is

$$\omega(k) = \frac{kc_s}{\sqrt{1 + k^2 \lambda_D^2}}, \quad (19)$$

where  $c_s \equiv \sqrt{Z\kappa T_e / m_i}$  is the ion-sound velocity and  $\lambda_D \equiv \sqrt{\kappa T_e / 4\pi n_e e^2}$  is the electron Debye length. The growth or damping rate is given by the imaginary part of  $\omega$ , and for a mode to be important its growth time  $\tau \equiv \Im m(\omega)^{-1}$  must be positive, and significantly shorter than the implosion timescale. In a stationary plasma and when electron and ion temperatures are equal, the ion-acoustic mode is Landau-damped. Instability occurs only when

$$\begin{cases} ZT_e / T_i > 1 \\ u_0 > c_s \end{cases} \quad (20)$$

where the electron fluid velocity is

$$u_0 \equiv j / en_e. \quad (21)$$

Thus, for ion-acoustic turbulence to be significant in an implosion, there must be both a significant electron-ion thermal disequilibrium and a large flow velocity (high current or low density). Electron-ion equilibrium depends on details of the plasma heating: Electric-field heating gives energy primarily to the electrons, which then collisionally transfer this energy to ions. The

equilibration timescale is  $\nu_{ei}^{-1}$ , which we have already argued is very short. When there is strong heating, however, such as early in runin and at stagnation, the electron temperature can exceed ion temperature. Even a small such disequilibrium can trigger instability if the ions are strongly ionized ( $Z \gg 1$ ). As the electrons heat up relative to the ions, they interact with the current flow to trigger the instability. Without ion damping (an extreme limit), the maximum growth rate is such that  $\omega_i \tau_{maz} \approx 3.19 v_{th}/u_0$ , or

$$\tau_{maz} \approx 2.30 \times 10^{-5} \frac{\sqrt{\mu_i n \kappa T / Z}}{j} \text{ ns}, \quad (22)$$

where  $\mu_i \equiv m_i/m_{\text{proton}}$  is the mass number of the ions. This could easily translate to a growth timescale of nanoseconds, the characteristic implosion time.

After triggering, the instability develops nonlinearly, and will persist even at saturation, when the conditions drop below triggering levels and the growth rate is zero. Energy from the current flow continues to go into fluctuations, as reflected in the anomalously high resistivity and heating levels observed.<sup>9,10</sup>

We now show how to use quasilinear theory to incorporate turbulence into our kinetic model. We will derive a parameter for the turbulence strength and use it to estimate the impact of fully-developed ion-acoustic microturbulence. In quasilinear theory, the distribution function is written as the sum of a slowly-varying average  $\langle f(v) \rangle$  (identical to  $f(\vec{v}, t)$  of eq. (2)) and a rapidly-varying fluctuation  $\delta f(v, t)$  (introduced here). Other quantities (e.g., fields) are similarly analyzed. If this expansion is used in eq. (10), the average and fluctuating distribution satisfy the "linearized" equations:<sup>2</sup>

$$\left[ \frac{\partial}{\partial t} + \langle \vec{a} + \vec{v} \times \vec{\omega}_c \rangle \cdot \vec{\nabla}_v \right] f(v, t) = -\langle \delta \vec{a} \cdot \vec{\nabla}_v \delta f \rangle \quad (23)$$

$$\left[ \frac{\partial}{\partial t} + \langle \vec{a} + \vec{v} \times \vec{\omega}_c \rangle \cdot \vec{\nabla}_v \right] \delta f(v, t) = -\delta \vec{a} \cdot \vec{\nabla}_v f(v) \quad (24)$$

Eq. (23) is just the Boltzmann equation, eq. (10), omitting the collision terms but adding a "quasilinear" source term on the right-hand side. The difference of two similar second-order terms has been neglected in eq. (24), on the argument that their influence on the average distribution is effectively third order. The RHS of eq. (23) provides a collision-like turbulence term for eq. (10). Evaluating it requires solving for both the fluctuating distribution and the consequent fluctuating fields from eq. (24) and Maxwell's equations. Making the fluctuating densities and fluctuating fields self-consistent results in a dispersion equation, and the undamped solutions of the dispersion equation define the turbulent modes.

Eq. (24) is in the form of the linearized Vlasov equation and can be solved in the same way. Fortunately, the magnetic field can be ignored in the solution, as long as it doesn't

significantly affect the predicted dispersion relation. Therefore, we can consistently study plasma microturbulence from electrostatic waves while retaining the dynamical effects of the magnetic field in eq. (10). Thus, Fourier transforming to solve eq. (24) and using Poisson's equation to obtain the fluctuating fields from the fluctuating densities, the new, quasilinear term has a diffusive form:

$$-(\delta \tilde{a} \cdot \vec{\nabla}_v \delta f) = \vec{\nabla}_v \cdot [\mathcal{D} \cdot \vec{\nabla}_v f] \quad (25)$$

where the diffusion tensor is

$$\mathcal{D}_{ij} = \frac{8\pi^2 e^2}{m^2} \int d^3 k \frac{k_i k_j}{k^2} W(k) \delta(\omega(k) - \vec{k} \cdot \vec{v}) \quad (26)$$

and  $W(k)$  is the electrostatic wave energy density, defined such that  $\int d^3 k W(k) = \langle \delta E^2 \rangle / 4\pi$ .

The specific form of the quasilinear diffusion tensor  $\mathcal{D}$  depends on the turbulent mode  $\omega(k)$  and energy density  $W(k)$ . If we use the real part of the ion-acoustic dispersion relation, eq. (19), to solve for  $\mathcal{D}$ , and then perform a Cartesian-tensor expansion, we obtain quasilinear terms in both the scalar and vector equations (eq. (11) and eq. (12)):

$$\vec{\nabla}_v \cdot [\mathcal{D} \cdot \vec{\nabla}_v f]^{(0)} = \frac{4\pi^2 e^2 \Omega}{m^2} \frac{c_s^2}{v^2} \frac{\partial}{\partial v} \left( \frac{1}{v} \frac{\partial f_0}{\partial v} \right) \quad (v > c_s) \quad (27)$$

$$\vec{\nabla}_v \cdot [\mathcal{D} \cdot \vec{\nabla}_v f]^{(1)} = \frac{4\pi^2 e^2 \Omega}{m^2 v^2} \left\{ \frac{\partial}{\partial v} \left( \frac{c_s^2}{v} \frac{\partial \vec{f}_1}{\partial v} \right) - \frac{1}{v} \left( 1 - \frac{c_s^2}{v^2} \right) \vec{f}_1 \right\} \quad (v > c_s) \quad (28)$$

Both terms are zero for very low velocities, when  $v < c_s$ . The parameter  $\Omega$ , a measure of the turbulence energy, is the average fluctuation energy density per wavelength:

$$\Omega \equiv 4\pi \int k W(k) dk. \quad (29)$$

With the turbulence term of eq. (28) added, eq. (12) becomes a vector differential equation in  $v$  which is difficult to solve even with our assumption of equilibrium  $\vec{f}_1$ . Fortunately, it is a good assumption to neglect the differential terms in both eq. (28) and eq. (27), since  $c_s^2/v_{th}^2 = Zm_e/m_i \ll 1$ . Thus:

$$\left( \frac{\partial f_0}{\partial t} \right)_{turb} = \vec{\nabla}_v \cdot [\mathcal{D} \cdot \vec{\nabla}_v f]^{(0)} = 0 \quad (30)$$

$$\left( \frac{\partial \vec{f}_1}{\partial t} \right)_{turb} = \vec{\nabla}_v \cdot [\mathcal{D} \cdot \vec{\nabla}_v f]^{(1)} = \beta \nu_{ei} \vec{f}_1(v) \quad (31)$$

where the turbulence strength parameter is

$$\beta \equiv \frac{4\pi^2 e^2 \Omega}{Z m^2 v_{th}^3 \nu_R}. \quad (32)$$

Thus, ion-acoustic turbulence just acts to multiply the electron-ion collision frequency by a factor  $\beta$ . The magnitude of  $\beta$  can be roughly estimated by noting that, if  $\ell$  is the dominant length scale of the fluctuations, then  $\Omega \approx \ell \times [\text{Fluctuation energy density}]$ , and so

$$\beta \sim \frac{\omega_e}{Z\nu_R} \frac{\ell}{\lambda_D} f_E, \quad (33)$$

where  $f_E$  is the fraction of thermal energy contained in the fluctuations.

The fluctuation energy  $f_E$  is generally proportional to  $N \equiv n\lambda_D^3$ , the number of particles in a Debye sphere; for most plasmas,  $N \gg 1$ . The exact relationship depends on the degree of turbulence in the plasma. In a non-turbulent plasma, the well-known result is that  $f_E \sim N^{-1}$ ; for moderate, fully-developed turbulence, where the instability growth has saturated,  $f_E \sim N^{-1/2}$ ; and for strong turbulence,  $f_E \sim N^0$ , and the fluctuation energy is comparable to the thermal energy.<sup>11</sup> We account for this by writing

$$f_E = N^{-\gamma} \quad (34)$$

where  $0 < \gamma < 1$ ; for saturated microturbulence,  $\gamma \approx \frac{1}{2}$ . Using the relationship  $\omega_e/\nu_R = 2\pi N/\log \Lambda$ , where  $2\pi/\log \Lambda$  is of order one, the turbulent enhancement in collision frequency is

$$\beta \approx \frac{\ell}{Z\lambda_D} N^{1-\gamma}. \quad (35)$$

Table 1 shows the value of  $N$  for various plasma conditions. For ion-acoustic turbulence, it is commonly assumed that  $\ell \approx \lambda_D$ . There are a wide range of possible enhancements to the collision frequency due to ion-acoustic microturbulence; for typical PRS conditions, factors of 10–100 are not unreasonable.

**Table 1. Debye length (nm),  $N$  = particles in Debye Sphere.**

Density (cm <sup>-3</sup> )	Temperature (eV)			
	10	100	500	1000
10 <sup>16</sup>	235 N=130	743 N=4,100	1,660 N=45,900	2,350 N=130,000
10 <sup>18</sup>	23.5 N=13	74.3 N=410	166 N=4,590	235 N=13,000
10 <sup>20</sup>	2.35 N=1.30	7.43 N=41	16.6 N=459	23.5 N=1,300
10 <sup>22</sup>	0.24 N=0.13	0.74 N=4.10	1.66 N=45.9	2.35 N=130

The increase in the effective collision frequency is enough in itself to significantly increase the resistivity of the plasma. In addition, the turbulence changes the shape of the distribution function

in a way that also increases the resistivity. The modification to the kinetic equation, eq. (11), due to turbulence is found by including the turbulence term of eq. (31) in the solution to eq. (12). The solution for  $C_{EB}$  remains in the form of eq. (18), but instead of  $\nu_{ei}$  the effective collision frequency

$$\nu_{ei}^{eff} \equiv (1 + \beta)\nu_{ei} \quad (36)$$

must be used. If the magnetic field is low, this increase in collision frequency changes the magnitude of the ohmic heating term; if the magnetic field is high, the higher collision frequency changes primarily the nature of the heating.

#### 4. Characteristics of Non-Maxwellian Terms

For computation it is useful to introduce dimensionless units, such that

$$\tau \equiv \nu_R t \quad (37)$$

$$\epsilon \equiv mv^2/2\kappa T. \quad (38)$$

We define the turbulence-modified effective collision frequency at the thermal velocity as  $\nu_{eff} \equiv \nu_{ei}^{eff}(v_{th})$ . The fields are normalized to  $\Omega_c \equiv \omega_c/\nu_R$ , and  $\mathcal{E} \equiv E/E_D$ , where  $E_D = mv_{th}\nu_R/e$  is the Dreicer field,<sup>12</sup> sufficient to cause runaway in unmagnetized systems. The new distribution function, normalized to 1, is  $f(\epsilon) \equiv (v_{th}^3/2n)f(v)$ . It obeys the normalized kinetic equation, which is, from eq. (11),

$$\frac{df_0}{d\tau} = C_{EB}(\epsilon) + C_{FP}(\epsilon) + C^*(\epsilon) \quad (39)$$

where the terms on the right-hand side are given below. In normalized units, the characteristic time in which any term will significantly modify the distribution function is equal to the magnitude of that term, in units of  $\nu_R^{-1}$ . The Fokker-Planck elastic collision term is derived from eq. (14):

$$C_{FP} = \frac{2}{\sqrt{\epsilon}} \frac{\partial}{\partial \epsilon} \left\{ f_0 \int_0^\epsilon f_0(\epsilon') \epsilon'^{1/2} d\epsilon' + \frac{2}{3} \frac{\partial f_0}{\partial \epsilon} \left[ \int_0^\epsilon f_0(\epsilon') \epsilon'^{3/2} d\epsilon' + \epsilon^{3/2} \int_\epsilon^\infty f_0(\epsilon') d\epsilon' \right] \right\}. \quad (40)$$

The small-angle collisions represented by  $C_{FP}$  cause the electrons to approach a Maxwell-Boltzmann distribution from any initial state. Acting against the tendency to approach a Maxwellian are the heating term represented by  $C_{EB}$  and the radiative cooling term represented by  $C^*(\epsilon)$ . The importance of these other terms in driving the distribution from a Maxwellian can be estimated by comparing their magnitude to  $C_{FP}$ .

The ohmic heating term in eq. (39) is, from eq. (18),

$$C_{EB}(\epsilon) = \frac{A_{EB}}{\sqrt{\epsilon}} \frac{\partial}{\partial \epsilon} \left[ g(\epsilon) \frac{\partial f_0}{\partial \epsilon} \right] \quad (41)$$

where

$$A_{EB} = \frac{4\nu_{eff}}{3\nu_R} \left( \frac{\mathcal{E}}{\Omega_c} \right)^2 \quad (42)$$

and the shape function

$$g(\epsilon) = \frac{\epsilon^3}{(\nu_{eff}/\omega_c)^2 + \epsilon^3} \quad (43)$$

determines where the heating is focused. When there is no turbulence,  $\nu_{eff}/\nu_R = Z$  (see eq. (36)). This form of  $C_{EB}$  is most convenient when  $\omega_c \gg \nu_{eff}$ .

The inelastic-collision term in eq. (39) is just as in eq. (15), but with the collision frequency normalized by dividing by  $\nu_R$ :

$$C^* = \frac{\alpha_{FS}^{-2} f_a \Omega_{ab} / g_a}{4Z \log \Lambda_{ee}} \frac{\kappa T}{mc^2 \sqrt{\epsilon}} \sum_j [-f_0(\epsilon) \theta(\epsilon - \epsilon_j) + f_0(\epsilon + \epsilon_j)]. \quad (44)$$

Here,  $\alpha_{FS} \approx 1/137$  is the fine structure constant,  $f_a$  is the fraction of ions in state  $a$ ,  $g_a$  is the multiplicity of state  $a$ , and  $\Omega_{ab}(\epsilon)$  is the collision strength discussed in connection with eq. (9).  $\Omega_{ab}(\epsilon)$  varies slowly with  $\epsilon$ .

The effect of ohmic heating on the distribution is determined by both the relative magnitude of  $C_{EB}$  and the shape function  $g(\epsilon)$ , which contributes to the magnitude when  $\omega_c \ll \nu_{eff}$ . The relative magnitude is roughly

$$|C_{EB}| \approx \frac{A_{EB}}{(\nu_{eff}/\omega_c)^2 + 1}. \quad (45)$$

Ohmic heating significantly influences the distribution function only where  $|C_{EB}| > 1$ . If the magnetic field is small ( $\omega_c \ll \nu_{eff}$ ),  $|C_{EB}|$  is proportional to  $E^2/\nu_{eff}\nu_R$ , and electron collisions and turbulence limit the influence of ohmic heating on the distribution. The low-field ohmic heating rate is inversely proportional to  $\nu_{eff}$  (the dimensional heating rate is  $C_{EB}(\epsilon)$  multiplied by  $\nu_R$ ). For a high magnetic field ( $\omega_c \gg \nu_{eff}$ ),  $|C_{EB}|$  is proportional to  $(\nu_{eff}/\nu_R)(E/B)^2$ , and the magnetic field limits the relative influence on the distribution. High-field ohmic heating increases linearly with  $\nu_{eff}$ , because collisions increase the current flow by interfering with the magnetic field confinement.

The shape function  $g(\epsilon)$  determines the form of the ohmically heated distribution. As shown in fig. (1), it increases rapidly from zero and asymptotically approaches its maximum value of 1. In general, low-energy particles (much below the inflection point) experience little heating, because the large low-energy collision rates effectively randomize the electron motion and prevent the electric field from doing net work on electrons. High-energy particles (much above the inflection point) are easier to heat up because more phase space is available to them.

When the magnetic field is low,  $g(\epsilon)$  rises rapidly ( $\sim \epsilon^3$ ) in the most populated energy range. The resulting electron distribution is greatly enhanced at high energies compared to a Maxwellian,

reflecting the runaway phenomenon, wherein faster electrons are more efficiently heated than slower electrons. For intermediate magnetic fields, the distribution is non-Maxwellian, with a local enhancement due to heating. With a large magnetic field,  $g(\epsilon)$  is nearly constant for most electrons, and the distribution shape is self-similar (as discussed below).

In a moderate magnetic field, ohmic heating results in a distribution function with an enhancement at intermediate energies but with a depleted high-energy tail relative to a same-temperature Maxwellian. From the form of  $C_{EB}$ , it is clear that this enhancement will be somewhere near the rapid rise of  $g(\epsilon)$ , although exactly where will depend on the shape of the distribution function. The slope of  $g(\epsilon)$  is maximized at the inflection point

$$\epsilon_0 \equiv \left( \frac{\nu_{eff}^2}{2\omega_c^2} \right)^{1/3}, \quad (46)$$

and so this makes a convenient estimate of the focus of ohmic heating. Actually, the falloff of the distribution function with energy will make  $\epsilon_0$  an underestimate. Fig. (2) shows numerically-determined values for the energy of greatest ohmic heating, when the heated distribution is a Maxwellian.

For very weak magnetic fields, the ohmic heating focus, with its distribution function enhancement, moves out to higher energies, and the depletion in the tail above  $\epsilon_0$  becomes less important. When  $\omega_c \rightarrow 0$ , the enhanced-tail runaway distribution is produced. For very strong magnetic fields, the ohmic heating focus moves to lower energies, and when  $\omega_c \rightarrow \infty$  the distribution takes on a depleted-tail, or "flat-topped", self-similar form.

Ohmic heating in a strong magnetic field produces a "self-similar" solution<sup>13</sup> for the distribution, in the same form as the distributions produced by inverse-bremsstrahlung laser heating. When  $\omega_c \gg \nu_{eff}$ , then  $g(\epsilon) \approx 1$ , and if inelastic collisions are neglected the solution to eq. (39) has the form:

$$f_m(\epsilon, y) = \frac{a_m}{y_m^{3/2}} e^{-(\epsilon/y)^{m/2}} \quad (47)$$

where the normalization and kinetic energy integrals determine

$$a_m = \frac{m}{8\pi\Gamma(3/m)} \quad (48)$$

$$y_m = \frac{3\Gamma(3/m)}{2\Gamma(5/m)} \kappa T_0 \quad (49)$$

and  $\kappa T_0 = 1$  for the normalized distributions. With electron-electron collisions alone,  $m = 2$  (a Maxwellian). With ohmic heating alone,  $m = 5$ . With ohmic heating plus electron-electron collisions,  $2 \leq m \leq 5$ :<sup>3</sup>

$$m = 2 + \frac{3}{1 + 1.66/\alpha^{0.724}} \quad (50)$$

where

$$\alpha \equiv \frac{\nu_{eff}}{3\nu_R} \left( \frac{\mathcal{E}}{\Omega_c} \right)^2. \quad (51)$$

The ratio of the self-similar distribution to a same-temperature Maxwellian is plotted in fig. (3).

The characteristics of ohmically-heated distribution functions discussed above are illustrated in fig. (4) and fig. (5). These show the evolution of an initially-Maxwellian distribution function under the influence of ohmic heating only. In fig. (4), the magnetic field is low:  $\omega_c/\nu_{eff} = 1/99$ , and the enhancement near  $\epsilon = 8$  can be seen. In fig. (5), the magnetic field is moderately high:  $\omega_c/\nu_{eff} = 99$ , and the distribution, while enhanced near  $\epsilon = 1$ , has mostly the character of the self-similar solution.

The inelastic collision term has a different (non-differential) character from the other terms in eq. (39); to estimate its importance relative to electron-electron elastic collisions, we first simply take the ratio of the inelastic to elastic collision frequencies, given by eq. (9) and eq. (7), respectively

$$\dots \frac{\nu_{ab}^*}{\nu_{ee}} = A^* \epsilon, \quad (52)$$

where

$$A^* = 1.838 \times 10^{-2} \frac{\kappa T}{Z \log \Lambda_{ee}} \frac{f_a \Omega_{ab}}{g_a}. \quad (53)$$

This ratio is generally small; since the only terms not of order one are  $Z$  and  $\log \Lambda$ , which are each near 10, an effect of perhaps a few percent might be anticipated from inelastic collisions. Greater effects should appear in the tail of the distribution, in particular at energies greater than  $Z$  times the thermal energy. The effect of inelastic collisions will be significantly greater, however, at higher temperatures (above 1 keV).

The effect of inelastic collisions is to enhance the distribution function tail, relative to a same-temperature Maxwellian. This is paradoxical, because collisional excitation shifts electrons out of distribution tail, into the bulk. But the scattering cools the system, and the net result is a relative enhancement in the tail, compared to the cooled Maxwellian. In thermal equilibrium, or for a fixed cooling rate, inelastics tend to produce enhancements at low energy, depletions near the threshold energy, and enhancements in the tail. This is illustrated in fig. (6), which plots the time-development of an initially Maxwellian distribution under the influence of inelastic collisions alone.

Compared to ohmic heating, inelastic collisions are much more important at low electron energy, but much less important at high energy. For a Maxwellian distribution, the approximate ratio is

$$\frac{C_{Ohmic}}{C_{Inel}} \approx \sum_{ab} \frac{A_{EB}}{A^*} \frac{[\epsilon(y + \epsilon^3) - 3]\epsilon^2}{(y + \epsilon^3)^2} \quad (54)$$



where

$$y \equiv (\nu_{eff}/\omega_c)^2. \quad (55)$$

The energy dependence of this ratio is shown in fig. (7), for various magnetic field strengths. The figure shows the ratio of ohmic to inelastic terms, divided by the high-energy limit of this expression, which is

$$\left. \frac{C_{Ohmic}}{C_{Inel}} \right|_{\epsilon \rightarrow \infty} = \frac{72.5 Z(\nu_{eff}/\nu_R) \log \Lambda}{\kappa T (f_a \Omega_{ab}/g_a)} \left( \frac{\mathcal{E}}{\Omega_c} \right)^2 \quad (56)$$

## 5. Conductivity in an inductive system

The kinetic theory presented here is expressed in terms of the electric field ( $\vec{E}$  or  $\mathcal{E}$ ) in the plasma. In an inductive system like a z-pinch, however, it is more convenient to use the current density  $\vec{j}$  as a parameter. Current and electric field are related by the conductivity  $\sigma$ , which in a magnetized system is a tensor:

$$\vec{j} = \sigma \cdot \vec{E} \quad (57)$$

The resistivity tensor is defined as  $\eta \equiv \sigma^{-1}$ . We will now show how to calculate "scalar" conductivities (or resistivities), which we can use to find the effective electric field for the kinetic model. This can also be used to correct MHD transport codes when the distribution function is non-Maxwellian.

There are two useful ways to define scalar conductivities. Both ways use the same conductivity parallel to the magnetic field, which is unaffected by the field. Consider the current perpendicular to the magnetic field. In the first approach, the "field representation", the electric field is given and the scalar conductivities determine the components of the current density vector parallel to and perpendicular to it. In the second approach, the "current representation", the current density is given, and the scalar resistivity determines the components of the electric field parallel and perpendicular to the current.

If total current density is  $\vec{j}$  (transverse to the magnetic field) and total electric field is  $\vec{E}$ , the field representation Ohm's law gives the current components  $j_{\perp}$  parallel to  $\vec{E}$  and  $j_{\wedge}$  perpendicular to  $\vec{E}$ :

$$j_{\perp} = \sigma_{\perp} E \quad (58)$$

$$j_{\wedge} = \sigma_{\wedge} E \quad (59)$$

The components of the current distribution function  $f_1(v)$  in these directions can easily be found in eq. (17). Similarly,  $\vec{E}$  has components  $E_{\perp}$  parallel to and  $E_{\wedge}$  perpendicular to  $\vec{j}$ , which are determined the current representation Ohm's law:

$$E_{\perp} = \eta_{\perp} j \quad (60)$$

$$E_{\wedge} = \eta_{\wedge} j. \quad (61)$$

Note that it is *not* true that, e.g.,  $\eta_{\perp} = \sigma_{\perp}^{-1}$ . The relationship between the field-representation conductivities and the current-representation resistivities is found by rotating from one representation to the other:

$$\eta_{\perp} = \frac{\sigma_{\perp}}{\sigma_{\perp}^2 + \sigma_{\parallel}^2} \quad (62)$$

$$\eta_{\parallel} = \frac{\sigma_{\parallel}}{\sigma_{\perp}^2 + \sigma_{\parallel}^2} \quad (63)$$

The current-representation resistivities are those most often used<sup>4,8</sup> in MHD models, and  $\eta_{\perp}$  is referred to as the “Spitzer” resistivity.

As the magnetic field increases to infinity, the field-representation conductivities go to zero: The drift velocity becomes vanishingly small, and the electron gyroradius also vanishes, eliminating the effect of collisions. This is called magnetic insulation. Paradoxically, the current-representation resistivities do not become infinite for an infinite magnetic field; in fact, the Spitzer transverse resistivity  $\eta_{\perp}$  for infinite magnetic field is well known to be only about twice the zero-field value. To explain this paradox, we take as an example a simple conductivity model.<sup>14</sup> By following the motion of a single electron under electric field acceleration and collisional drag, we can estimate the field-representation conductivity as

$$\sigma_{\perp}^e = \frac{\sigma_{\parallel}^e}{1 + (\omega_c/\nu)^2}, \quad \sigma_{\parallel}^e = \frac{(\omega_c/\nu)\sigma_{\parallel}^e}{1 + (\omega_c/\nu)^2} \quad (64)$$

where  $\nu$  is a collision frequency and  $\sigma_{\parallel}^e = ne^2/m\nu$  is the zero-field conductivity. These conductivities do properly go to zero as the magnetic field becomes infinite. The current-representation resistivities are:

$$\eta_{\perp}^e = (\sigma_{\parallel}^e)^{-1}, \quad \eta_{\parallel}^e = \frac{\omega_c}{\nu} (\sigma_{\parallel}^e)^{-1} \quad (65)$$

For this model, the “Spitzer” resistivity  $\eta_{\perp}$  is completely unaffected by the magnetic field. How can this be? When the magnetic field is increased, the cross-field resistivity  $\eta_{\parallel}$  also increases, indicating an increase in the electric field perpendicular to the current. If the magnetic field increases to infinity, so does this cross-current electric field. The ratio between the field  $E_{\perp}$  along the current and the field  $E_{\parallel}$  transverse to the current is

$$E_{\perp}/E_{\parallel} = \nu/\omega_c. \quad (66)$$

The current representation, in postulating a finite current, does not allow a magnetic field cutoff: the resistivity simply determines the electric fields necessary to generate the given current. This resolves the paradox: A “Spitzer” current flowing in an infinite magnetic field is driven by an

infinite electric field transverse to the current flow. In the field representation, by contrast, a finite electric field is postulated, and the resulting currents are calculated. An inductive system (like a PRS) is best described in the current representation, since the driver is capable of producing large electric fields to maintain the current flow.

In our kinetic model, the field representation conductivities can be straightforwardly calculated from eq. (17), using eq. (4):

$$\sigma_{\perp} = \frac{2}{3} \frac{\omega_e^2}{\nu_{eff}} \int_0^{\infty} \frac{\epsilon^3}{1 + (\omega_c/\nu_{eff})^2 \epsilon^2} \frac{\partial f_0}{\partial \epsilon} d\epsilon \quad (67)$$

$$\sigma_{\parallel} = \frac{2}{3} \frac{\omega_e^2}{\nu_{eff}} \left( \frac{\omega_c}{\nu_{eff}} \right) \int_0^{\infty} \frac{\epsilon^{5/2}}{1 + (\omega_c/\nu_{eff})^2 \epsilon^2} \frac{\partial f_0}{\partial \epsilon} d\epsilon. \quad (68)$$

This form is most convenient for  $\omega_c \ll \nu_{eff}$ , but these expressions are general. The Spitzer resistivity can now be found from eq. (62). In the highly-magnetized, large- $\omega_c$  limit, where the self-similar solution of eq. (47) is valid, the Spitzer resistivity has a simple limit:

$$\lim_{\omega_c \rightarrow \infty} \eta_{\perp} = \frac{32\pi^2}{3} \frac{\nu_{ei}^{th}}{\omega_e^2} f_0(0). \quad (69)$$

In the unmagnetized limit, the expression involves an integral which must be evaluated for the particular distribution function. In any case, the resistivity is of the form

$$\eta_{\perp} = A_{\perp} \frac{Z \log \Lambda}{(\kappa T)^{3/2}} \text{ sec}. \quad (70)$$

The constant  $A_{\perp}$  is shown in Table 2 for integral values of the self-similar parameter  $m$ , both for unmagnetized and strongly magnetized plasma, with no turbulence included.

**Table 2. Resistivity coefficient  $A_{\perp}$  for different distributions**

Magnetic field	$m = 2$	$m = 3$	$m = 4$	$m = 5$
$B = 0$	$3.3798 \times 10^{-15}$	$3.5612 \times 10^{-15}$	$3.6521 \times 10^{-15}$	$3.7056 \times 10^{-15}$
$B = \infty$	$1.1475 \times 10^{-14}$	$7.1223 \times 10^{-15}$	$5.7471 \times 10^{-15}$	$5.1133 \times 10^{-15}$

In the unmagnetized plasma, a Maxwellian distribution has the highest resistivity, because higher- $m$  distributions have fewer fast, tail electrons. The resistivity for an  $m = 5$  distribution is slightly (0.91 times) lower than a Maxwellian. In the strongly-magnetized plasma, conversely, the Maxwellian has the lowest resistivity. The strong magnetic field efficiently confines the tail electrons and makes the low-energy, bulk electron the current carriers. The magnetized resistivity of the  $m = 5$  distribution is less than that of a Maxwellian by a factor of 2.24.

Table 3 lists the resistivities of several elements (most of which are used as PRS radiators), for comparison with the magnitudes of the plasma resistivities presented here.

**Table 3. Selected electrical resistivities<sup>15</sup>***Given in units of  $10^{-18}$  sec; 1 microhm-cm =  $\frac{1}{9} \times 10^{-17}$  sec.*

ELEMENT	77° K	273° K	373° K
Mg	0.69	4.33	6.22
Fe	0.73	9.89	16.3
Cu	0.22	1.73	2.49
Ag	0.33	1.68	2.37
Au	0.56	2.27	3.16
Zn	1.22	6.11	8.67
Al	0.33	2.72	3.94
Se	15.0	13.3	—

In the presence of turbulence, the resistivity uniformly increases due to the increase in  $\nu_{eff}$ , although the extent of the increase depends most importantly on the magnetic field strength, form of the distribution function, and temperature. In fig. (8), the increase in resistivity with turbulence strength is shown for the  $m = 2$  and  $m = 5$  distributions in a large magnetic field. With a weak magnetic field, the curves would look similar, but the Maxwellian ( $m = 2$ ) resistivity would be less than that of the  $m = 5$  distribution, and the effect of turbulence would be less pronounced.

By symmetry, the current density  $\vec{j}$  must be along the pinch ( $\hat{z}$ ) axis. This situation is enforced by the presence of radial charge-separation electric fields ( $E_{\perp}, E_{\parallel}$ ). As we have shown, the radial electric fields can become extremely large. The total electric field makes an angle  $\theta_j = \tan^{-1}(\sigma_{\parallel}/\sigma_{\perp})$  with the pinch axis. The magnitude of the total electric field, used in our kinetic model, is related to the total (axial) current density by:

$$E = \frac{1}{\sqrt{\sigma_{\perp}^2 + \sigma_{\parallel}^2}} j. \quad (71)$$

For a given current density,  $E$  increases with magnetic field, roughly as  $B$  for high fields.

The electron flow, as given by  $\vec{f}_1(v)$ , is not generally parallel to the current, but rather changes direction with velocity. Thus, there are always electron flows intermixing throughout the radial extent of the pinch. These flows have the potential to both enhance radial transport and seed instabilities not discussed here. Such anisotropies in the flow are discussed below.

## 6. Runaway electrons

Because the electron collision rates decrease rapidly with relative energy (see eq. (7)), particles with large enough kinetic energy are not affected by collisions and become runaways. With no magnetic field, "runaway" electrons are those with a velocity greater than the critical velocity<sup>12</sup>  $v_c \approx v_{th} \sqrt{3E_D/E}$ . The critical velocity  $v_c$  is independent of  $v_{th}$ , but as the unmagnetized system is heated and  $v_{th}$  increases, an increasing number of electrons have velocities above  $v_c$  and thus run away.

A magnetic field inhibits this free acceleration of electrons. In a collisionless plasma with  $B > E$  (in Gaussian units), free-streaming electron motion across field lines is impossible, being replaced by a combination of cyclotron and  $\vec{E} \times \vec{B}$  drift motions. When  $B < E$ , collisionless electrons can be accelerated across field lines, although the magnetic field reduces the magnitude of the acceleration. This high-electric field acceleration might, in connection with neck formation, cause z-pinch runaways.<sup>16</sup> The large radial fields required for axial current propagation in the magnetized system could also promote this type of runaway, as could the presence of turbulence. Predictions of electric and magnetic fields inside the pinch require a model of how current and fields penetrate inside and their consequent relationship.

In the bulk of the current-carrying region,  $B > E$ , and high-energy electrons are confined by the magnetic field. To identify "runaways", we look for combinations of parameters that generate directional and/or monoenergetic beams. Finite-size effects can be estimated using the mean free path and the physical dimensions of the system. Or, the rate at which high-energy electrons are produced can be found by defining a runaway velocity threshold and calculating the electron flux past this threshold.

Anisotropy in the electron velocity distribution is given by  $\vec{f}_1(v)$ : Any  $\vec{f}_1(v) > 0$  indicates a directed beam at velocity  $v$ . The angle between  $\vec{f}_1(v)$  and the electric field is easily computed. Both lie in the  $\hat{r}$ - $\hat{z}$  plane, perpendicular to  $\vec{B}$ ; it follows that the angle  $\theta$  between  $\vec{f}_1(v)$  and the  $\hat{z}$  axis is

$$\tan \theta = \theta_j - \frac{\omega_c}{\nu_{eff}} \epsilon^{3/2}, \quad (72)$$

where  $\theta_j$  is the axial angle of  $\vec{E}$ . For a large magnetic field, this anisotropy between average current and individual particle flow acts to isotropize the distribution; electron-ion collisions, by interfering with the magnetic field, act to preserve the electric-field anisotropy. Just the opposite happens with a low magnetic field, where electron-ion collisions isotropize the distribution.

Future work on runaways will be directed towards determining how current and fields penetrate into the pinch. Given the current and field distribution, the kinetic theory developed here can be utilized to investigate where and how high-energy and high-anisotropy electron flows originate.

## 7. Model calculations

The actual electron distribution function is a product of the interplay between electron-electron collisions, ohmic heating and electron-ion excitation collisions, as described above. To investigate the behavior of the distribution function in high-power PRS machines such as DECADE, we have numerically solved eq. (39) for the time-evolving distribution. In particular, we are looking for an equilibrium distribution shape, which will serve as a generalization of the self-similar form of eq. (47) to moderate magnetic fields and the presence of inelastic collisions. Therefore, we

set the ohmic heating strength  $A_{EB}$  such that the ohmic heating rate equals the inelastic cooling rate, which is dependent only on the plasma parameters (e.g., temperature, ionization, electron distribution function). We neglected turbulence; any turbulence would act like an increased ionization level  $Z$ .

**Table 4. Parameters used in numerical solutions**

Case	$B$ (MG)	$\epsilon_{Focus}$	Current (A/cm <sup>2</sup> )	$\frac{C_{Ohmic}}{C_{Inel}} \bigg _{\infty}$
$\kappa T = 500$ eV, $Z = 24.01$ , Radiative power $3 \times 10^{15}$ W				
1	0.93	9.0	$6 \times 10^9$	3.08
2	29.26	4.6	$8 \times 10^9$	0.19
$\kappa T = 1500$ eV, $Z = 28.96$ , Radiative power $8 \times 10^{15}$ W				
3	0.335	9.0	$7 \times 10^9$	0.50
4	10.54	4.6	$9 \times 10^9$	0.35

The numerical solution was for a selenium plasma, of ion density  $n_i = 10^{20}$  cm<sup>-3</sup>. The parameters are summarized in table 4. The atomic model used for selenium included 95 transitions for different ionization stages between the ground state and first excited state; of these, 35 were found to make some contribution under the given plasma conditions. Ion populations were determined by a collisional-radiative equilibrium code. The transitions used are numbered and listed in table 5. The relative importance of each transition can be seen in the bar charts of fig. (9) and fig. (10), which show the contribution of each transition to the total radiative power for each of the two temperatures considered.

The model results are shown in fig. (11), fig. (12), fig. (13) and fig. (14), respectively, for the four cases described in Table 4. For a given temperature, increasing the magnetic field changes the distribution from the runaway distribution of fig. (11) to the self-similar type distribution of fig. (12). The low-energy enhancement of the ohmically-heated distribution seen in fig. (5) is missing from fig. (12) because of the rapid isotropization from electron-electron collisions at low energies. For a given magnetic field, increasing the temperature significantly reduces the non-Maxwellian effects for these parameters. This is both because of the increasing influence at higher temperatures of inelastic collisions relative to ohmic heating and because the higher conductivities at high temperatures lead to lower electric fields in the plasma. Still, distribution function enhancements at higher temperatures do generate significant numbers of electrons at high energies (e.g., at 1500 eV,  $\epsilon = 10$  corresponds to 15 keV).

**Table 5. Transitions used in numerical solutions**

Index	Threshold (eV)	Ionization	Transition
1.	62.1	Li-like	0 - 1
2.	1956.7	Li-like	1 - 2
3.	68.1	Be-like	0 - 1
4.	1954.5	Be-like	0 - 2
5.	1886.5	Be-like	1 - 2
6.	87.7	B-like	0 - 1
7.	1712.3	B-like	0 - 2
8.	1624.5	B-like	1 - 2
9.	117.3	C-like	0 - 1
10.	1765.4	C-like	0 - 2
11.	1648.2	C-like	1 - 2
12.	156.4	N-like	0 - 1
13.	1688.3	N-like	0 - 2
14.	1531.8	N-like	1 - 2
15.	163.6	O-like	0 - 1
16.	1597.1	O-like	0 - 2
17.	1433.5	O-like	1 - 2
18.	1921.1	O-like	1 - 3
19.	180.0	F-like	0 - 1
20.	1642.2	F-like	0 - 2
21.	1462.2	F-like	1 - 2
22.	1890.2	F-like	1 - 3
23.	1897.4	F-like	1 - 4
24.	1530.3	Ne-like	0 - 1
25.	1996.4	Ne-like	0 - 2
26.	466.1	Ne-like	1 - 2
27.	663.8	Ne-like	1 - 3
28.	765.0	Ne-like	1 - 4
31.	468.7	Na-like	1 - 2
33.	656.3	Na-like	1 - 3
35.	750.5	Na-like	1 - 4

## 8. Conclusions

We have presented a model that consistently includes the effects of electron-electron collisions, ohmic or electric-field heating, distribution function cooling by inelastic collisions with ions, and ion-acoustic turbulence. The actual distribution function shape depends on the interaction between these factors.

At moderate temperatures (under 1 keV), the ohmic heating term is the dominant influence on the distribution. This is true even when the ohmic heating and inelastic cooling rates are equal, as shown in fig. (11) and fig. (12). The magnitude of the ohmic term is proportional to the square of the electric field (cf. eq. (41)), which is in turn proportional to the current density and the magnetic field. The relationship is given in eq. (71); a rough estimate comes from using the simple model

of eq. (64):

$$\mathcal{E} = \frac{j}{ne} \frac{\nu_{eff}}{\nu_R} \sqrt{(\omega^2/\nu_{eff})^2 + 1}, \quad (73)$$

where the dimensionless quantity  $\mathcal{E}$  is the ratio of the electric field to the Dreicer field. The exact electric field can always be calculated from eqs. (67–68). Since  $\mathcal{E}$  is determined by the current, we can define a minimum current density for which ohmic heating is important (see the discussion of eq. (45)). The condition will depend on the magnetic field, density and temperature at each point, and so assessing the importance of ohmic heating in any PRS will require a magnetohydrodynamic model that predicts both current penetration and heat flow. As we have shown, ohmic heating effects on the distribution are directly multiplied by microturbulence.

Inelastic collisions become more important at higher temperatures (cf. eq. (53)) and could modify the distribution by up to 10% at keV temperatures. Inelastic collisions oppose high-magnetic field ohmic heating, cooling the distribution so as to produce a relatively enhanced tail. At high temperatures and currents, ohmic heating and inelastic collisions could balance each other and produce a distribution that was close to Maxwellian. Turbulence would disrupt this balance.

When strong-magnetic field ohmic heating dominates, the self-similar distribution  $f_m(\epsilon)$  is a good analytic approximation to the actual distribution function. In hotter plasmas, or for lower current density, or when the current is concentrated on the plasma edge so that  $E/B \gg 1$ , another analytical approximation must be found for the distribution function form. It is always true that the distribution function can be found numerically, by integrating eq. (39).

Establishing the scaling of non-Maxwellian effects for DECADE shot parameters is the next important step. For this, we will need an analytic model of the current and field distribution in the device. We will first assume a uniform axial current density, investigating non-Maxwellian distributions produced in an energy equilibrium. This will establish a baseline for non-Maxwellian production, and allow us to estimate the change in PRS radiative output from that predicted using a Maxwellian distribution. We can then more realistically use a Bennett pressure equilibrium to relate current and temperature profiles, and determine the effect of non-Maxwellian distributions and turbulence<sup>17</sup> on the Pease-Braginskii current and radiative collapse. Radiative effects in DECADE-class z-pinch plasmas are likely to be strongly influenced by these phenomena.

## REFERENCES

1. P. Pulsifer and K.G. Whitney, "Non-Maxwellian electron distributions in z-pinch plasmas," NRL Memorandum Report 6662 (1990).



2. Radiation Hydrodynamics Branch, *Advanced Concepts Theory Annual Report 1991*, NRL Memorandum Report 92-6960 (1992), pp. 32-58.
3. P. Alaterre, J.-P. Matte and M. Lamoureux, *Phys. Rev. A* **34**,1578 (1986).
4. L. Spitzer, Jr. and R. Härm, *Phys. Rev.* **89**,977 (1953).
5. K.G. Whitney and M.C. Coulter, *IEE Trans. Plasma Sci.* **16**, 552 (1988).
6. I.P. Shkarofsky, T.W. Johnston and M.P. Bachynski, *The Particle Kinetics of Plasmas*, Addison-Wesley, 1966.
7. David L. Book, *NRL Plasma Formulary*, NRL Publication 0084-4040 (1987).
8. S.I. Braginskii, in *Reviews of Plasma Physics*, M.A. Leontovich, ed., vol I, p. 205 (Consultants Bureau, New York, 1967).
9. R.C. Davidson and N.A. Krall, *Nucl. Fusion* **17**,1313 (1977).
10. E.C. Field and B.D. Fried, *Phys. Fluids* **7**,1937 (1964).
11. S. Ichimaru, *Basic Principles of Plasma Physics*, W.A. Benjamin, Reading, Massachusetts (1973).
12. H. Dreicer, *Phys. Rev.* **115**,238 (1959), *Phys. Rev.* **117**,329 (1960).
13. A.B. Langdon, *Phys. Rev. Lett.* **44**,575 (1980).
14. C. Kittel, *Introduction to Solid State Physics* (sixth edition), John Wiley & Sons, 1986. See chapter 6, eq. (64).
15. N.W. Ashcroft and N.D. Mermin, *Solid State Physics*, Holt, Rinehart and Winston, New York (1976); G.W.C. Kaye and T.H. Laby, *Tables of Physical and Chemical Constants*, Wiley, New York (1966).
16. B.A. Trubnikov and S.K. Zhdanov, *Sov. Phys.-JETP* **43**,48 (1976).
17. A.E. Robson, *Phys. Rev. Lett.* **63**,2816 (1989).

## Figure Captions

Figure 1. Plot of the shape function  $g(\epsilon)$  for different values of  $\omega_c/\nu_{eff}$ : From left to right, the curves are for  $\omega_c^2/\nu_{eff}^2 = 10, 1$  and  $0.1$ , respectively.

Figure 2. Numerically determined ohmic heating focus energy as a function of  $\omega_c/\nu_{eff}$ . The focus energy is the point of greatest enhancement of an initially Maxwellian distribution function when affected by ohmic heating only. Each curve is for a different distribution function temperature  $\kappa T_0$ : The middle curve is for the initially normalized distribution,  $\kappa T_0 = 1$ , the upper curve is for  $\kappa T_0 = 20$  and the bottom curve is for  $\kappa T_0 = 0.1$ .

Figure 3. Ratio of the self-similar distribution function  $f_m(\epsilon)$  with a same-temperature Maxwellian. Curves A,B,C,D correspond to integral  $m$  values of 2, 3, 4 and 5, in order of greater tail depletion.

Figure 4. Evolution of an initially-Maxwellian distribution under ohmic heating only, in a low magnetic field. Here  $\omega_c/\nu_{eff} = 1/99$  and  $\kappa T = 500$  eV. Shown is the ratio of the distribution with a same-temperature Maxwellian; the curves show the evolution of distribution shape as it heats, from numerical solution of eq. (39).

Figure 5. Evolution of an initially-Maxwellian distribution under ohmic heating only, in a high magnetic field. Here  $\omega_c/\nu_{eff} = 99$ , and  $\kappa T = 500$  eV. Shown is the ratio of the distribution with a same-temperature Maxwellian; the curves show the evolution of distribution shape as it heats, from numerical solution of eq. (39).

Figure 6. Evolution of an initially-Maxwellian distribution under inelastic cooling only. Shown is the ratio of the distribution with a same-temperature Maxwellian; the curves show the evolution of distribution shape as it cools, from numerical solution of eq. (39).

Figure 7. Ratio of magnitudes of the ohmic heating and inelastic cooling terms, as a function of energy. This plot gives only the dependence of  $\epsilon$ ; the abscissa is in units of  $A_{EB}/A^*$ , as given in eq. (56).

Figure 8. Electrical resistivity (sec) as a function of turbulence level  $\eta_{eff}/\eta_{ei}$ . Solid curve is for a Maxwellian, dashed curve is for the  $m = 5$  depleted-tail distribution. A strong (1 MG) magnetic field emphasizes the difference between curves.

Figure 9. Power density, in  $\text{W}/\text{cm}^3$ , generated by each selenium inelastic collisional transition (listed in Table 5), at  $\kappa T = 500$  eV. The total radiative power density was  $3 \times 10^{15} \text{ W}/\text{cm}^3$  at this temperature.

Figure 10. Power density, in  $\text{W/cm}^3$ , generated by each selenium inelastic collisional transition (listed in Table 5), at  $\kappa T = 1500$  eV. The total radiative power density was  $8 \times 10^{15} \text{ W/cm}^{-3}$  at this temperature.

Figure 11. Numerical results for the evolution of the distribution function in time under energy-equilibrium conditions. Shown is the ratio of the distribution function with a same-temperature Maxwellian. Time between successive curves A,B,C... is  $\tau_{ee}$ . This is low magnetic field, low temperature case 1:  $B = 0.93$  MG,  $\kappa T = 500$  eV. Other parameters are shown in Table 4.

Figure 12. Numerical results for the evolution of the distribution function in time under energy-equilibrium conditions. Shown is the ratio of the distribution function with a same-temperature Maxwellian. Time between successive curves A,B,C... is  $\tau_{ee}$ . This is high magnetic field, low temperature case 2:  $B = 29.26$  MG,  $\kappa T = 500$  eV. Other parameters are shown in Table 4.

Figure 13. Numerical results for the evolution of the distribution function in time under energy-equilibrium conditions. Shown is the ratio of the distribution function with a same-temperature Maxwellian. Time between successive curves A,B,C... is  $\tau_{ee}$ . This is low magnetic field, high temperature case 3:  $B = 0.34$  MG,  $\kappa T = 1500$  eV. Other parameters are shown in Table 4.

Figure 14. Numerical results for the evolution of the distribution function in time under energy-equilibrium conditions. Shown is the ratio of the distribution function with a same-temperature Maxwellian. Time between successive curves A,B,C... is  $\tau_{ee}$ . This is high magnetic field, high temperature case 4:  $B = 10.54$  MG,  $\kappa T = 1500$  eV. Other parameters are shown in Table 4.

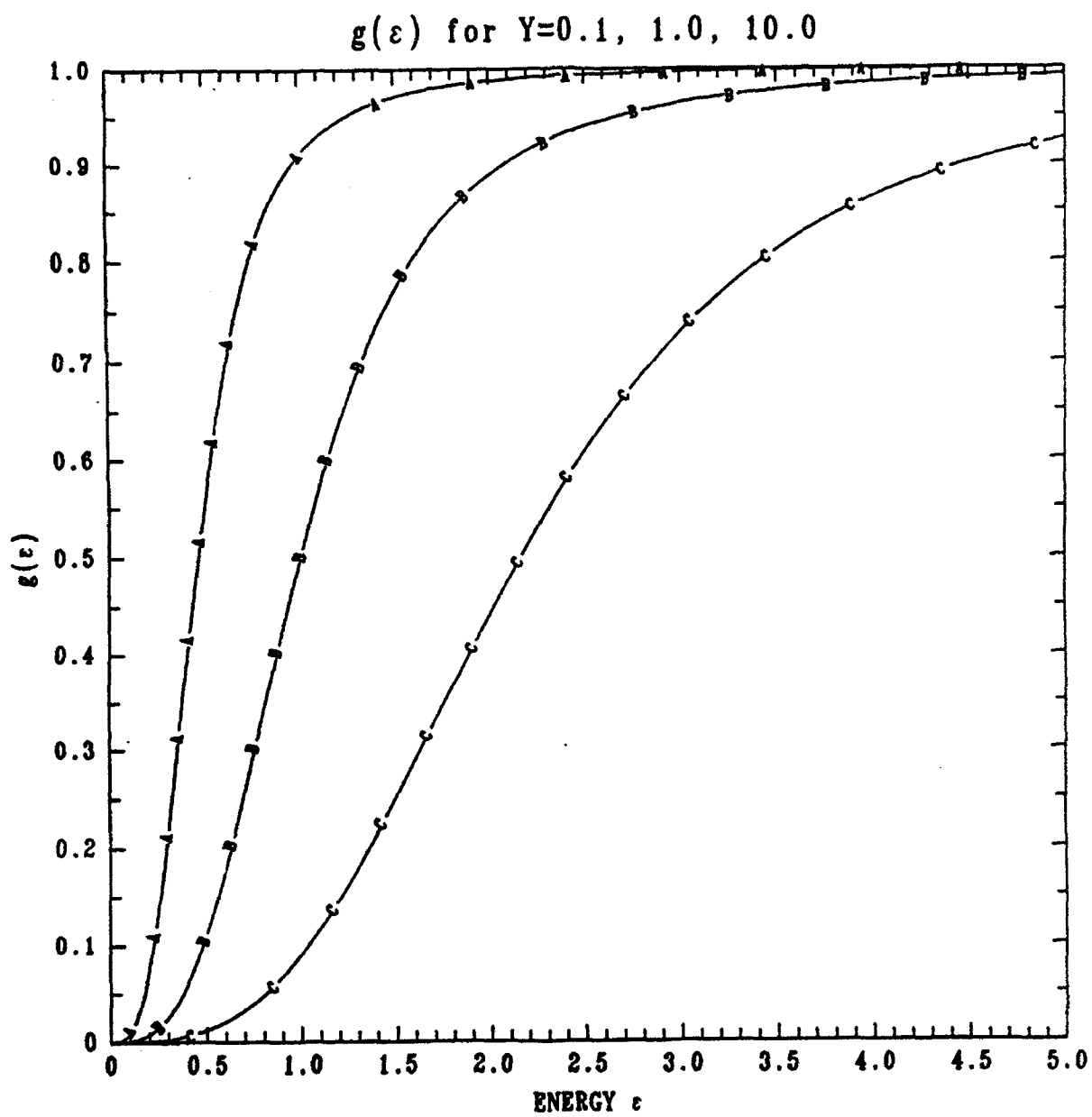


Figure 1

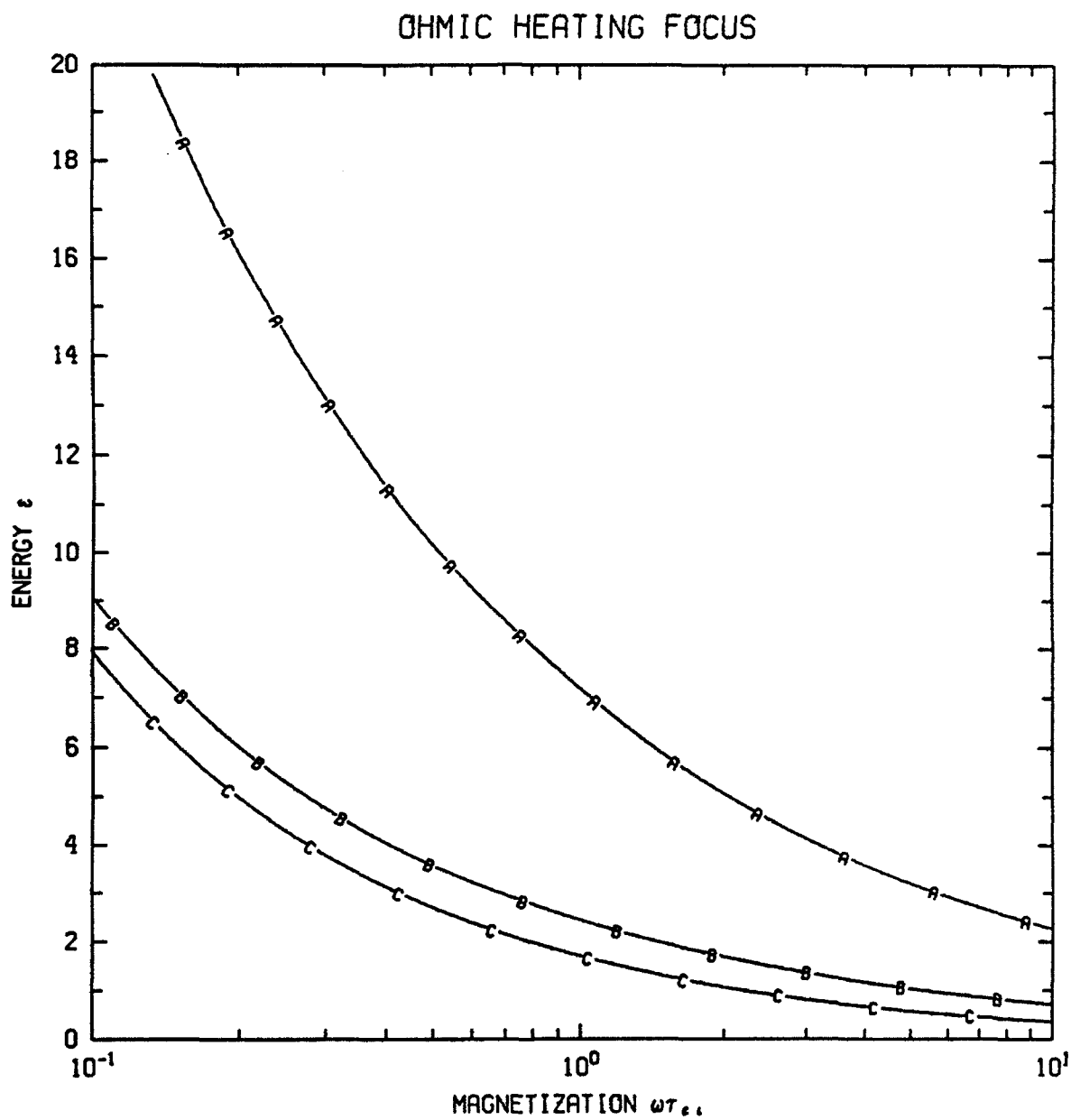


Figure 2

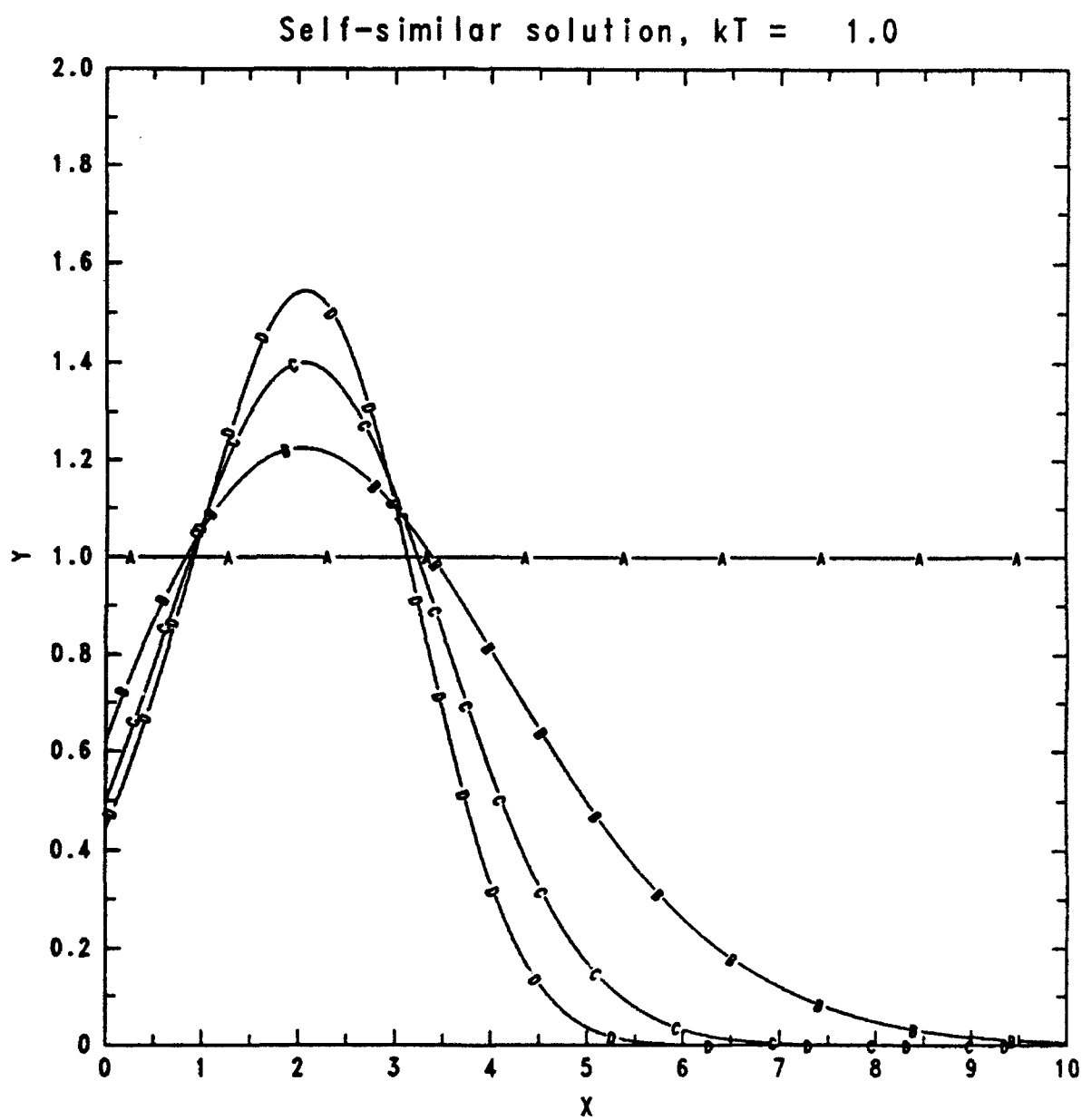


Figure 3

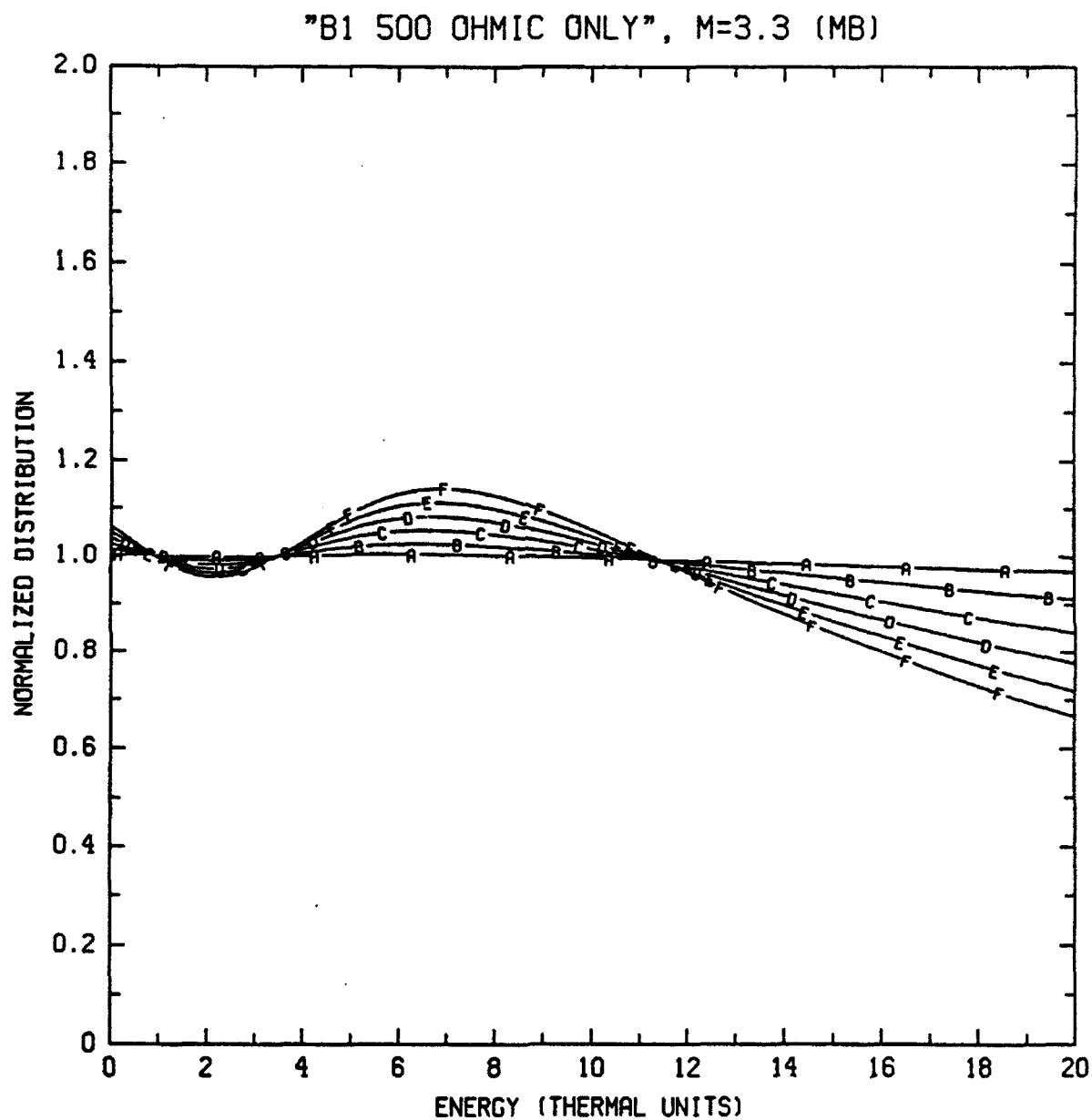


Figure 4

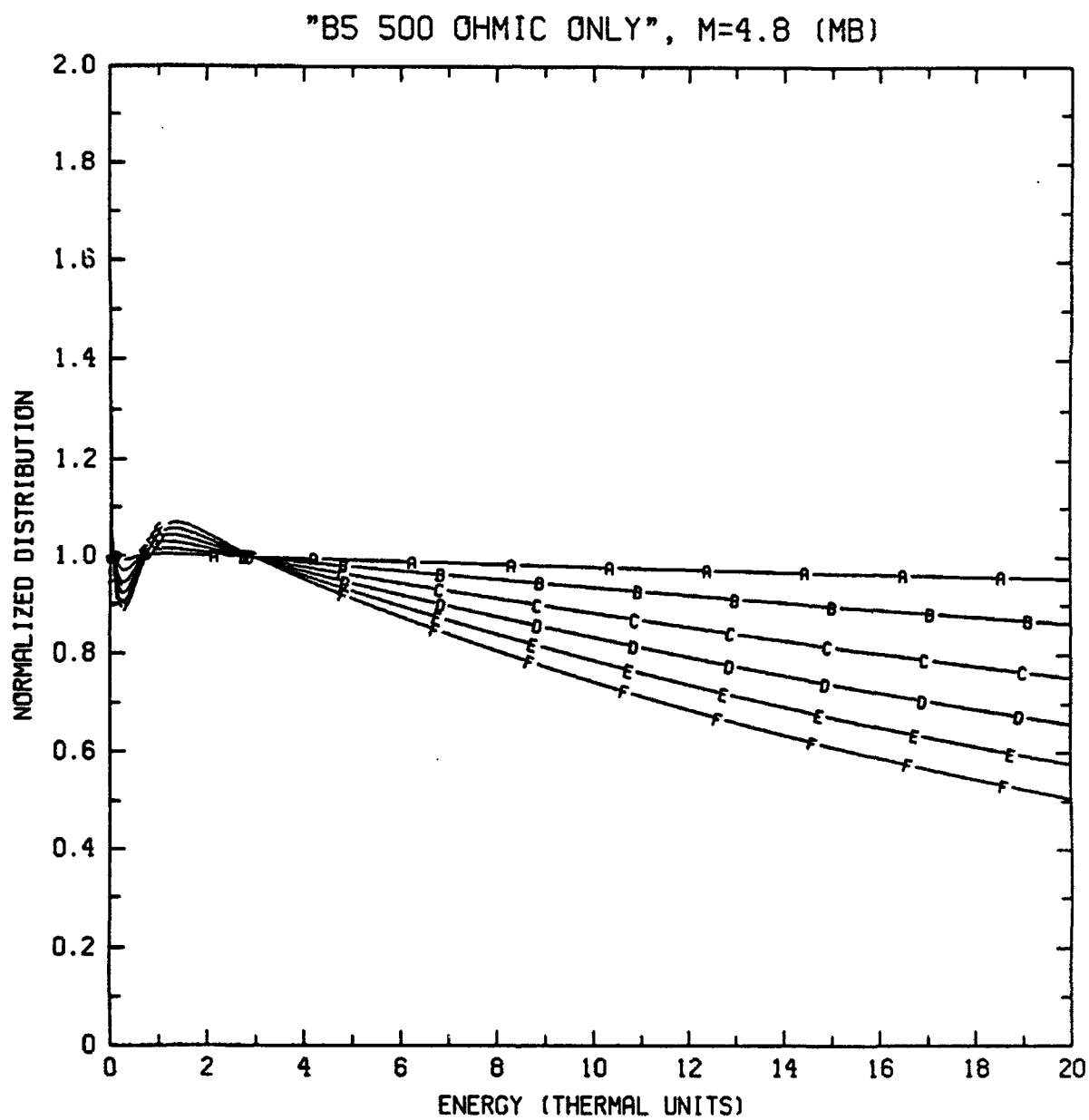


Figure 5



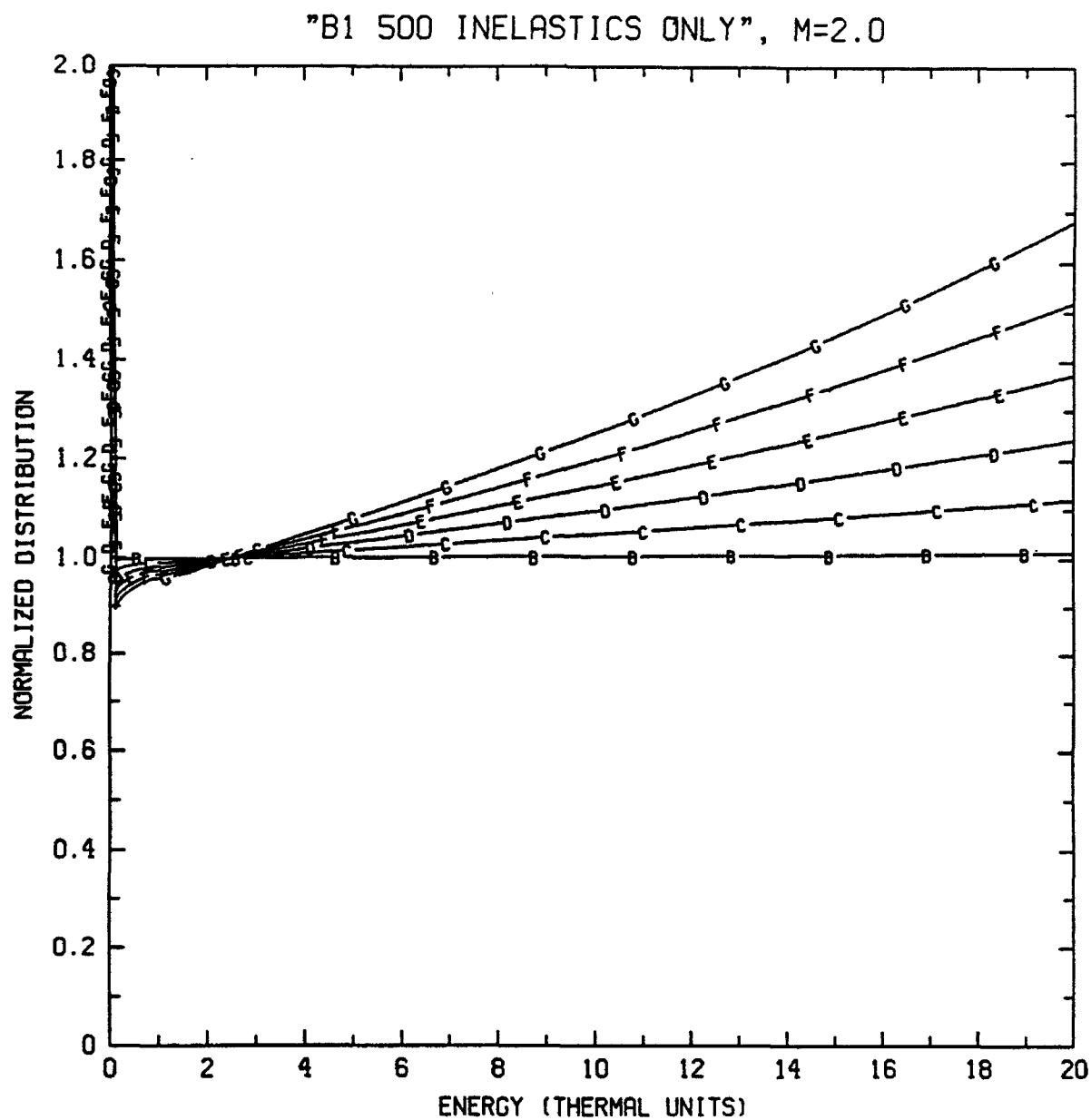


Figure 6

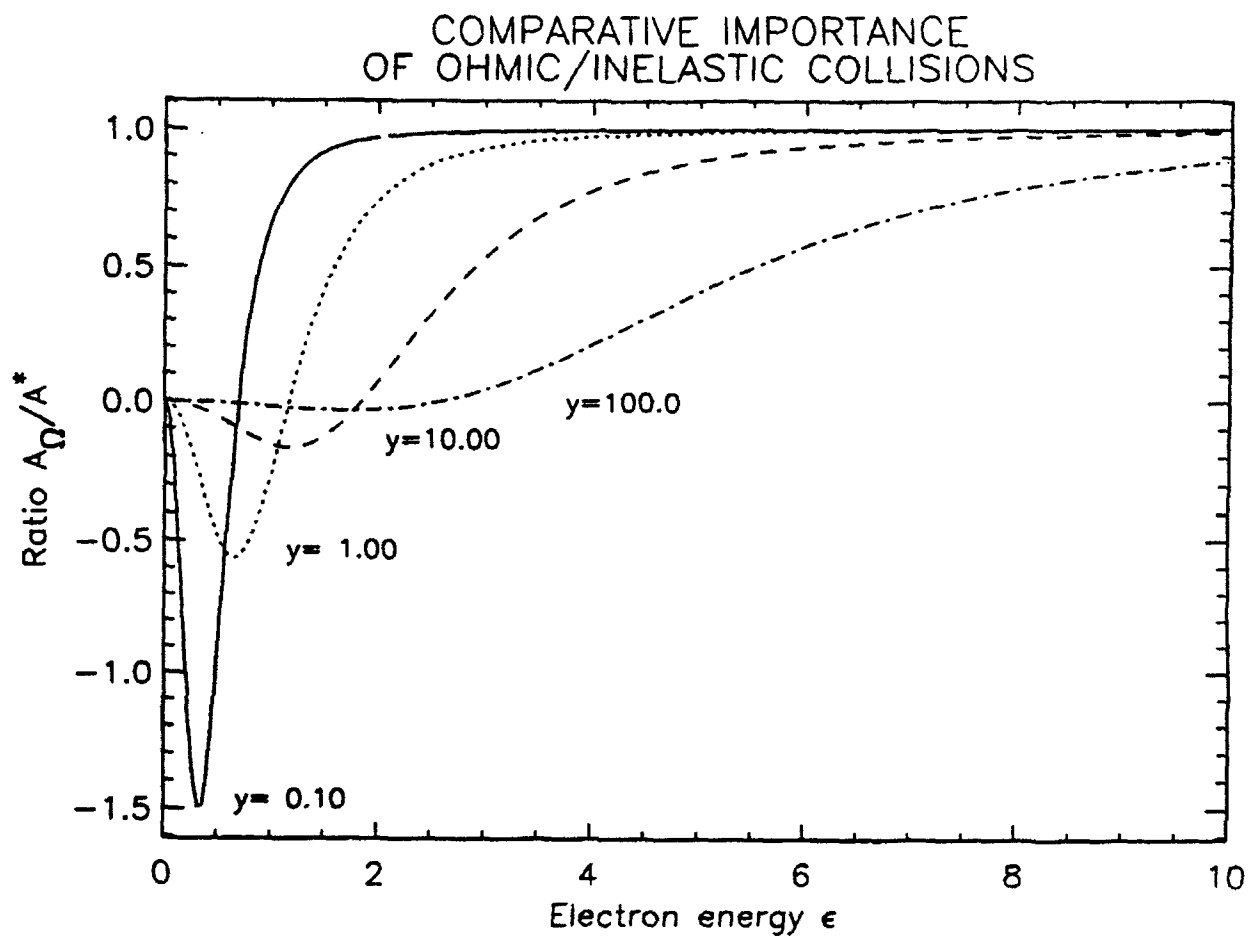


Figure 7

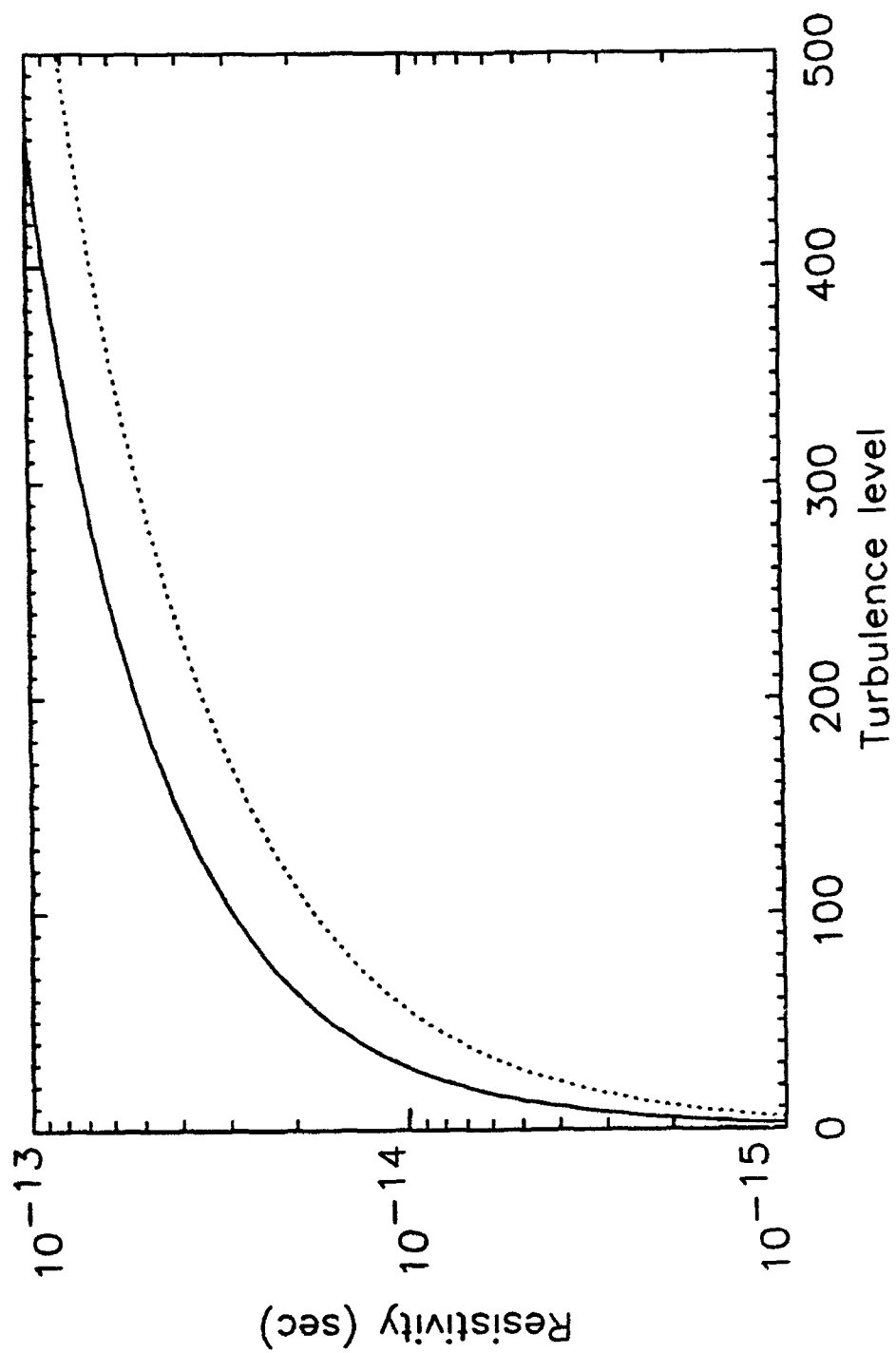


Figure 8

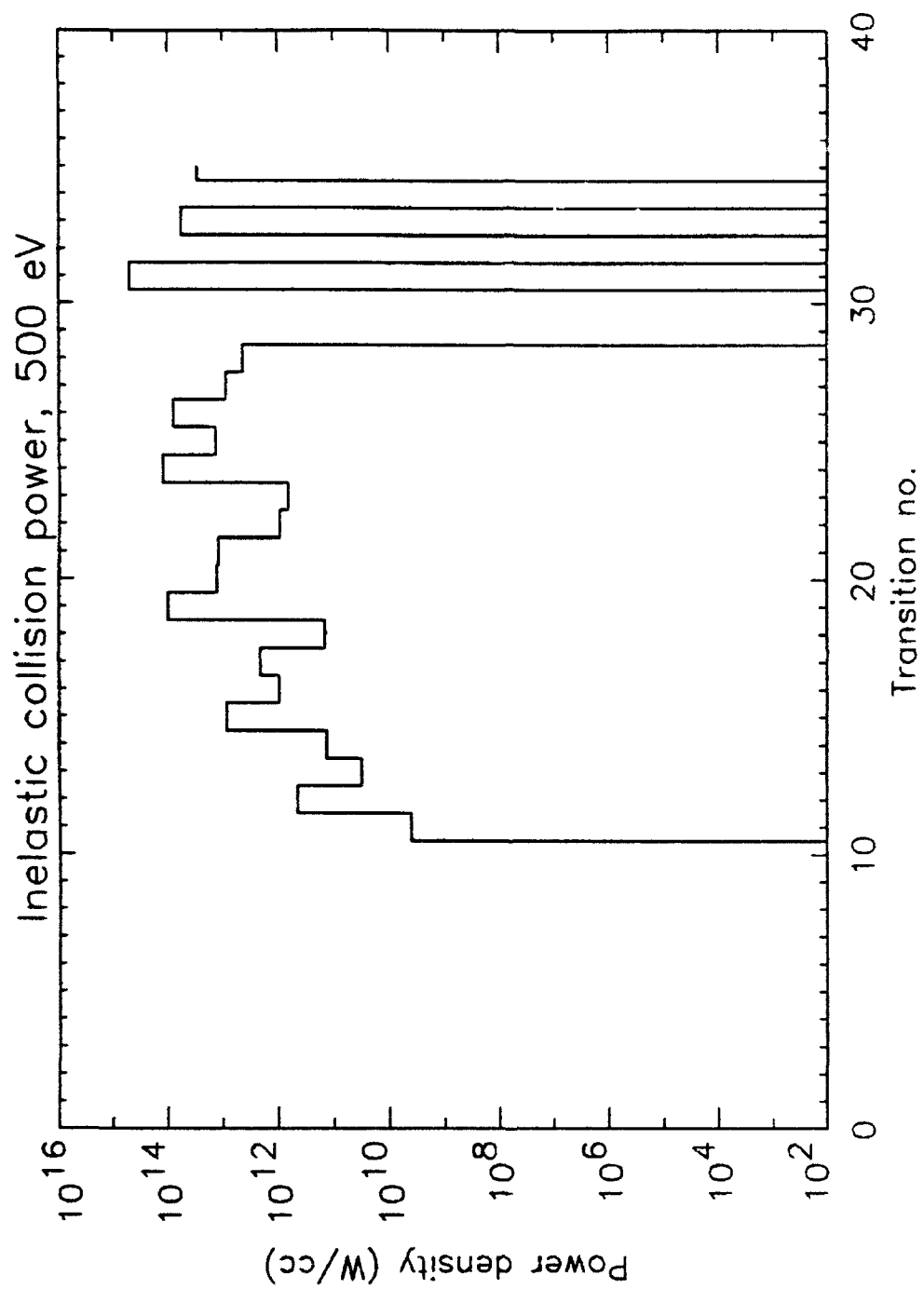


Figure 9

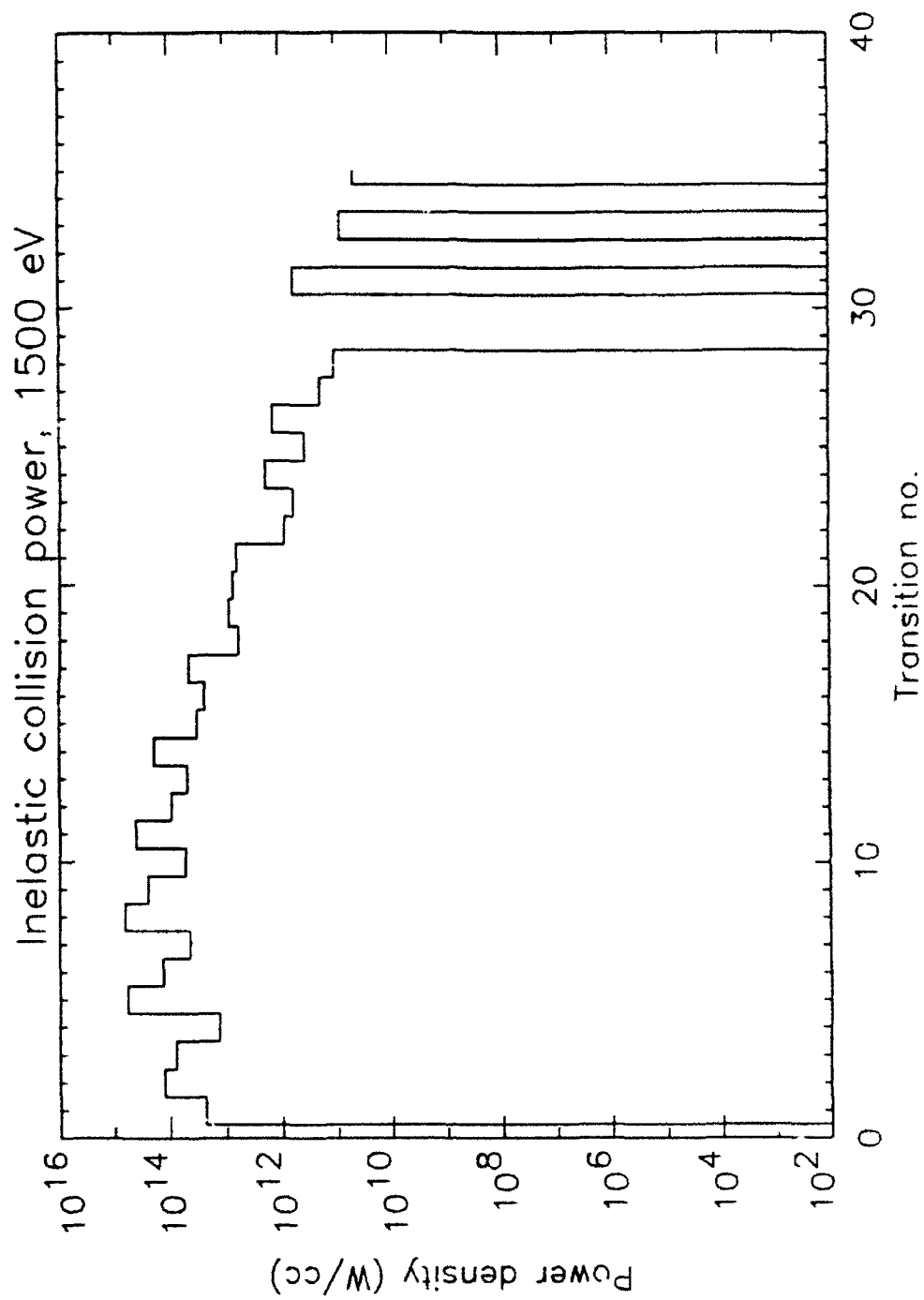


Figure 10

"STD B1 500 OHMIC HT", M=3.3 (MB)

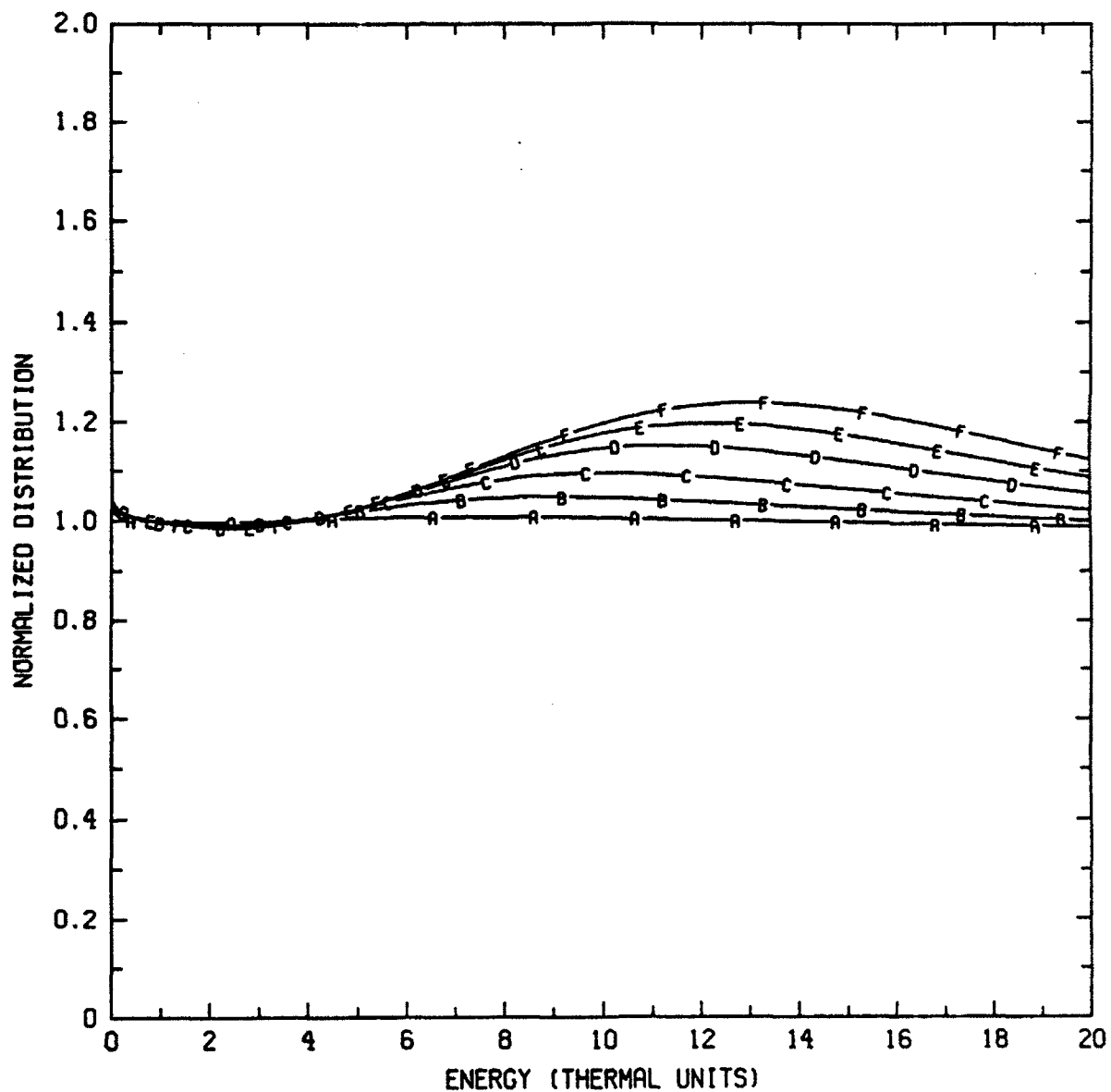


Figure 11

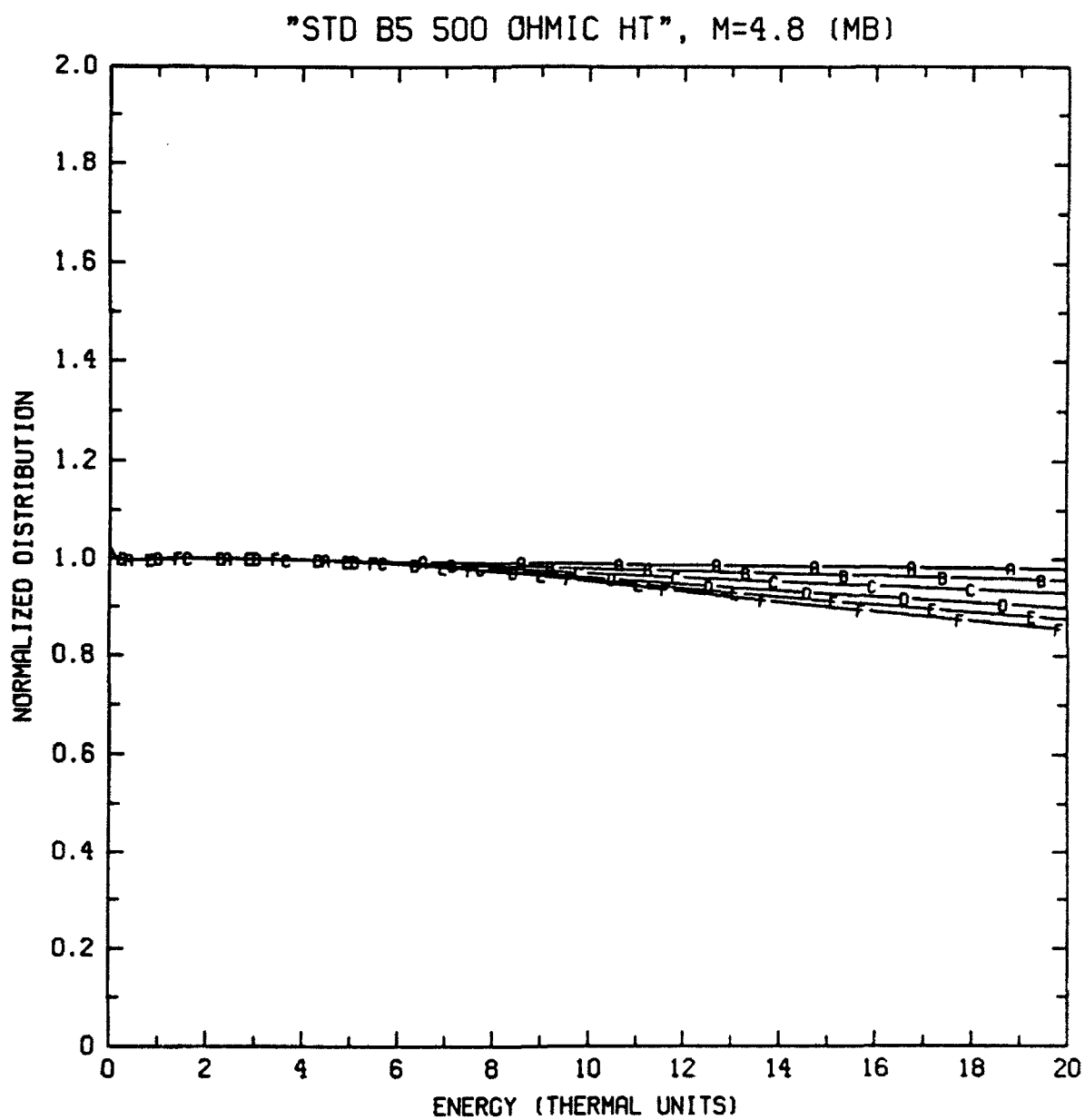


Figure 12

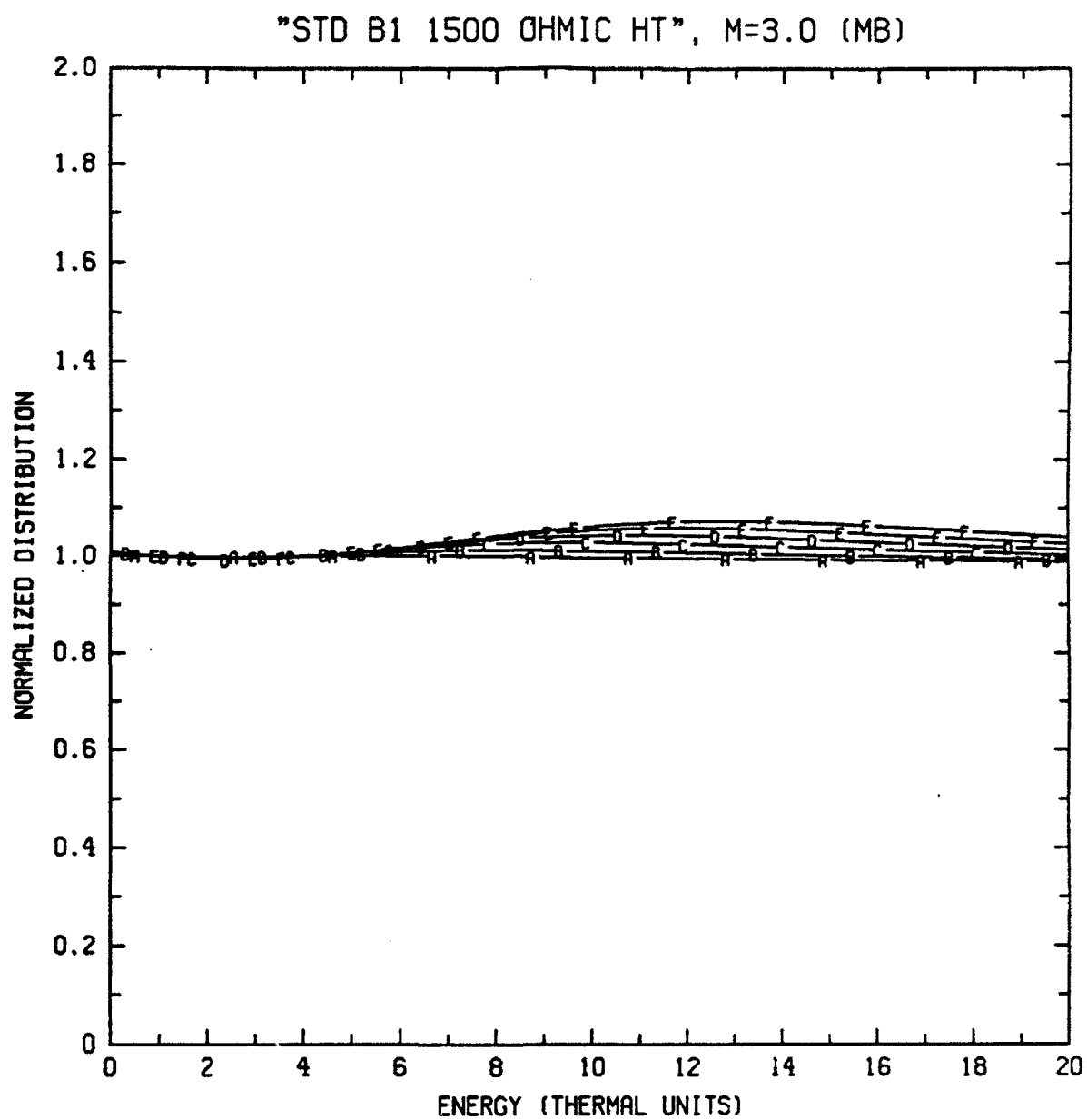


Figure 13



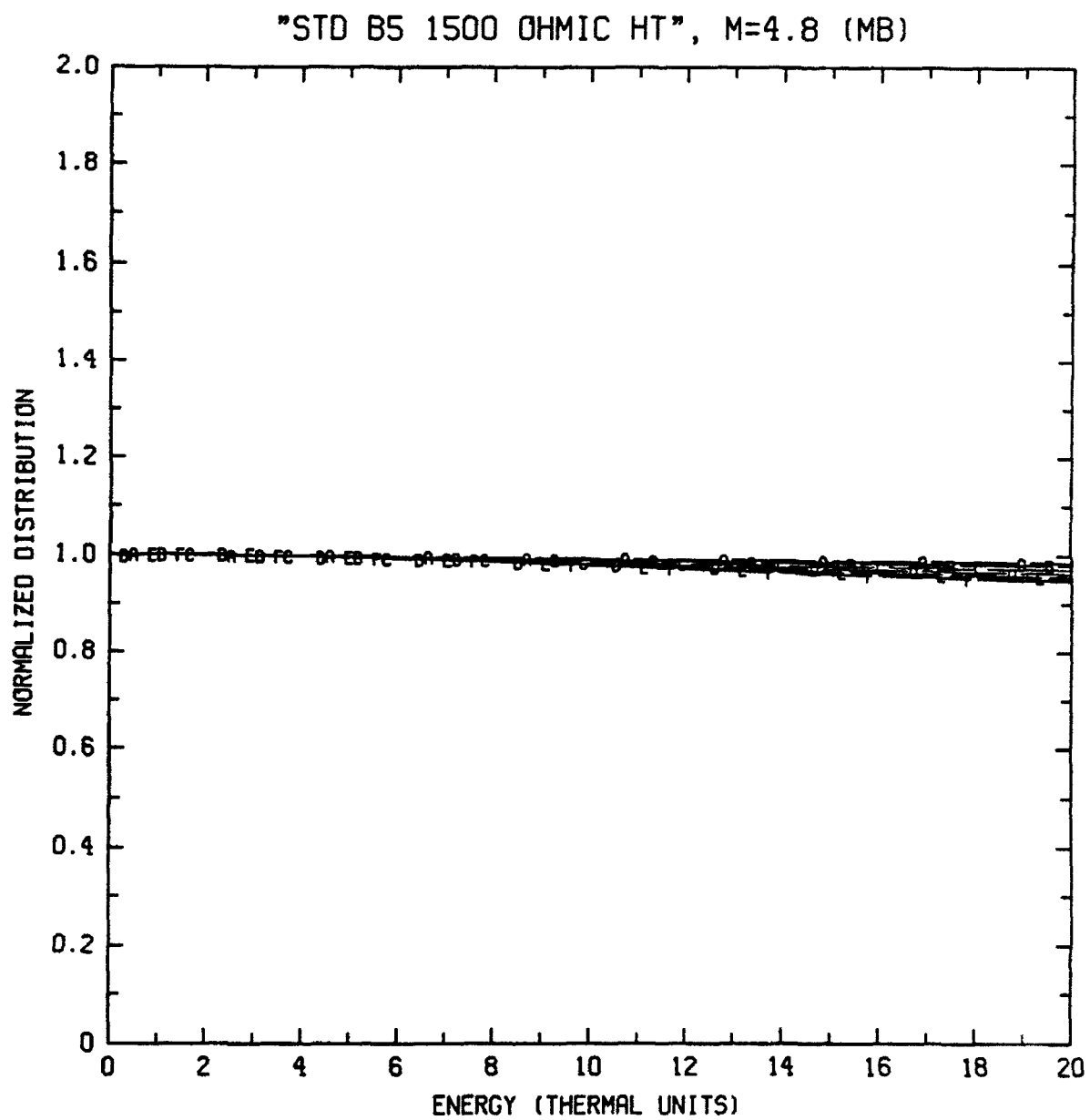


Figure 14

## IV. PRS NOZZLE DESIGN AND GAS PUFF SIMULATION

### (a) PI Simulations and Nozzle Designs

During this past year, considerable effort was concentrated on developing a better understanding of the 2D dynamics of gas puff implosions associated with different nozzle designs. In particular, the role of tilting nozzles inward was examined in order to minimize the so called "zippering" effect in which the implosion first reaches the axis near the nozzle throat and then progresses up the axis. This type of 2-D implosion results in a lower peak power and a longer radiation pulse width than would be expected from a uniform 1-D implosion. However, if the nozzle is tilted inwards, the peak power of K-shell emission is higher and the pulse width is shortened. The density on the central axis at the time of assembly also appears more uniform. It would appear that the total yield would then be approximately independent of tilt angle and that the tilted nozzle design would be desirable purely from the standpoint of higher peak power during the pulse. This is not the case, however. In our simulations, and in experimental results from Physics International, the tilted nozzles also produced higher yields in addition to the higher powers. This is because the final assembly on axis occurs over the full length of the pinch in the tilted nozzles with the result that the *average* density is substantially higher. Evidently the quality of the tilted nozzle implosions, in terms of density uniformity, is such that the resultant large increase in peak power also leads to greater yields despite the fact that the FWHM time of the pulse is shorter.

Nozzle Width (cm)	Yield (kJ) (0 deg. tilt)	Yield (kJ) (-7.5 deg. tilt)	Yield (kJ) (-10 deg. tilt)
0.8	1.4	3.0	4.6
0.4	2.0	3.7	7.1

Table I. Double Eagle Argon K-shell yields from different nozzle designs (50  $\mu\text{gm/cm}$ )

Table I shows the Argon K-shell yield values from six Double Eagle nozzle design simulations. It can be seen that there is about a 4:1 ratio in the argon K-shell yield between the best case (tilted nozzle, 0.4 cm width) to the worst case (untilted nozzle, 0.8 cm width). This is roughly the ratio seen in the PI experiments. The simulation results have shown that for a straight nozzle, the bulk of the radiation comes from the dense region which moves up the z-axis during zippering. In contrast, when the nozzle is tilted the radiative power is spread more uniformly over the plasma volume. In addition, the average bulk density over the entire plasma fill is twice as high in the best yield case versus the worst case ( $1 \times 10^{19} \text{ cm}^{-3}$  versus  $5 \times 10^{18} \text{ cm}^{-3}$  shown in Table I). An explanation for the lower densities in the untilted nozzle designs is as follows. During a "zippering" implosion, the large amount of axial kinetic energy which is generated results in preheated mass being pushed up the axis. As a result, as the implosion progresses the remaining mass implodes onto this hot plasma which limits its compression and final density.

Figures 1 and 2 show density fill plots for the worst case (0.8 cm nozzle width,  $0^\circ$  tilt) and best case (0.4 cm nozzle width,  $-10^\circ$  tilt) nozzles. Figure 1 (a) and Fig. 2 (a) show the initial density profile while Fig. 1 (b) and Fig. 2 (b) show the density near final assembly at the time of peak power. The importance of these results is that in a straight nozzle the radiative output is localized and persists during the so-called "zippering" time. This leads to the relatively broader radiation pulses observed in implosions using these nozzles. In a more uniform implosion, with a mass loading initiated by flow from a tilted nozzle, both higher peak power and higher yields are observed.

Historically, one of the troubling problems in Z-pinch simulations is the fact that the radiation pulse width seen in the simulations tends to be of much higher power and shorter duration than that observed in experiments. Despite this problem, however, there is still very good agreement with K- and L- shell yields. Several explanations have been given for this. These include 2-D effects in which instabilities and non-uniform implosions lead to different times of collapse for different parts of the plasma. Another theory has been that enhanced transport coefficients in the experiment tend to broaden the current and thermal profiles and hence, soften the implosion.

In order to address this issue, a series of simulations was conducted which compared 2-D results, obtained with tilted and untilted nozzles, against 1-D results. For a series of simulations of the PI Double Eagle device over a range of linear mass densities and enhanced resistivities we found that the yields are nearly the same in 2-D calculations as in 1-D calculations but that the width of the radiative power pulse and the value of the peak power can be very different. In fact, for a series of Double Eagle implosions, we found that for three mass densities ( $50 \mu\text{gm/cm}$ ,  $100 \mu\text{gm/cm}$ , and  $150 \mu\text{gm/cm}$ ) the ratio of the 2-D radiative power curve pulse width to the 1-D pulse width was almost the same with a value close to 2.5. A standard straight nozzle (i.e. typical of the design used in the experiment) with a 10 degree gas expansion, and a 3 cm length was used. We then went back and repeated the 1-D calculations but increased the resistivity with a constant multiplier,  $\eta^*$ . We chose  $\eta^*$  factors of 1, 10, and 100. Increasing this value resulted in a broadened pulse width as well as some increase in the yield. When  $\eta^* = 100$  and with the highest mass loading, the 1-D pulse width came to within 85% of the 2-D value. It must be emphasized, however, that the mechanisms for broadening the pulse widths (at least for the case of a straight nozzle) are different in the two cases. The 2-D broadening is due to "zippering" or, motion along the axis, while the broadening in the 1-D simulations is due to a penetrating magnetic field which softens the implosion. Figure 3 summarizes these results in graphical form.

The PI simulation results show the same qualitative trend as the experimental results. However, there was a systematic error in the yields obtained from the simulations as compared with the experiment in that the simulation yields were consistently less than were observed experimentally. There may be several reasons for this. First, these simulations are designed primarily to test hypotheses about implosion uniformity. Since the initial mass distribution formed from a nozzle can fill nearly the entire computational domain, the orthogonal mesh is fixed in time. Hence, resolution for the core plasma is reduced over what could be achieved with a 1-D Lagrangian or Eulerian with a moving mesh calculation. In these simulations, there were approximately 100 radial zones. Therefore, at the final point of assembly, the resolution in the K-shell emitting zones is reduced to just a few zones. This necessarily reduces the peak density which can be achieved and could lead to a

systematic error. A second possibility is that the pulse width for the experiment is still much larger than those which are seen in the simulations. The experimental widths are approximately double that of the simulations although the trend of shorter pulses in tilted vs. untilted nozzles holds. It appears that there are still other physical processes, besides 2-D effects, which will have to be invoked to explain the broader pulses. This is an ongoing and important topic for future research. Despite these problems, it can be said that the modeling has resulted in good agreement with the PI experiments since: (a) the ratio of the yield of untilted and tilted nozzles was nearly the same (4:1 from best case to worst case) and; (b) the trend in the reduction of pulse widths is the same in the simulations as in the experiment. The model also confirms the experimental hypothesis that jetting occurs along the axis during a "zippered implosion". These results have been compiled into a paper which has been accepted for publication in *Physics of Fluids* (to appear in the March, 1993 issue).

#### **(b) Saturn Simulations**

With the success of the interaction with PI and the qualitative agreement between simulation and experiment, it was felt that the 2-D code was sufficiently benchmarked and could be used to look at implosion problems on other pulse power machines. The goal has been to advance the simulation capability through benchmarking with existing machines while at the same time contributing to the understanding and improvement of ongoing experiments.

With this in mind, our next step was to examine gas puff implosion dynamics on the Sandia National Laboratory Saturn pulse power device. This was a particularly advantageous choice because the nozzle design used in Saturn experiments was similar to that used in the Double Eagle experiments.

In these simulations, we used a circuit model to drive the implosion. This model consisted of the characteristic voltage waveform of the SATURN generator coupled to a circuit which consisted of a machine inductance of 9.75 nh, 0.17 ohms of machine resistance, and return current bars set so that the initial load inductance is 2.5 nh. The simulated gas puffs were argon.

A modified "thin" radiation lookup table routine was used for both equation

of state properties and radiation power. A "thin" radiation model implies that all radiation energy is immediately lost from the emitting computational zone of the plasma and is not absorbed in other parts of the pinch plasma. In the initial phase of performing these simulations, for lack of opacity, it was found that an overly large amount of radiated power was coming out in the L-shell. In an attempt to correct this problem, a scheme was developed for modeling the effective opacity within each computational zone. This allows us to continue to use the lookup tables but requires an additional parameter when making the table, namely the effective length over which to calculate the optical depth. Once the length is chosen, the effect of opacity within each individual zone and for each table entry is calculated with lowered the Einstein A's obtained by dividing by the optical depth (i.e.,  $\bar{A} = A/\tau$ ). Several tests showed that this can dramatically effect the L-shell line radiation by decreasing it by factors of two or more. However, the K-shell is relatively unaffected. We now feel that this "local" approximation allows us to more accurately model 2-D Z-pinch implosions. In addition to radiative power, the equation-of-state lookup tables include internal energy and density based values for electron temperature and charge state. These values are then used to determine the electron pressure.

Two sets of Saturn argon simulations were conducted with the 2-D code PRISM. The first set of simulations were conducted by changing the nozzle design and adding progressively more tilt angle. We used the PI nozzle design that has been discussed in the previous section (0.4 cm nozzle width) except that the diode length was taken to be 2 cm. The tilt angles covered a range from 0° to -12.5°. This series of simulations thus covered designs from straight nozzles to nozzles which slightly overcompensate for the 10° expansion of the puff gas as it exits the nozzle throat. A mass loading of 450  $\mu\text{gm}/\text{cm}$  was chosen, since as discussed below (see Table III), this is near the mass for which Saturn achieves the maximum K-shell yield. The results are not expected to change dramatically with differing mass loadings.

The results of this series is shown in Table II. It can be seen that the peak power increases by a factor of two from the 0° to the -10° case. The FWHM (i.e., the length of time to rise from one half peak to peak and then fall again to one half peak) also falls by a factor of two. In terms of these two measures, the tilted

nozzle design is obviously superior to those of the untilted nozzle. The power and pulse width values in Table II also show that even 5° of tilt substantially improves the implosion quality as evidenced by the higher power and shorter pulse width. However, the K-shell yield is roughly 30% higher for the tilted case. This is below the yield improvement seen in the simulations of the PI Double Eagle device discussed above. One conjecture for this discrepancy between the two sets of simulations is the different nature of the two machines. Due to the low machine inductance of Saturn, the current peaks well before the time of implosion. Therefore, the plasma is not so much driven into the final assembly by the magnetic field pressure but rather implodes under its own inertia. These implosions are sometimes referred to as "kinetic energy" implosions. Double Eagle, by contrast, has a higher inductance and the current peaks very close to the time of final assembly. In this case the zippering motion can be driven with much higher gradients. Consequently, the emitting region can be more localized. The result, for Double Eagle, is that there is not a simple tradeoff between peak power and pulse width. With Saturn, the simulation results indicate that this one-for-one tradeoff may be closer to what is seen in the 0° and the -10° results in Table II. This is a topic which needs to be investigated further in the future in order to understand its importance in DECADE and future machines.

<b>Tilt Angle (degrees)</b>	<b>Power (TW)</b>	<b>Yield (kJ)</b>	<b>FWHM (nsec)</b>
0	1.7	27	13.5
-5	3.1	31	7
-7.5	3.2	31	6
-10	3.6	33	6
-12.5	3.5	35	5

**Table II. Saturn Argon K-shell yields as a function of nozzle tilt angle (450  $\mu\text{gm/cm}$ )**

Figure 4 shows the current, input generator voltage, and radiative power for the straight nozzle case. The same quantities are shown in Fig. 5 for the case with

$-10^\circ$  nozzle tilt. In both figures it can be seen that the motional impedance of the inwardly moving plasma causes the current to roll over at about 70 nsec. The result is that the peak current is between 8 MA and 9 MA. However, the most dramatic difference between the two figures are seen in the radiative power curves. In the tilted case, the curve is symmetric with a higher peak power (roughly 3.6 TW). The radiative power curve in the untilted case, in contrast, is not as symmetric, broader at its FWHM, and has slightly less than one half of the peak power of the tilted nozzle.

In addition to the tilted nozzle series discussed above, a series of simulations were conducted with the  $-10^\circ$  nozzle design and various mass loadings. In the discussion above, it was seen that the peak power, at the expense of a shortened FWHM, dramatically increases when a tilt angle is used to counteract the expansion of the puff gas as it exits the nozzle. Here, we detail the yield with mass relationship for the tilted nozzles. The results obtained using a 1.25 cm radius nozzle with a 0.4 cm exit width and a  $10^\circ$  inward tilt are given in the table below. Again, the length of the puff along the axis was taken to be 2 cm.

When these simulations were made with different values of enhanced resistivity, we found that K-shell yield remained fairly uniform but the total yield increased (i.e., K-shell plus L-shell) substantially. Since the experimental results have indicated that there is much more L-shell radiation than is typically seen in the simulations, we chose to use an enhanced resistivity for these runs. Evidently, a large fraction of this L-shell radiation must come from resistive heating.

Mass ( $10^{-6}$ gm/cm)	K-shell Yield (kJ)	Total Yield (kJ)
300	22	122
400	32	139
450	33	148
600	31	154

**Table III. Saturn Argon K-shell yields as a function of mass for  $-10^\circ$  tilt nozzles**



Additional post-processing was done using the complete atomic physics package and thin radiation model (as opposed to the table lookup used during the simulation) at selected times during the radiative power pulse using values dumped during the simulation. This typically requires about 10 post-processing runs, based on one dump per nsec, per mass load. This was done as an exercise to determine the accuracy of using the table lookup scheme which is must less expensive, computationally speaking, than using the full atomic physics package. For the 450  $\mu\text{gm}/\text{cm}$  simulation, this method gave a K-shell yield of 35 KJ which is very close to the 33 KJ obtained from the lookup values. This has added confidence that the table lookup method is validated.

### (c) Summary

In summary, when the zippering effect is eliminated in argon gas puff implosions by using a tilted nozzle design, the K-shell power can be significantly increased. The K-shell yield is also increased although this effect is more dramatic in the PI Double Eagle device than on the SNL Saturn device. This appears to be due to the fact that the plasma which participates in the K-shell radiation is more efficiently imploded in the tilted nozzle designs and reaches higher densities.

The use of tilted nozzles in the upcoming DNA devices (i.e., DECADE and follow on machines) should provide for more optimized implosions. Further experimentation on present devices (Double Eagle and Saturn) and 2-D simulations of nozzle designs will provide a path for achieving these optimized implosions.

In the future there are several areas which should be explored with the 2-D PRISM code. First, the discrepancy in the enhancement seen in the Double Eagle experiments and simulations versus the Saturn simulations is still not fully understood although, there are plausible explanations. It is important that this issue be resolved because the two devices have different current driver characteristics and this is an important design issue for PRS experiments on future machines. Second, we have used a generic nozzle design in these studies. There are other parameters of the nozzle flow which may be important including, but not limited to, the profile in the cross-section of the gas. The ultimate study will be to initialize the code with results input directly from a nozzle design code. We have had informal

preliminary conversations with C. Deeney at P.I. about doing this. Finally, this work represents a benchmarking of the code through close interaction with experiments at P.I. The goal in the upcoming year will be to examine optimum PRS designs for DECADE and follow-on pulse power machines.

### Figure Captions

**Figure 1.** Density fill plots showing the initial profile (a) and the profile at assembly (b) for an argon gas puff implosion. Untilted nozzle design.

**Figure 2.** Same as Fig. 1 but for an implosion initiated with a  $-10^\circ$  tilted nozzle.

**Figure 3.** Radiation pulse width as a function of linear mass density for 2-D nozzle implosions and 1-D implosions with different multipliers on Spitzer resistivity.

**Figure 4.** Current, input generator voltage, and radiative K-shell power for a Saturn simulation. This argon implosion was initiated with an untitled nozzle.

**Figure 5.** Same as Fig. 4 but for an implosion initiated with a  $-10^\circ$  tilted nozzle.

Nozzle: 2.5 cm diam., 0.4 cm width, 0° tilt  
Initial Profile

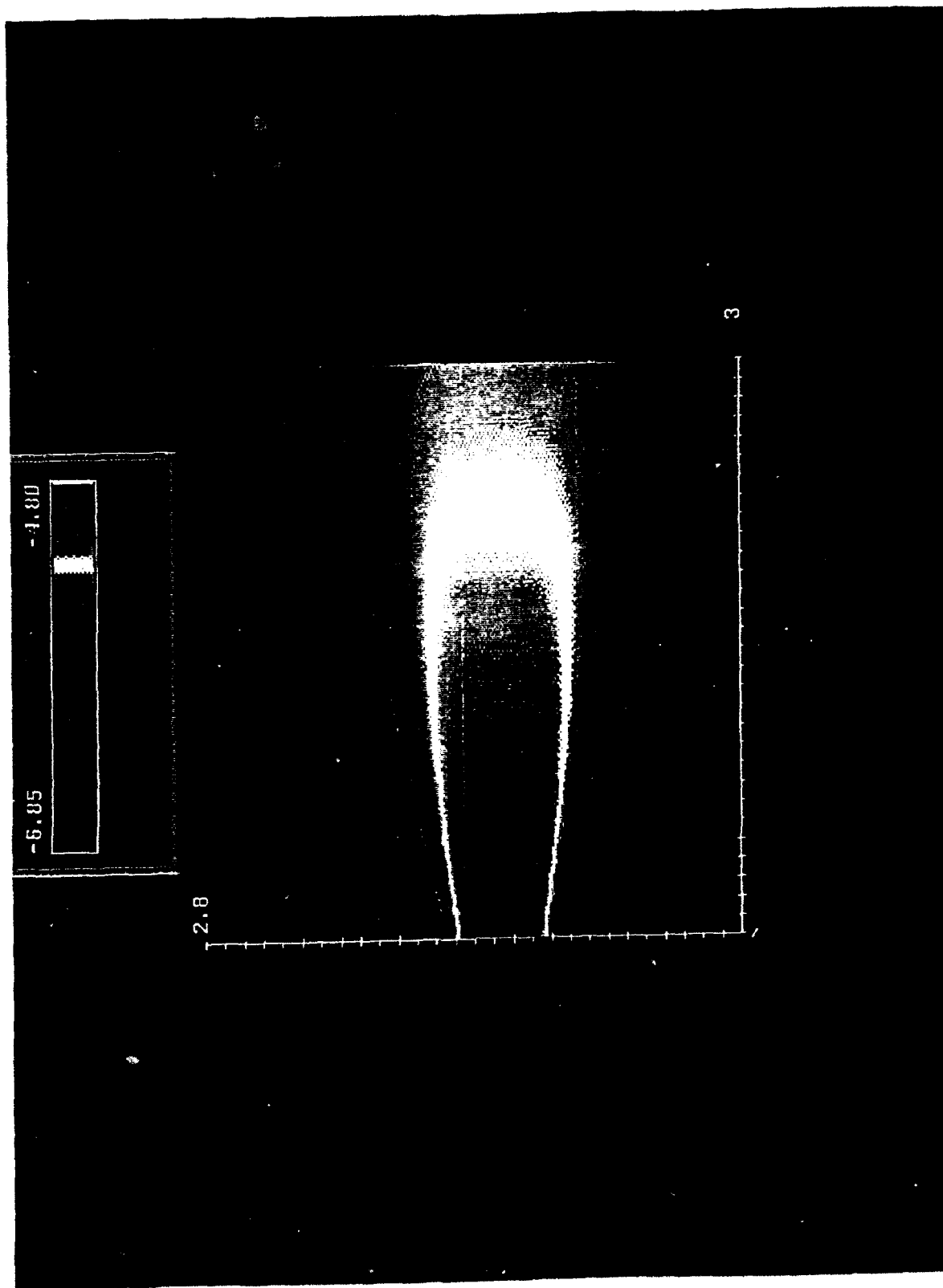


Figure 1. (a)

Nozzle: 2.5 cm diam., 0.4 cm width, 0° tilt  
110 nsec

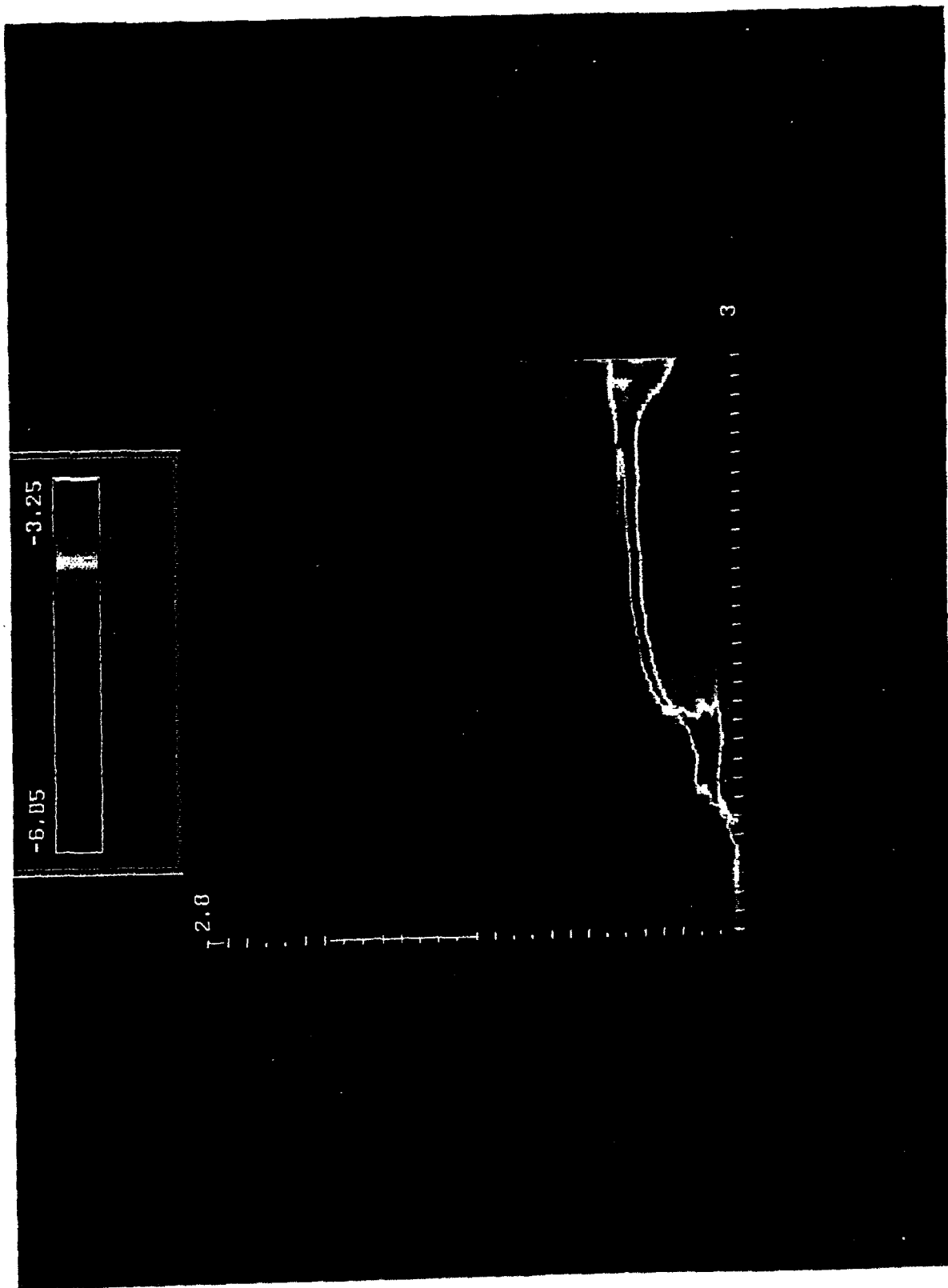


Figure 1. (b)

Nozzle: 2.5 cm diam., 0.4 cm width,  $-10^\circ$  tilt  
Initial Profile

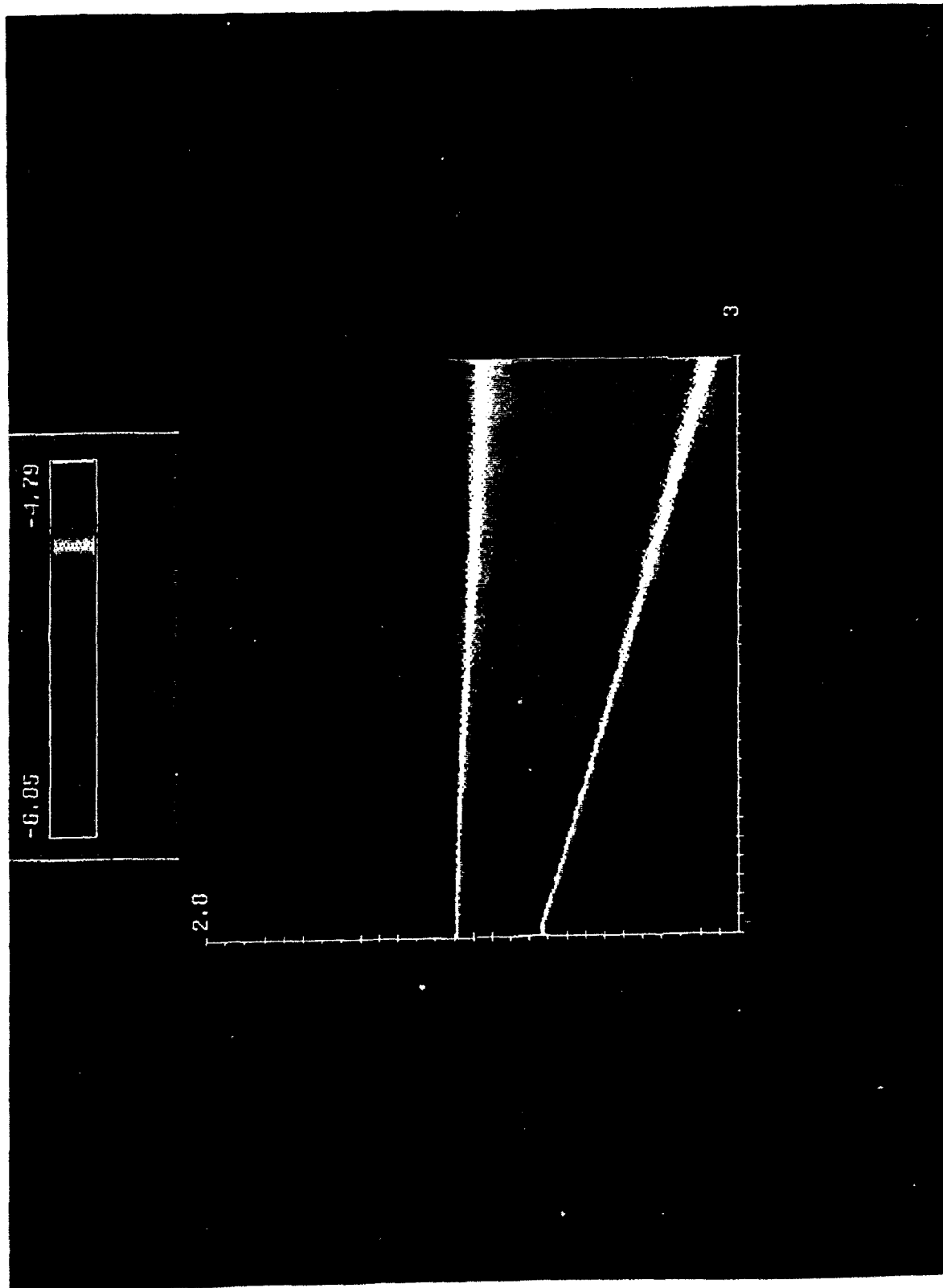


Figure 2. (a)

Nozzle: 2.5 cm diam., 0.4 cm width,  $-10^\circ$  tilt  
100 nsec

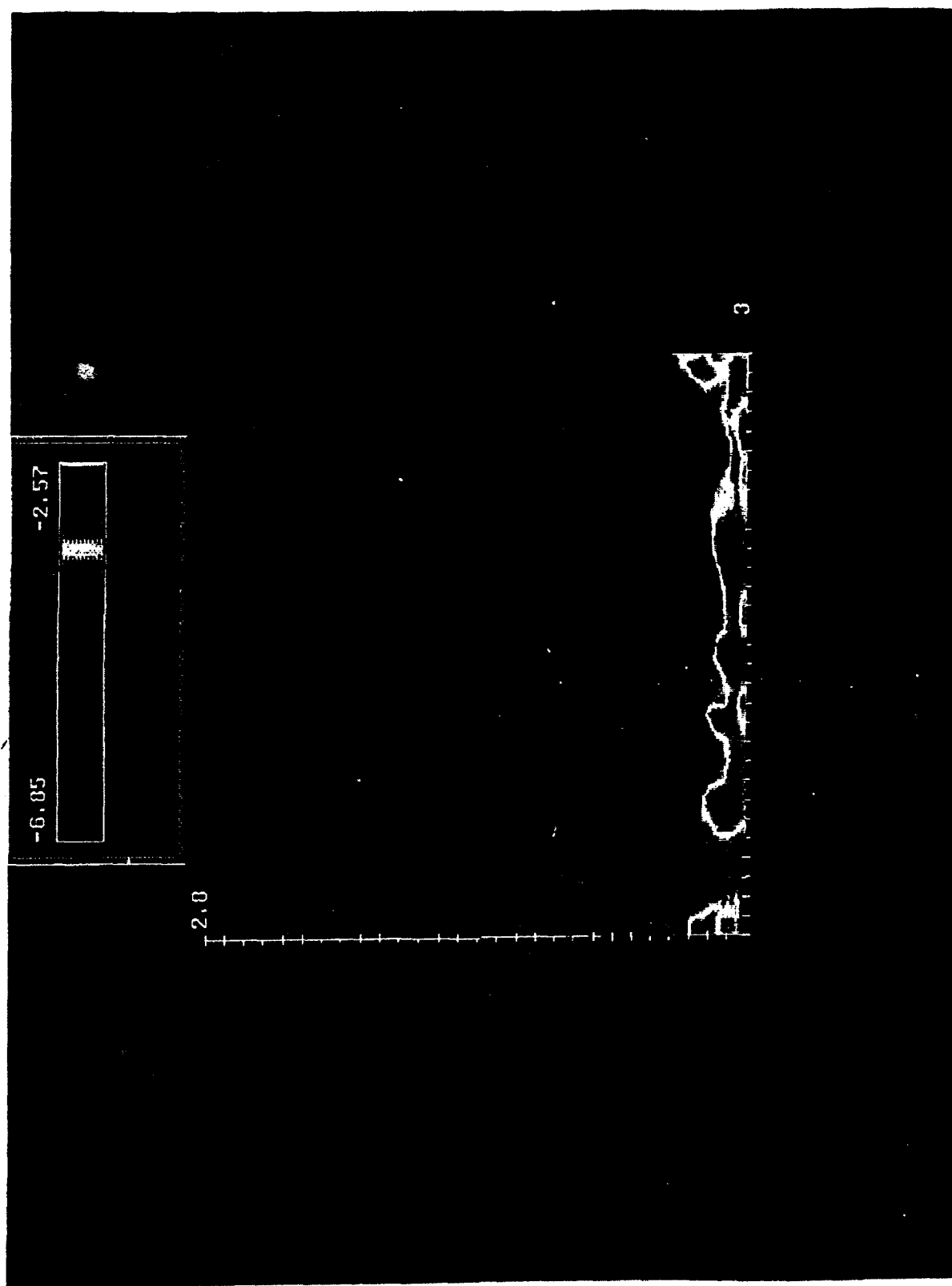


Figure 2. (b)

# Radiation Pulse Width as a Function of Mass

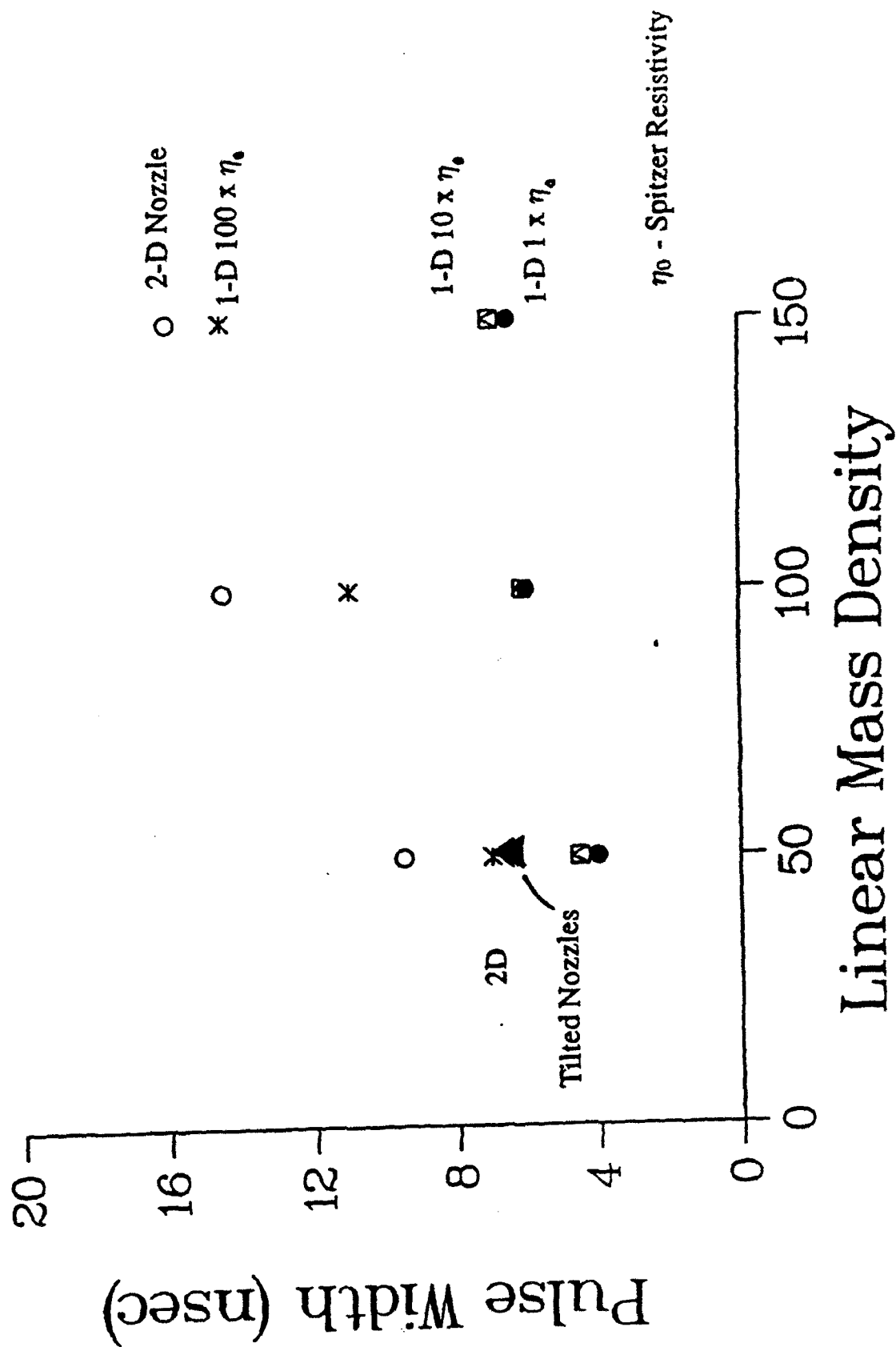


Figure 3.



# Saturn Implosion 0° Tilt

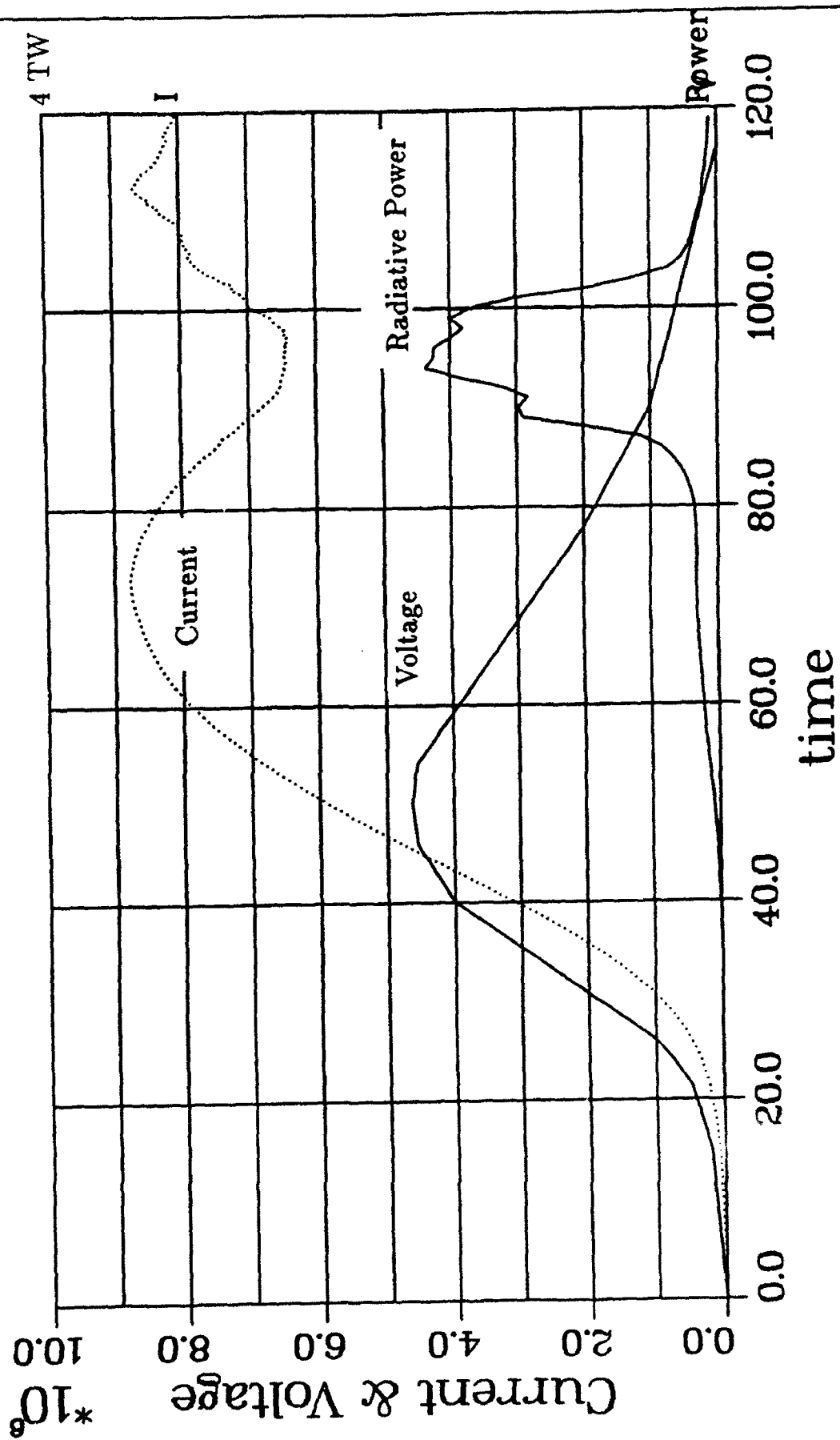


Figure 4.

# Saturn Implosion -10° Tilt

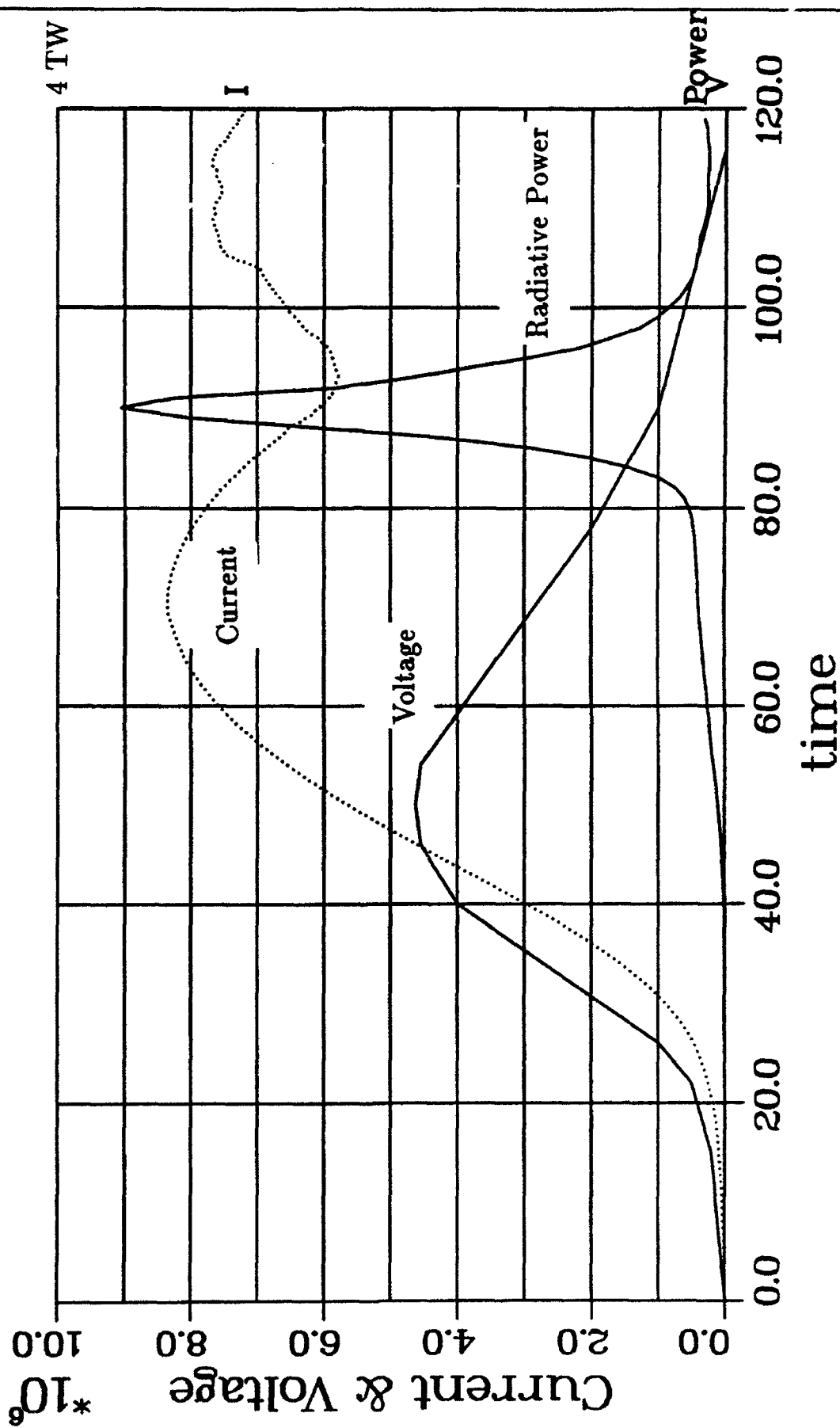


Figure 5.

## **V. Coupling PRS Loads to DECADE Class, Long Conduction Time POS Inductive Generators**

### **I. Introduction**

The introduction of inductive energy stores (IES) to pulse power driven Plasma Radiation Sources (PRS) has made possible an order of magnitude or so reduction in the total size of the pulser modules and a potentially significant decrease in the risetime of the output current pulses. The risetime decrease would make available the added option of smaller radial implosions in PRS load designs. NRL is involved in a specific effort to understand power flow to the PRS load in an IES machine in support of the DNA DECADE simulator. As part of that program we are developing a transmission line model that resolves the Plasma Opening Switch (POS) module into a series of shunts in the transmission line and determines the electrical properties of those shunts from four basic theoretical models (described in II., below). This work is intended to provide first a simplified but comprehensive model to study power flow to any PRS operating in an inductive generator environment, and later some scaling guidance for the design of PRS loads in DECADE. In particular, useful design guidance will require an understanding of several issues, such as: the low overall system efficiency, the possibility of POS restrike and other MITL losses, and the expected peak voltage at PRS implosion.

These issues are in fact fundamental to IES/PRS systems and essentially unavoidable. The operation of the POS, an essential IES element, tends to lower the general efficiency of the pulser. The fraction of initial stored energy delivered to the load can be low ( $\approx 5\%$ ), if only due to the basic energy transfer constraints associated with inductive store systems. The interaction between a POS and its load depends upon the time development of the load impedance. The efficiency of a PRS implosion depends upon the quality of power flow to the immediate vicinity of the pinch. Therefore, a primary question is: how can we make the best trade-off between the high voltages developed at PRS implosion and the amount of front end inductance that controls the probability of restrike in the POS? If restrike occurs, it could curtail needed power flow to the PRS. If one can speak of a single "coupling problem" as such, it is this PRS voltage/front end impedance trade-off. The experience to date would imply that, as the present switch and load designs are scaled to DECADE, neither the PRS nor the POS can be optimally designed in ignorance of one another.

We have been quite successful previously in using simple transmission line and PRS descriptions for modeling the power flow to PRS loads in capacitively driven pulse power machines, and in investigating the consequences of various load and machine parameters on PRS performance. Early IES investigations involved the use of phenomenological lumped circuit modules to mock up the POS – typically as a time dependent resistance with a conduction delay. The work presented here constitutes a natural extension of these previous studies, but different in that it proposes several new theoretical descriptions for the recent observations in the long conduction time POS experiments done on Hawk at NRL. The scope of this summary is a description of the POS model, its benchmark with the Hawk experiments, and some preliminary observations on power flow and POS/PRS interactions.

## II. Structure and Performance of the POS Model

While motivated by the need to carry out PRS load design calculations for DECADE that encompass all the relevant power flow issues, the new theory initiatives to be set forth are rooted both in recent observations from the Hawk POS device and in some weaknesses of early theoretical models in treating: (i) the progression of current during the POS conduction phase, and (ii) the cathode sheath. In some early work the (apparently linear) progression in time of the current channel along the cathode could be described as a process of matching the switch current to the injected current, and opening was viewed as a consequence of running out of new area for conduction, which forced ion current to be drawn. This increased ion flow would erode the plasma ions to open a channel. In this picture the local cathode area and plasma density set an upper limit to the current, no matter what the timescale for charging the storage inductor. However, the width of the observed current channel seemed to argue for a turbulent diffusion process.

A linear current progression is inconsistent with respect to both observation and theory. Magnetic probes generally show a very broad current channel, and even given recent observations limiting the spatial resolution of the probes, any apparent turbulent diffusion indicated by the wide current front should provide a current progression into the switch with a speed determined by the physics of the anomalous transport processes. If such a diffusion picture is accurate, then there is every reason to expect a nonlinear progression of the current channel through the switch. No basis for the very special case of a linear progression has been established. Moreover, a good deal of evidence to date

suggests that the actual progress of the current channel is not linear, at least at higher conduction currents. It is certainly possible therefore that the switch is not a "current limited" device at all. Certainly in the long conduction time, high current limit, the nonlinear scaling of conduction time and peak current is potentially describable by a variety of snowplow style models. The Hawk observations demonstrate clearly that bulk plasma motion and number density depletion are crucial processes in the long conduction time POS.

A second weakness in earlier models was the treatment of magnetic insulation in the cathode sheath as it progressed along the switch. The use of an unmagnetized bipolar Child-Langmuir current density over the whole "active" portion of the cathode is inaccurate and ignores the important modifications to the gap space charge density arising in a magnetized sheath. As shown below, only an extraordinary enhancement of electron space charge can draw enough ions from the anode surface of the sheath to produce a significant level of erosion, and only a complete description of the ion emission process that includes a presheath model can establish whether or not erosion can occur. The issue must be addressed by a model sufficiently complete to account for the evolution of electron space charge over the whole length of any gap or depletion channel that arises. Unfortunately the gap and emission surface structures in the long conduction POS are not well known – the "physical gap" (inferred from density depletion) is quite a bit larger than the "electrical gap" (inferred from magnetic insulation conditions). Some model accounting for the buildup of electron space charge in a semi-collisional gap is needed, either to justify or to ignore the idea of erosion.

#### New POS Theory Elements

In addition to the motivating weaknesses just noted there are as well some motivating observations that argue for a fresh model and arise from the Hawk experiment. The principal innovation in Hawk is the observation of the axially integrated electron line density over the entire conduction and opening phase at various radial locations. That line density decays with time over a gap about 1 cm wide, referred to here as a "depletion channel". If the peak current prior to opening is denoted  $I_{cond}$ , one finds that:

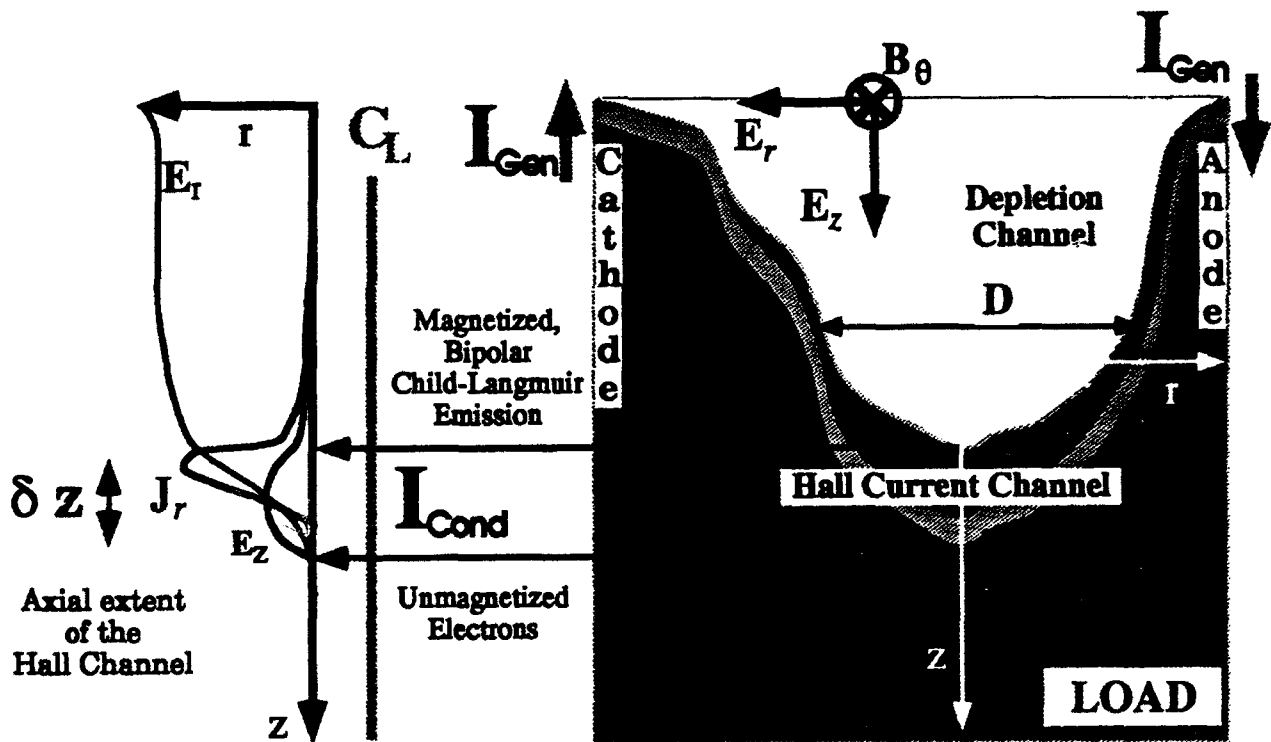
[ i.] A steady drop in line density precedes the opening event .

[ ii.]  $I_{cond}$  scales sublinearly with density,  $\propto n^{0.25}$ .

[iii.] The observed physical width  $D$  of the depletion channel is larger than the mm size electrical width inferred from the opening data.

A model that seeks to capture these observations quantitatively requires several characteristic structures and some rules governing the relationships among them. The basic conception of such a model, for a coaxial POS, is shown in Fig. 1.

**Fig. 1 Conduction Phase POS Structures**



With physical structures shown to the right of the center line, and field profiles schematized to the left, the POS is pictured here in the conduction phase. Generator current circulates from anode to cathode through a Hall current channel that is compressing the switch plasma and propagating

toward the load. In the depletion channel (shown just upstream) one expects a partially magnetically insulated Child-Langmuir shunting current to develop, but the primary conduction current is in the Hall channel. The axial extent of the Hall channel is determined primarily by turbulent diffusion processes scattering the electron flow emitted from the upstream cathode (interior electrode). The shunting conduction current determines the line voltage by attenuating the radial electric field of the coaxial TEM mode.

The POS description summarized below requires four theoretical developments to build, from the concept above, a mathematical model that is free of the problems already mentioned, and is also readily extendable to deal with more subtle issues later. This model is comprised of (i) a shunted transmission line picture of the POS electrodynamics, (ii) a Hall channel snowplow picture of current penetration into the POS, (iii) a warm, magnetized emission theory to describe the magnetic insulation of the depletion channel, and (iv) an explosive loss of force equilibrium to initiate the opening.

#### Transmission Line Representation

The normally complex 2-D electrodynamics present in a POS can be approximated by the evolution of a TEM mode in a shunted transmission line. The shunted transmission line description is possible because one can simplify the electrodynamic description by employing axial electric field modes which allow a self-similar response of the POS plasma to the stress imposed by the generator. The physical character of the transmission line in the POS region is determined by the effective gap width  $D$  and the effective cathode radius  $r_c$ , which may be located several mm into the physical gap as the conduction phase develops. The absorbed TEM mode propagates down this line, defined by the low density annular "depletion channel" region just upstream of the Hall current channel. As the field energy propagates into the denser plasma of the Hall channel, it develops a longitudinal component,  $E_z$ , viz.

$$\mathbf{E} = \hat{r}E_r^{TEM} + \hat{z}E_z^I$$

which can be strong enough to support whatever radial Hall shunt current ( $\propto E_z B_\theta^{-1}$ ) is required by the difference in line currents that enter and leave any annular slice of switch plasma in the Hall channel.

The axial self-similarity of the plasma response, over such an annular slice containing the radial Hall current, is possible because the radial structure of the axial electric field conforms to a particular set of TM boundary conditions. It is not obvious that such a mode set should exist, but it turns out that any POS bulk plasma density profile has a compatible radial profile for the axial electric field which admits this decomposition. The radial Hall current density  $J_r$  can then be described by a self-similar form which varies only in  $z$ , viz.  $ren_e(r, z, t) \frac{E_z \times B_\theta}{B_\theta^2} = J_r(z, t)$ .

#### Current Penetration: Conduction $\Rightarrow$ Kinematics

Conversely, when (i) the axial current difference is taken to be the Hall shunt current needed to maintain current conservation and (ii) an axial extent for the Hall channel is fixed by an appropriate turbulent diffusion length, then the local axial electric field can be uniquely determined over the entire length of the switch plasma. But now the electrodynamics determines the kinematics of the Hall channel and the length of the conduction phase is determined by the time required for this snow-plow like Hall channel disturbance to propagate the length of the switch plasma and then push through the rear or downstream surface to open the circuit. In this process the ion number density is compressed axially but is lost radially, and therefore the conduction phase model only tracks the axial compression until an initial cell size is squeezed to a fixed small fraction of its original size.

Is the POS then a current limited device? In this hydrodynamic limit it would not show any intrinsic upper limit to  $I_{cond}$ . If this conduction mechanism is excited, the plasma can accept an essentially arbitrary amount of current into such a "Hall channel" by means of progressively smaller charge separations at progressively higher bulk plasma densities. The net effective stress on the ion plasma component can be calculated from (i) a partial force balance on the electron plasma component and (ii) a fixed amount of radial shunt current generated per unit axial length. The current that can be carried by this process is as large as ever needed for the theory of present or future POS devices. The scale size for the current solution is given by  $60.359 [r_c^2 n_{o,i} / 10^{15}] [Z/2]$  MA. In practice, since the typical POS ion density  $n_{o,i}$  is on the order of  $10^{15}$  and the charge state  $Z$  is of order one, this normalizing current is about 60 MA. Since very small fractions of this current are encountered in real POS devices, the resulting fractional charge separations in the Hall channel are very small.



### Magnetized Emission: Gap Equilibria $\Rightarrow$ Erosion Constraints

The required magnetized emission picture considers the dynamics of "free" electrons, viz. those having a mean free path on the order of or greater than the gap size. Unlike the vacuum MITL problem, the effective emission surface in the POS depletion region is not a dense, highly conductive electrode plasma, but rather a diffuse plasma cloud with a sharp radial density gradient. Electron emission can be space charge limited in the depletion region, but the characteristic length for the decay of any net charge is of the order of a few Debye lengths, or more, up to the plasma skin depth (if the conducting layer is microturbulent or exhibits neutral scattering). Under these conditions a detached electron current would not be expected, and the emitted population of electrons can only exhibit a few relevant orbit classes that contribute to an equilibrium flow in the ambient magnetic field of the depletion region. In a steady Vlasov limit, there must exist a detailed balance between electrons entering a volume element on the "cathode" surface along a given trajectory, those leaving the surface along that trajectory, and those electrons resident on the surface, establishing the local space charge. The radial TEM mode electric field at the surface then establishes a local charge density and its radial integral defines the voltage across the line. The fraction of the electron population surviving to enter the "anode" surface, rather than propagate axially, then determines the local shunt current allowed in the space charge limited gap.

Using this model, one may calculate the impedance of a POS gap in the depletion region accurately over the whole of DECADE relevant parameter regimes. One output of the emission model is a rule for the space charge limited shunt impedance to be used at any point in a depletion channel or sheath when it is partially or heavily magnetically insulated. It turns out that the gap impedance, relative to the usual Child-Langmuir impedance, can be roughly approximated as a function of a single variable, the product of cyclotron frequency and sheath free-fall transit time, which serves as a measure of the magnetization.

A second output of the model is an estimate of the ion current drawn from the cathode side of the gap as a function of the local magnetization. As shown in the table below, as the magnetization increases, the normalized electron flux drops, but the relative ion current enhancement increases

dramatically. The final (or absolute) ion flux, scaling as the product of these parameters, is not much enhanced for any degree of magnetization. Since the largest enhancement factor is so weak the ion flux may never become sufficiently large to produce erosion.

**Table I. Ion Fluxes and Magnetic Insulation**

Magnetization	Electron Flux	Ion Factor	Final Ion Flux
0.0	0.81313	0.96976	0.78850
0.25	0.15198	4.2370	0.64394
0.50	0.15005	4.5547	0.68343
0.75	0.18714	4.4787	0.83814
0.85	0.22396	4.3375	0.97143
1.0	0.15551	7.9983	1.2438
1.15	$8.184 \cdot 10^{-8}$	$7.851 \cdot 10^6$	0.6930
1.25	$0.4937 \cdot 10^{-16}$	$1.0003 \cdot 10^{15}$	0.4940

#### Gap Equilibria, the Role of Erosion, and Force Balance

In Fig. 2 a sheath structure, in the neighborhood of an "anode" plasma surface bounding the depletion region, has been sketched. The spatial variable  $\xi$  denotes a length scaled by the gap width  $\mathcal{D}$ . The ion velocity profile  $V(\xi)$  has a scale speed  $V_o$  determined by the voltage across the gap. Once an ion flow is established in the space charge limited region, the density is determined by the space charge limited (spatially uniform) ion flux,  $\Gamma_o$  and the ion velocity profile. As indicated, the removal of ions from this surface is controlled by the relative strength of two competing terms in the continuity equation. For any ion velocity profile whatever, fluid kinematics sets a speed for the apparent movement of any density level on any spatial domain

$$\dot{\mathcal{D}} = V_o(\xi_o) \left[ 1 + \frac{\partial_\xi \ln V_o}{\partial_\xi \ln n_o} \right].$$

Clearly, if  $\mathcal{D}$  is to expand because the gap erodes, then the density level must recede, viz.

$$\frac{\partial_\xi \ln V_o}{\partial_\xi \ln n_o} < -1,$$



and the density level moves opposite to the flow! This is a totally general criterion for the erosion of an emission surface, and from it one can derive two important results.

First, it is easy to see that in regions of space charge limited flow an erosion process is impossible because for any of the equilibrium flows with fixed  $\Gamma_o$ ,

$$\frac{\partial_{\xi} \ln V_o}{\partial_{\xi} \ln n_o} \equiv -1.$$

Second, it is clearly the presheath region that requires an accurate theoretical treatment to assess the speed of any erosion process. In the presheath the ion flow makes a smooth transition from the steady interior flow  $u_o$  characterizing the source plasma to the free fall profile determined by the gap space charge. Only if the velocity gradient in the presheath solution is sufficiently strong will the erosion process be triggered; the magnitude of the ion flux that finally leaves to enter the strictly space charge limited region is only a boundary condition for the presheath problem. Establishing erosion or computing an expected speed for the erosion process must proceed from a complete solution over the presheath region – large ion flux cannot by itself establish that erosion must occur.

For a experiment like Hawk, a first approximation to the presheath problem can be developed using the ion fluxes that come from the magnetized emission model. The scale factor called "Final Ion Flux" in the table above enters as a calibration constant for the emitted ion flow. Balancing the ion flux into the equilibrium gap with a thermal flux from the interior, and assuming the presheath spatial scale is  $\kappa$  Debye lengths, the time scale for presheath density depletion can be estimated by

$$-\partial_t \ln n_i = \frac{\text{Ion Flux Out} - \text{Thermal Flux In}}{\text{Spatial Scale}},$$

$$-\partial_t \ln n_i = \frac{1.96 \cdot 10^{15} \left[ \frac{n_o \alpha_o V_o^{\frac{3}{2}}}{D^2 \sqrt{Z}} \right] - 9.79 \cdot 10^5 \sqrt{T_i/A} n_i}{743 \kappa \sqrt{T_e n_i}},$$

and, even for the most generous choice of  $\kappa=1$  and typical Hawk parameters [ $T_{e,i}=10\text{eV}$ ,  $n_i=1.0 \cdot 10^{16}$ ,  $D=0.25 \text{ cm}$ ], this estimate implies that  $V_{gap} \approx 5.0 \text{ MV}$  would be needed to overcome the thermal flux. For Hawk parameters even the largest ion flux enhancement due to thermal, magnetized emission implies weak erosion.

If erosion is not a strong opening mechanism, then what additional physics will determine the size of the depletion region? Is the size likely to be static, and what conditions might force it to expand?

Unlike a conventional space charge limited diode, the POS depletion region gap is defined by fluid surfaces that are free to move. Thus paired, charged layers having finite dimension, large density gradients, and small to moderate resistivity are considered in this model as likely sources of electron and ion emission into the thinner material between them. An opposing pair of such surfaces is then subject to strong attractive forces if the voltage across their gap is large and strong repulsive forces if the intervening magnetic field within that gap is large. As the conduction phase progresses the axial compression and radial exclusion of mass by the passage of the Hall channel can leave behind a depletion region gap at radius  $R$  in a radial force balance

Outward Magnetic Push                      Inward Electric Pull

$$\mathcal{M} \ln^2 \left( 1 + \frac{D}{R} \right) \ddot{D} = \frac{1}{2} \left[ (I_{line} Z_{line})^2 - (I_{gap} Z_{gap})^2 \right] ,$$

where  $\mathcal{M}$  is the mass of an annular slice of "cathode" or "anode" plasma, while  $I_{line}$  and  $I_{gap}$  are the currents along the plasma surfaces and across the upstream slice of the Hall channel, respectively.

Here the arrangement of forces is such that, at fixed line current and voltage, smaller separations than the equilibrium value will drive the gap shut and larger separations will drive it apart. Cast in terms of the line and gap currents and voltages, the equilibrium constraint becomes

Geometrical    Electrical

$$\frac{R \delta z \left( 1 + \frac{D}{R} \right)}{D^2} \ln \left( 1 + \frac{D}{R} \right) = \frac{506}{\sqrt{V_{gap}}} \frac{I_{gap}}{I_{line}} \mathcal{F} \left( \frac{\Omega}{\Phi} \right) .$$

Typical solutions for  $D$ , for the currents and voltages inferred at the end of the depleted gap region during POS simulations, are on the order of  $3 \rightarrow 5$  mm. During conduction this force equilibrium can be established, but such equilibria are unstable. The loss of the shunt current  $I_{gap}$  as the Hall snowplow pushes off the downstream surface of the POS leaves the system out of balance. When

this equilibrium fails, the net radial forces can be quite strong and readily open the gap on a 10 ns timescale.

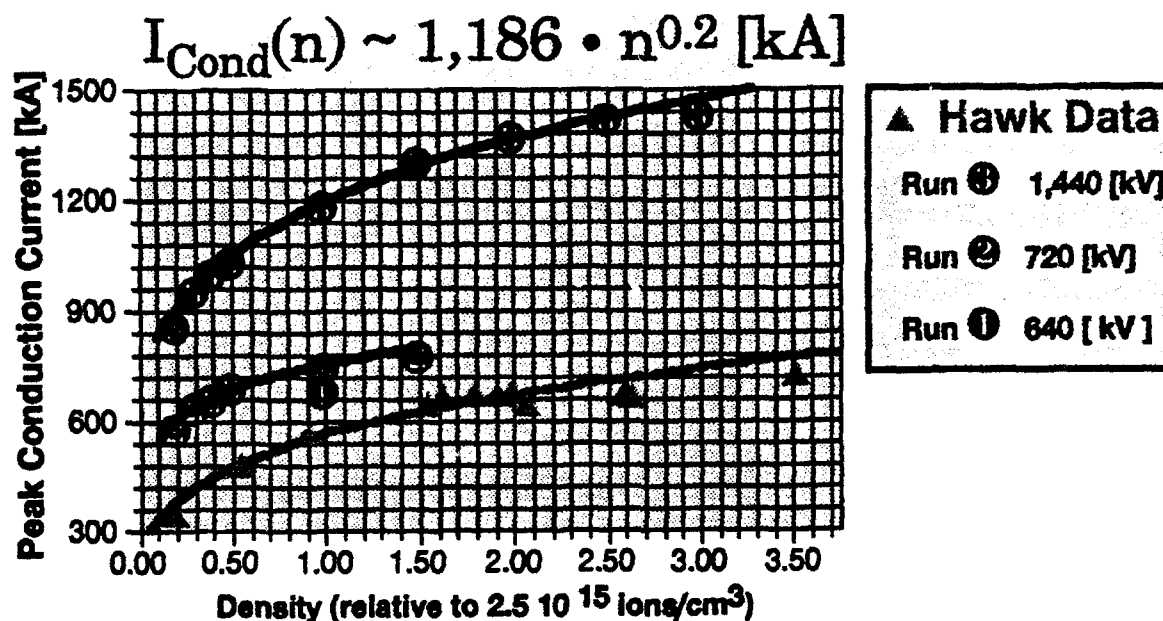
The onset of the opening phase, the gap size, and the opening rate of the POS are thus determined by the constraints imposed by the transmission line current and voltage profiles on an electrostatic and magnetostatic equilibrium between the surfaces forming the effective cathode and anode in the depletion channel. The opening is caused by the rupture of the Hall channel as it breaks free and moves downstream of the POS leaving a depletion channel with an equilibrium width already large enough to become magnetically insulated by the typical currents and voltages. As an effect enhancing the opening, when the Hall channel breaks free of the bulk POS plasma, the failure of the force equilibrium pushes the gap open further. Erosion, if it occurs at all at the higher densities of Hawk-like switches, is likely to be only a second order effect serving to strengthen the opening rather than cause it.

#### Conduction Phase Benchmarks of the POS Theory

As a fundamental benchmark for the model proposed here, a sequence of POS conduction phase solutions with a short circuit load was computed with varying background plasma densities. In this case the length of the switch was held fixed, as was the radius of the depletion channel. The peak conduction current in the model POS as a function of the average plasma density that uniformly fills the gap as the Marx bank begins its discharge was calculated. Note that the conduction time, and the peak conduction current are fixed predictions in the model once the density has been chosen from experiment; the results are shown in Fig. 3.

In the Hawk experiment the measured densities are on the order of those used here ( $\approx 2.5 \cdot 10^{15}$  ions/cm<sup>3</sup>) and a Hawk simulation was computed with the model for three cases. In the first, the charging voltage on the Marx is the same as in a typical Hawk shot,  $\approx 640$  kV. One density calibration point was checked and the predicted conduction time was  $\approx 1/\mu\text{sec}$ . In the second, the charging voltage on the Marx is the same as the rated peak voltage for Hawk,  $\approx 720$  kV. In the third, the Marx voltage has been doubled to admit more current into the inductive store and thus gain access to a larger range of densities while keeping the conduction time within the quarter cycle time of the bank.

**Fig. 3. Conduction Current Scaling**



The conduction current in the simulation line is somewhat larger than in the experiment, perhaps due to the systematic uncertainty in the density correspondence between the model and the experiment. The simulation and the Hawk data scale with density more slowly than the  $n^{0.25}$  rule, and a faster charging rate for the inductive store shifts the model scaling curve toward a larger conduction current, scaling like  $V_{\text{Marx}}^{2/3}$ . The kinematics of the depletion channel may not be perfectly represented by the existing model, but any more detailed treatment based on the same fundamentals will probably show a similar trend. To the extent the experiment moves away from this slower density scaling and source voltage dependence, the corrections to the current penetration model should be sought in terms of more detailed microturbulence resistivity models and diffusion theory.

### III. POS/PRS Coupling Behavior - Preliminary Findings

Among the many possible paths to an understanding of the coupling of stored electrical energy to radiation through an inductive energy store and a PRS, the traditional choice has focused on kinetic energy delivery to the imploding annular plasma and compression to a given fraction of the initial radius. Here the assessments will be made in a similar way but with some minor changes and additional considerations arising from the POS model being employed. In particular, while the IES (being essentially a current source) is a very natural PRS driver, the risetime of that current into the load will depend upon the intervening inductance and the associated possibility of restrike in the POS gap. For the PRS this means that the usual similarity of energy transfer for fixed values of initial mass and radius in the combination  $m_o R_o^2$  may be modified by POS restrike effects as  $R_o$  changes shift the front end inductance. For the same reason the choice to measure kinetic energy delivery at a fixed fraction of the initial radius is also modified here. The "gas bag" load model used here undergoes a transition from an annulus to a solid cylinder at a prescribed lower radius rather than a prescribed fraction of the initial radius. Subsequent to this assembly the load usually implodes further and the final stagnation radius is fair measure of the change in inductance achieved. The peak load kinetic energy is recorded shortly after the time of assembly, and is then reduced to zero at peak compression. By selecting two fixed radial measures rather than imploding to a fixed fraction of the initial radius, the absolute values of initial and final radius play properly independent roles in defining the downstream inductance seen by the POS.

#### The PRS/POS in a Hawk-like Line

With peak currents on the order of 0.75 MA Hawk is at best a weak PRS driver, but it could be equipped with a gas jet front end and used as a research facility. As a first step in examining the coupling problem that was defined in the Introduction, consider the Hawk pulser fit with a PRS load characterized by an outer (return current) radius of 3.0 cm, a pinch length of 2.0 cm, and a initial load radius of 1.5 cm. The initial Marx charge is taken to be 720kV, the POS conduction time is set to about 1150 ns by adjusting the switch plasma density. Masses smaller than  $\approx 37.5 \mu\text{g}/\text{cm}$  can be imploded in such a device, with the sum of the POS conduction and the implosion time less than the



quarter cycle time of about  $1.25 \mu s$ . Since the load is Ar the X-ray yields are a small fraction of the pinch energy, even scaling the emission by  $n_f^2$ , and this provides a useful test case precisely because the energy is fairly well bottled up. The initial mass is varied from  $15.0 \rightarrow 35.0 \mu g/cm$  and various measures of energy coupling and efficiency are developed. It is found that the overall efficiency of energy into the load rises monotonically with load mass for all cases the pulser is able to implode within the quarter-cycle time. There is a small peak in the kinetic energy coupling to the load as the mass is varied.

Table II. PRS Coupling in a Hawk Line

Mass $\mu g/cm$	$E_{Kin}$ [kJ]	$E_{Ind}$ [kJ]	$T_{pk}$ [eV]	$n_{pk}$ [ $10^{19} cm^{-3}$ ]	$Y_K$ [J]	$Y_T$ [J]
15.0	1.82	3.60	1,280	1.51	1.32	1.98
17.5	1.79	4.04	1,140	1.68	1.75	2.86
20.0	1.82	3.63	1,040	1.79	2.14	3.84
22.5	1.83	3.97	960	2.04	2.66	5.24
25.0	1.81	3.82	899	2.03	3.01	6.45
27.5	1.86	3.71	838	2.26	3.47	8.24
30.0	1.84	4.00	798	2.40	3.97	10.2
32.5	1.85	3.70	755	2.39	4.18	11.8
35.0	1.86	3.74	715	2.61	4.60	14.2

The electrical measures of energy delivery are seen to be roughly constant for all the load masses; but the load velocities, at the beginning of assembly and stagnation, were certainly not constant. What is seen here is the familiar inductance rule in action, viz. the energy to the implosion varies directly with the change in load inductance over the rundown. The variation in radiative yield then arises because each distinct mass is locked onto a distinct stagnation path by the thermodynamic constraints of the implosion. Because the radiation yield is so small, these implosion paths follow essentially adiabatic trajectories in the pressure and density. In the Hawk electrical environment the implosion dynamics are fixed by the stagnation adiabat which any given load mass is placed upon, while the energy delivered to the front end is essentially constant.

### The PRS/POS in a DECADE Line

Consider a generic DECADE pulser fit with a PRS load characterized by an outer (return current) radius of 3.125 cm, a pinch length of 2.0 cm, and a initial load radius of 3.0 cm. The initial Marx charge is taken to be 750kV, the POS conduction time is set to about 390 ns by adjusting the switch plasma density to  $6.25 \cdot 10^{13}$  ions/cm<sup>3</sup>. Each module accumulates about 2MA in the POS before the opening event is triggered by the emergence of the Hall channel from the downstream plasma boundary. The risetime of current into the load is now slower,  $\approx 50$ -55 ns, and the initial voltage on the load generally spikes to about 1700 kV during the opening phase. The peak POS voltage is essentially the same as the peak load voltage, and a second (weaker) spike in both occurs as the implosion stagnates. The second spike is generally not sufficient to spoil the magnetic insulation of the POS gap, but much more detail about the front end must be incorporated to explore the question definitively.

Masses smaller than  $\approx 4.0$  mgm/cm can be imploded in such a device, with the sum of the transfer capacitor charging time, the POS conduction and the implosion time less than the quarter cycle time. Recent 1-D and 2-D implosion calculations at DECADE current levels have indicated the persistence of a rather high level of preheating and a consequent hollowness to the implosions. A gas bag model can only simulate this through the addition of viscous dissipation if the resistivity is to remain classical, and the timing of the enhanced heating is to correspond with the earliest decelerations in the stagnation process. As a consequence the model load is equipped here with an enhanced ion relaxation time which provides a sufficiently strong viscous preheat to the implosion calculation to obtain an early average temperature similar to that in the 1-D and 2-D MHD models. The relaxation time is chosen to obtain a viscous heating rate competitive with, but not exceeding, the compressional heating rate that sets the models overall stagnation timescale. The load material is Ar and the X-ray yields are now a more sizable fraction of the pinch energy.

If the initial mass is varied from  $4.0 \rightarrow 0.40$  mgm/cm then the various measures of energy coupling and efficiency discussed above can be summarized in the table shown.

Table III. PRS Coupling in a DECADE Line

Mass mgm/cm	$E_{kin}$ [kJ]	$E_{ind}$ [kJ]	$\Delta L$ [nH]	$T_{pk}$ [eV]	$n_{pk}/10^{21}$ [cm <sup>-3</sup> ]	$Y_K$ [kJ]	$Y_T$ [kJ]
4.0	440.0	816.0	12.8	146.0	1.11	0.00	178.0
3.0	379.0	1,080	19.8	845.0	28.7	26.5	1,600
2.0	316.0	926.0	20.4	925.0	24.9	38.2	1,320
1.0	237.0	680.0	20.3	735.0	11.9	50.4	877.0
0.8	226.0	589.0	18.6	1,190	4.20	114.0	741.0
0.7	213.0	515.0	17.2	1,510	1.78	138.0	368.0
0.6	193.0	446.0	16.6	1,870	1.12	131.0	204.0
0.5	178.0	404.0	16.3	2,450	0.804	93.0	119.0
0.4	162.0	365.0	16.1	3,220	0.597	51.7	61.1

The electrical measures of the energy delivered to the front end are seen to peak with the total yield, and, while the driving current at the time of stagnation was essentially constant, the peak kinetic energy delivered drops off less rapidly than the mass, indicating progressively higher implosion speeds as the mass falls. The K-shell yield peaks at a mass slightly lower than that which optimizes the total yield. The peak in K-shell yield with lower mass occurs because the very light loads get hotter and turn around faster at lower density. The lower yields at large mass are simply a matter of insufficient energy transfer.

#### IV. POS/PRS Coupling Behavior – Conclusions

The results detailed above confirm, once again, that a DECADE class machine can couple energy to a PRS load and do so in a relatively efficient manner. From these calculations one would expect between 0.5 → 1.5 MJ to be coupled forward of the POS modules into the front end. More important than the power flow details in this preliminary study however is the result that a POS model anchored in a few simple hypotheses can be successful at DECADE power levels and properly responsive to the electrical environment generated by the PRS and any front end MITL loss processes. Several important results should be noted from the POS model:

- i. Self-similar Hall current channels can exist for any bulk plasma density profile.

- ii. These Hall current channel can carry very large currents, implying the POS is not a current limited device.
- iii. The model captures the conduction time, peak conduction current, opening time, and the late time impedance.
- iv. The model exhibits  $I_{cond}$  scaling with density and Marx voltage that is compatible with experimental data.
- v. The concepts that work to explain the conduction phase have important implications for the opening phase and the viability of any erosion hypothesis. In particular, any erosion speed calculation must account for the presheath structures; and, the emission theory appropriate to the dense Hawk POS conduction phase predicts weak ion flux enhancement.
- vi. A causal opening mechanism has been identified that is distinct from erosion. In particular, gap equilibria can exist which predict the inferred electrical gap size, and the loss of force balance in these equilibria at the end of the conduction phase predicts gap accelerations and opening times compatible with experiment.

The POS model can be viewed as the union of three distinct, but intimately related parts. Each element: magnetized emission theory, Hall channel penetration, and gap dynamics, can and should be refined much further, but the need to do so will be based upon the performance relative to existing and further POS experiments. However these elements evolve, the results can now be installed in an integrated numerical framework that works rather well as a model of the entire DECADE machine.

The coupling problem posed at the beginning of this work has also been addressed in the context of a particular generic machine design, with the result that POS restrike appears unlikely to be a major concern. While some POS restrike does occur it generally is too little and too late to have much effect on the energy delivered to the load. Naturally this is a very preliminary assessment and it must be refined further with detailed machine design parameters and careful attention to the experimental results as they are available. In addition to the painstaking collection of machine details and further POS comparisons, future efforts will also include a second modeling alternative for the DECADE line, viz. the combination of modules to a single parallel line with an appropriate POS segment.

## VI. L-Shell Model Development and Scaling

The development of x-ray diagnostics in the L-shell requires an extensive atomic data base. These data include energy levels, collision strengths, photoionization cross sections, and dielectronic recombination branching ratios. When accurate data is obtained, it can allow us to develop scaling relations to obtain more reliable and more extensive data files. This data processing is also necessary for scaling PRS load dynamics. We are continuing the process of slowly upgrading and evaluating our L-shell atomic data base, since these data in our current data base were obtained only in an approximate way and are not very accurate or complete. We have developed much improved calculations of dielectronic recombination (DR) rate coefficients over the last few years. A dataset was completed last year of DR rates for recombination from oxygen-like ions for Ar, Ti, Fe, and Se. These DR calculations involve detailed calculations of energy levels and autoionization as well as radiative rates. We are in the process of demonstrating their Z-scalability. We are trying to develop scaling relations for the singly as well as doubly excited energy levels, autoionization rates, radiative rates and state specific DR branching ratios following our scaling of dielectronic recombination data in fluorine-like ions (Phys. Rev. 42, 2640(1990)).

By carrying out the process of scaling using three and four-parameter fits to the oxygen-like DR data, one not only efficiently extends the data base to all elements in the fourth row of the periodic table, one also obtains a check on the accuracy of the data of the Ar, Ti, Fe, and Se databases that were calculated in detail. While most of the data can be fitted with extreme accuracy, there are a few anomalies. These are shown in Figs. 1, 2, and 3

using a few of the states that make important contributions to the DR process. Fig. 1 shows how the energies scale for the doubly excited states:  $2p^33s^2$ ,  $2p^43d^2$ , and  $2p^43snl(4 \leq n \leq 8)$ . The accuracy of the latter 4 data points is seen to be less than that of the first 8 data points. The least squares fit presumably improves upon the accuracy of the latter 4 points. In Fig. 2 we see that the total autoionization rates for the states  $2p^33s^2$  and  $2p^43d^2$  scale very accurately. The data for the autoionization rates of the  $2s2p^5nl(5 \leq n \leq 10)$  state do not scale as accurately. Similarly, Fig. 3 shows that the total radiative rates for the states  $2p^33s^2$  and  $2p^43d^2$  scale very accurately, but that the radiative rates for the  $2s2p^6nl(5 \leq n \leq 10)$  state show small errors. Our next effort was thus to track down sources of the few erroneous data, especially if human errors in bookkeeping such a large number of input and output data had been made. We are going through a thorough checking of our database for oxygen-like DR recombination data. A few mistakes have been found and corrected and our error investigation is nearing completion.

We have also recently completed DR rate calculations for oxygen-like molybdenum (Mo) in order to determine the accuracy of extrapolating the scaling relations. Once we have finished the Z-scaling relations using the O- to F-like Ar, Ti, Fe and Se data, we will be able to test them by comparing the Z-scaled data with the explicitly calculated Mo data. We have also just begun to calculate N- to O-like DR data to continue to fill out the L-shell dataset.

During the development of a detailed atomic model for neon-like selenium that utilizes the above DR data, we discovered that our in-house capabilities for calculating the necessary collision strengths and photoionization cross sections for the model were greatly inadequate. The Branch collision strength capabilities had been developed for K-shell modeling and were unreliable for the L-shell. The neon-like selenium model was completed only by tediously

utilizing data that was available in published x-ray laser literature. However, the reliability of our DR rate calculations must be matched by a similar high accuracy and consistency for our collision strength and photoionization data. We thus investigated the possibilities of obtaining or accessing collision codes such as the one put together by Zhang and Sampson at Penn State University or even a modified version of Cowan's code which can be used to accurately calculate the needed large number of L-shell collision strengths.

We have now acquired atomic codes, developed by the researchers at Los Alamos Laboratory, to calculate accurate collision strengths and photoionization cross sections (and in turn radiative recombination rates). Using these codes, we should be able to generate the large datasets that are routinely needed for L-shell ionization balance calculations. These codes include the structure codes of R. D. Cowan and are available on the Los Alamos Cray. We have obtained printed documents for properly using the codes. They include 1) CATS, a modified version of Cowan's Atomic Structure Code, 2) ACE, Another Collisional Excitation code, 3) LINE, a code for computing atomic LINE spectra, and 4) TAPS, a Theoretical Atomic Physics code which is used to handle and display the data generated by the three previous codes. The purpose of the atomic physics code development effort at Los Alamos was to bridge the gap between simple models and sparse sets of more accurate data by providing a collection of computer programs for conveniently calculating the quality atomic data needed for ionization balance calculations and diagnostics. These codes are easy to run, and their required input has been minimized. The fact that they generate atomic physics data in the greatest detail possible as well as perform averages when such detail is not necessary makes them very useful. For example, the programs store data based on fine structure levels, but if quantities based on multiplet terms or configurations

are desired, then the fine structure data is averaged. We are beginning to use these codes by learning how to set up the atomic structure files, input/output commands, code action commands, data file management commands and the commands needed to calculate multiplet strengths and excitation cross sections. We are also exploring several physics issues such as what kinds of wave functions or what approximations need to be used in these codes for our particular applications. We can now use the Los Alamos codes to calculate collision strengths.

In order to test the Los Alamos collisional codes we calculated a few neon-like selenium and iron collision strengths. The results obtained agreed with other published and presumably more accurate collision strengths except at very low energies. We therefore investigated the use of ACE (as mentioned before), which uses a distorted wave approximation and gives more accurate collision strengths than CATS. However this code takes a large amount of computer time. The researches at Los Alamos Laboratory are still in the process of optimizing it by adding options for calculating more atomic parameters. We are presently communicating with them and as more information becomes available we will incorporate it accordingly in our calculations. Since we need to generate large numbers of collision strengths, the ACE code may not be very economical and practical. Thus, at present, we are using the PWB approximation for most of the collision strength calculations and using ACE for the most important diagnostic transitions, especially at low energies.

We have used the plane wave Born (PWB) method of Cowan to calculate the collision strengths for N-, O- and F-like selenium. Fig.4 shows the energy level diagram for the F-like system that we are currently using for our database development. The other L-shell ionization stages have a similar structure: only the degeneracy of the states changes from one ionization stage to another. The collisional excitations A, B, and C (labeled in Fig.4) from



the ground state to the 3s, 3p and 3d excited states respectively are especially important. In Figs. 5 and 6 we show the calculated collision strengths (solid lines) obtained from CATS for these transitions for F-like and O-like selenium and compare them with those that had been previously calculated (dotted lines) from our adapted in-house codes. Fig. 5 shows that the collision strengths for the dipole transitions (excitation from the ground state to 3s and 3d states) in the CATS calculations are close to those calculated previously except at very low energies. Agreement is within a factor of two for the monopole (ground state to the 3p excited state) transition. However, there is no agreement between the present and previous calculations of collision strengths for the same transitions in O-like selenium as can be seen from Fig. 6. Since the CATS collision strengths are obtained in a more consistent fashion and the collision strengths for the same transition (for F-like and O-like systems) show similar behavior we believe that our present results are much more accurate and should be scalable. The previous collision strength data for O-like selenium, on the other hand, were especially inaccurate and unscalable.

It is known that collision strengths decrease as the nuclear charge  $Z$  increases. We are in the process of obtaining collision strengths from CATS for the same ionization stages and for the same transitions for iron as we have done for selenium. Once these data are obtained, we will be able to verify the  $Z$  dependence of collision strengths as described in our 1990 final report and eventually scale the data to obtain collision strengths initially for any  $Z$  between iron and selenium and possibly beyond.

Presently our L-shell data base does not include any radiative recombination (RR) rates to excited states. In order to have an upgraded and complete model we have to eventually include such rates. There is also available an ionization code called GIPPER on the Los Alamos Cray. However,

this code is still being developed for the calculation of more improved collisional ionization rates, and there is no available written document on it. We can, however, use it to calculate photoionization cross sections; thus, we intend to learn to use GIPPER in the future to calculate photoionization cross sections and then, using detailed balance, calculate the radiative recombination rate coefficients needed to compute the continuum emissions of importance in the L-shell.

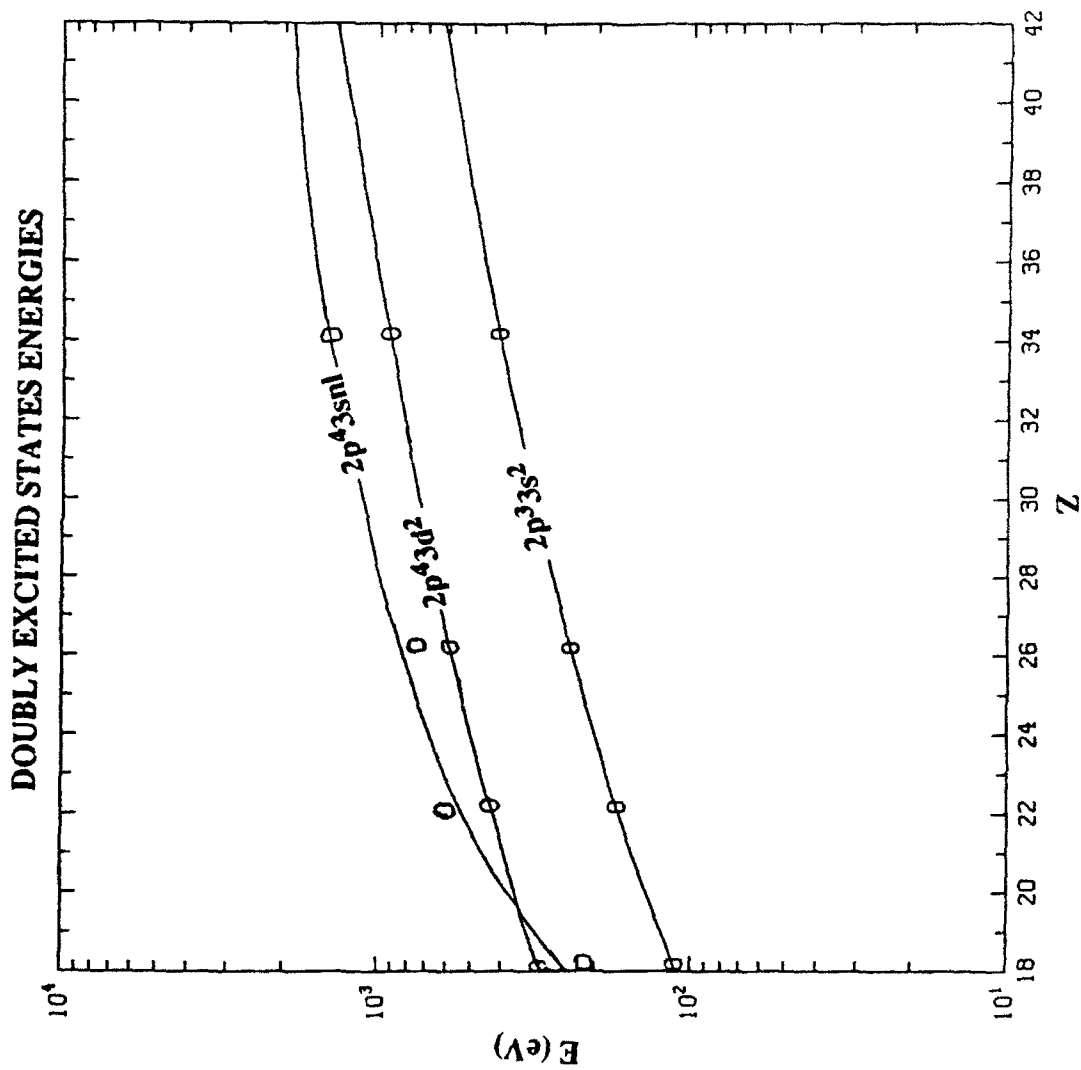


Fig. 1 Variation of energies of a few doubly excited F-like states. The curves are three-parameter fits to the four calculated points shown of Ar, Ti, Fe, and Se ions.

# TOTAL AUTOIONIZATION RATES

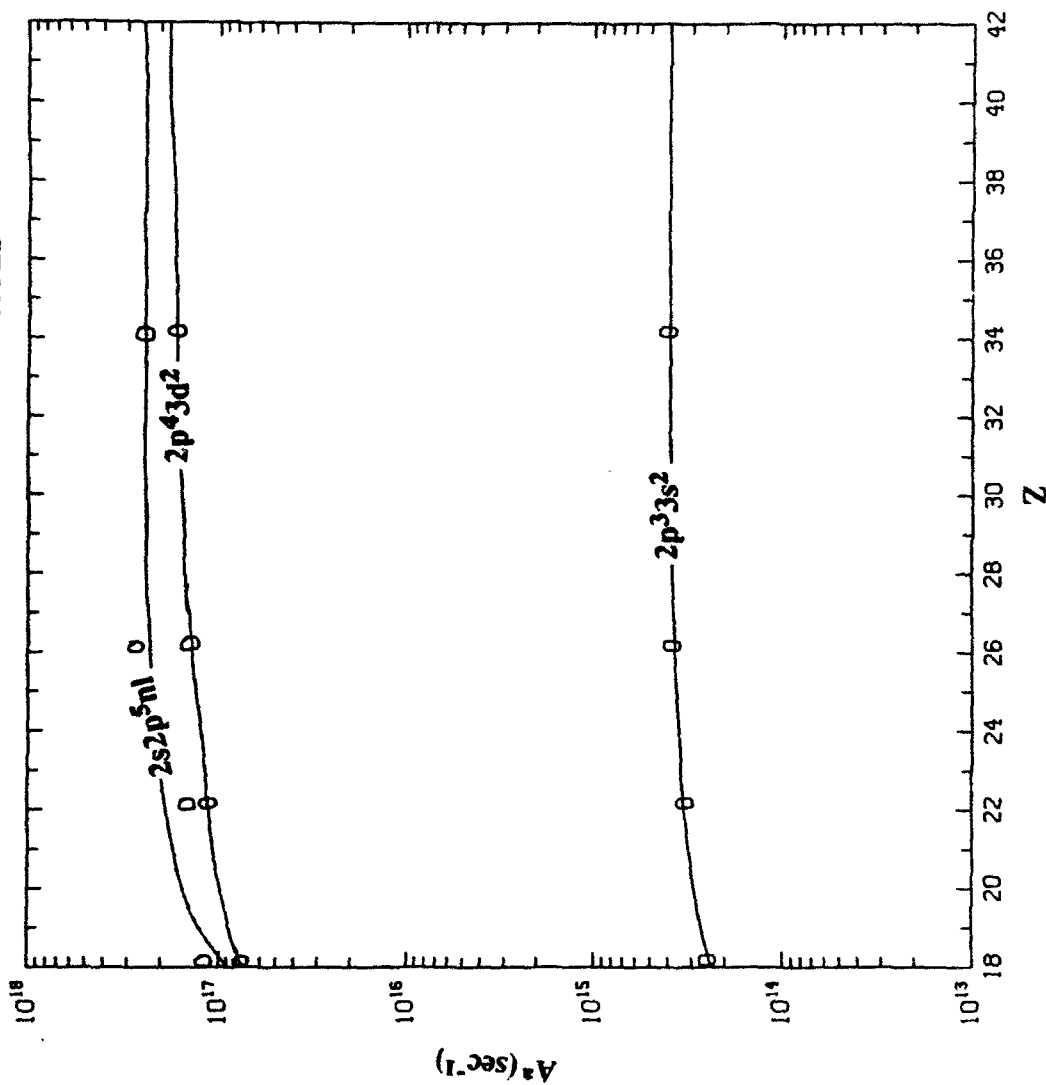


Fig. 2 Variation of total autoionization rates (of the states labeled) as a function of  $Z$ . The curves are three-parameter fits to the four calculated points shown for Ar, Ti, Fe, and Se ions.

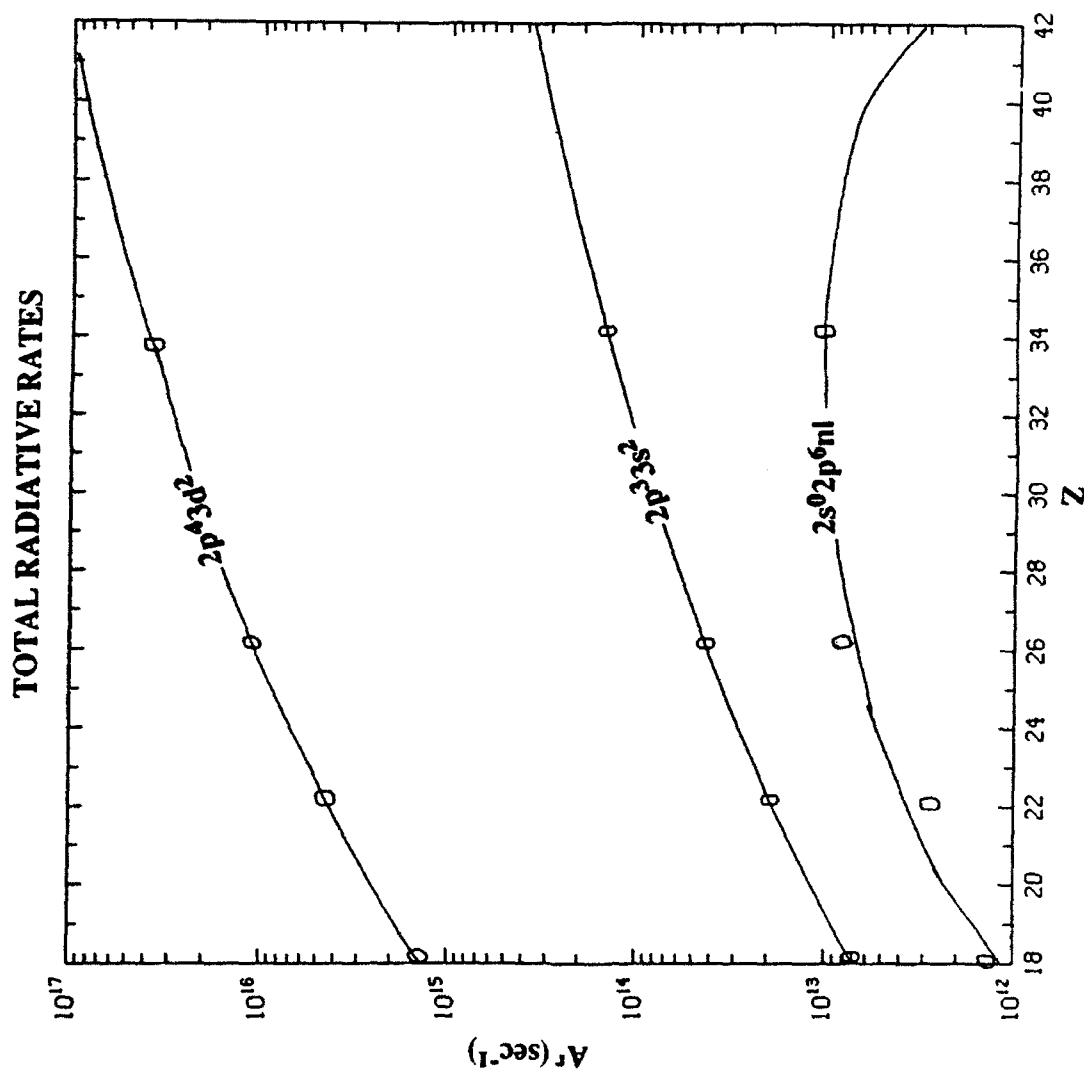


Fig. 3 Variation of total radiative rates (of the states labeled) as a function of  $Z$ . The curves are three-parameter fits to the four calculated points shown for Ar, Ti, Fe, and Se ions.

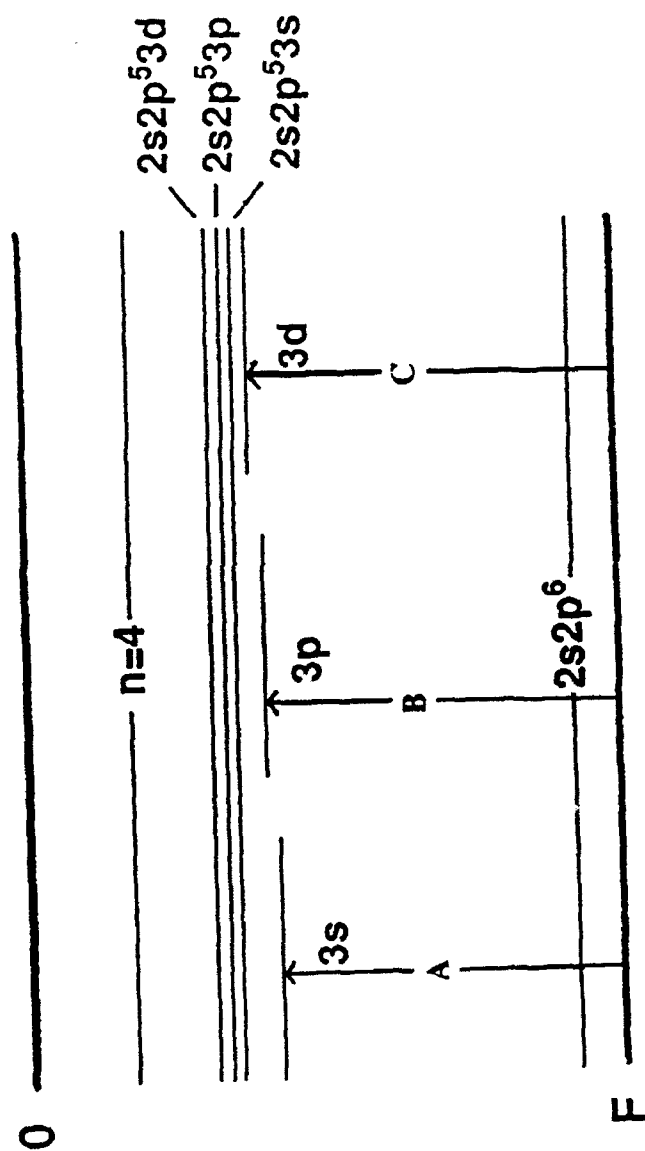


Fig. 4. Energy level diagram for F-like ions.

# COLLISION STRENGTHS FOR EXCITATION FROM GROUND STATE

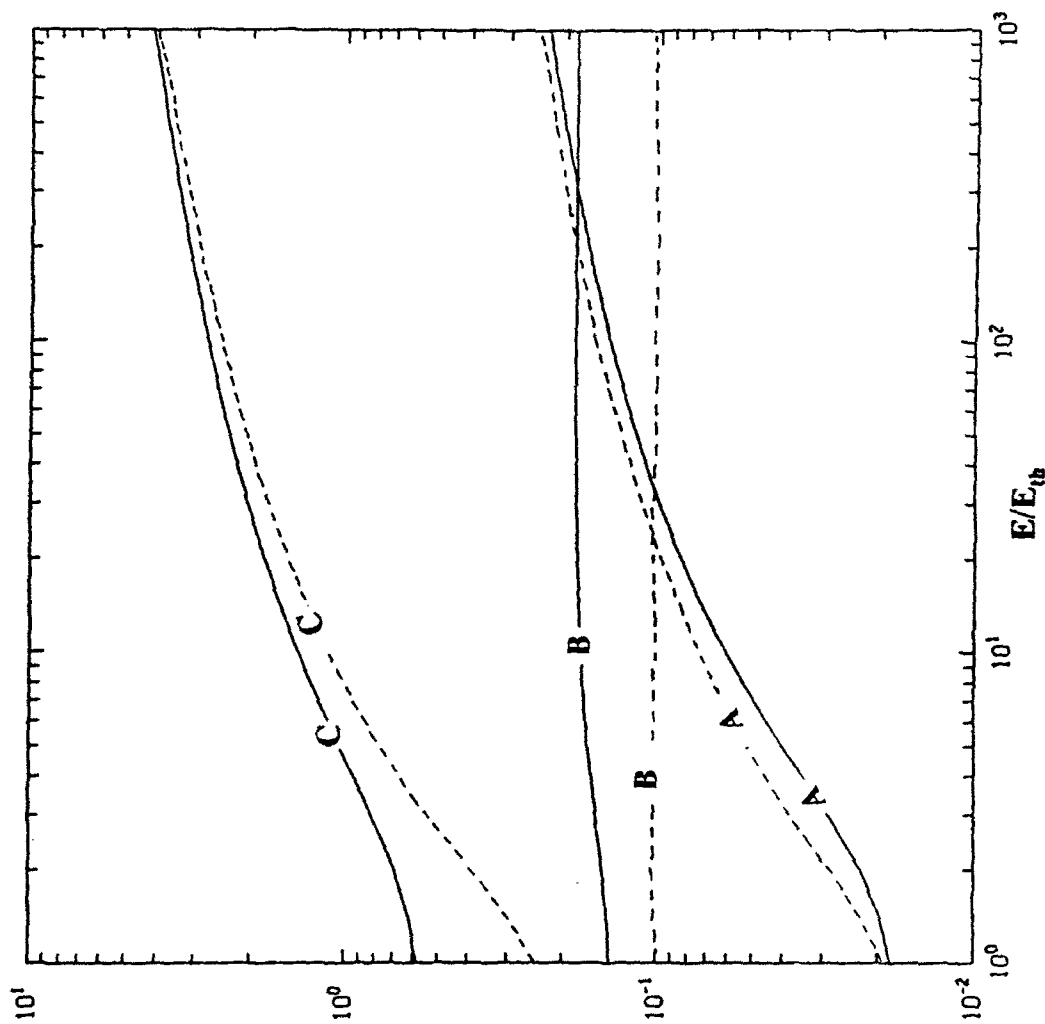


Fig. 5. Collision strengths of the 3s, 3p and 3d excited states of F-like selenium for excitations from the ground state of the ion. The solid lines represent the present calculations and the dotted lines represent previous calculations.

# COLLISION STRENGTHS FOR EXCITATION FROM GROUND STATE

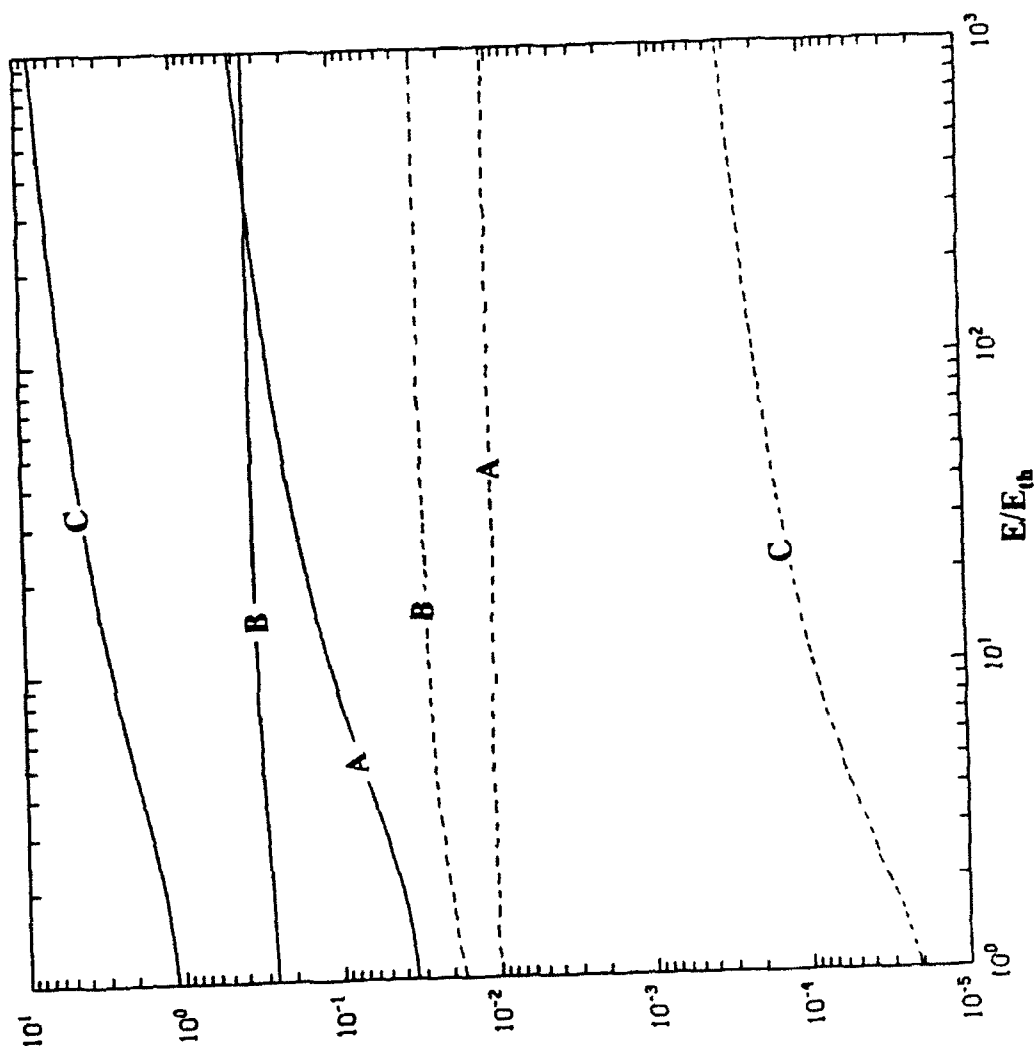


Fig. 6. Collision strengths of the 3s, 3p and 3d excited states of O-like selenium for excitations from the ground state of the ion. The solid lines represent the present calculations and the dotted lines represent previous calculations.